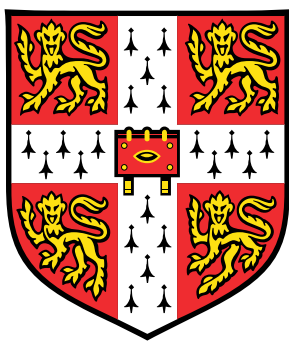# A New Framework for Simulating Multimaterial Systems and Gaseous Cookoff

Haran Jackson

The Centre for Scientific Computing

University of Cambridge

This dissertation is submitted for the degree of

Master of Philosophy in Scientific Computing

Fitzwilliam College   Supervisor: Dr N. Nikiforakis

Declaration

This dissertation is the result of my own work and includes nothing which is the outcome of work done in collaboration except where specifically indicated in the text.

Word Count (including tables, figure legends, and appendices): 14,896

<div align="right">

Haran Jackson

August 29th 2016

</div>

Acknowledgements

Abstract

The recently proposed Hyperbolic Peshkov-Romenski (HPR) model of continuum mechanics [85] is able to describe both solids and fluids (viscous and inviscid, Newtonian and non-Newtonian) in the same framework. Dumbser et al. extended the model to include a hyperbolic subsystem for thermal conduction [31]. This extended model should be well suited to simulating cookoff, where multiple materials and phases of matter may be present, and up until now models have relied on coupling different sets of equations to describe the different materials. The hyperbolicity of the HPR system also makes it amenable to large-scale parallelisation, and it does not suffer from the appearance of nonphysical infinite-speed waves, unlike the parabolic Navier-Stokes equations, or the classical Fourier law of heat conduction.

In this study, an Arrhenius reaction model is combined with the HPR model and the feasibility of simulating cookoff within this framework is demonstrated. Two substantial theoretical developments are also presented. Firstly, a new method is proposed for significantly accelerating the simulation of slow cookoff on short, bounded domains. The acoustic components of the system are approximated by assuming that the pressure equilibrates on a faster time scale than the other processes of the system, and only a reduced subsystem is solved. Secondly, a modification of Barton's [12] application of Sambasivan and Udaykumar's Riemann Ghost Fluid Method [98, 99] is devised for the HPR model, allowing it to be used in multimaterial problems with heat conduction. Both developments are assessed numerically and shown to be effective.

Contents

List of Figures

List of Tables

Nomenclature

Roman Symbols

$\mathbf{0}_n$ Zero vector of length n

$\boldsymbol{e_i}$ ith basis vector

$\boldsymbol{J}$ Thermal impulse vector

$\boldsymbol{q}$ Heat flux vector

$\boldsymbol{v}$ Velocity

A Distortion tensor

B_c Prefactor in Arrhenius reaction kinetics

c_0 Adiabatic speed of sound

c_h Characteristic velocity of heat waves

c_p Specific heat capacity at constant pressure

c_s Characteristic velocity of transverse perturbations

c_v Specific heat capacity at constant volume

c_∞ High frequency limit of phase velocity of longitudinal sound waves

C_{cfl} Courant number

E Total specific energy

E_a Activation energy of a reactive species

I_n Identity matrix of size $n \times n$

K_0 Reaction rate in discrete ignition temperature reaction kinetics

p Pressure

p_0 Reference pressure

p_∞ Pressure constant in stiffened gas equation of state

P_r Prandtl number, equal to $\frac{c_p \cdot \mu}{\kappa}$

Q_c Energy formed per unit mass of reactant

R_c Universal gas constant

R_e Reynolds number

s Entropy

T Temperature

t Time variable

T_i Ignition temperature in discrete ignition temperature reaction kinetics

T_0 Reference temperature

x Space variable

Greek Symbols

α Constant related to characteristic velocity of heat waves

δ Kronecker delta

ϵ Dimensionless inverse activation energy

γ Ratio of specific heat capacities, equal to $\frac{c_p}{c_v}$

κ Thermal conductivity

λ Concentration of reactive species

μ Viscosity

ρ Density

ρ_0 Reference density

σ Viscous shear stress tensor

τ_1 Strain dissipation time

τ_2 Thermal impulse dissipation time

Other Symbols

$\|\cdot\|$ Euclidean vector norm

$\|\cdot\|_F$ Frobenius matrix norm

Acronyms / Abbreviations

ALE   Arbitrary Lagrangian-Eulerian

AMR   Adaptive Mesh Refinement

CFL   Courant–Friedrichs–Lewy

CJ   Chapman–Jouguet

DG   Discontinuous Galerkin

EOS   Equation of State

FV   Finite Volume

GFM   Ghost Fluid Method

HPR   Hyperbolic Peshkov-Romenski

NS   Navier-Stokes

ODE   Ordinary Differential Equation

PDE   Partial Differential Equation

RGFM   Riemann Ghost Fluid Method

RP   Riemann Problem

WENO   Weighted Essentially Non-Oscillatory

WLOG   Without Loss of Generality

ZND   Zel'dovich-Neumann-Döring

Notes

Unless otherwise stated, repeated indices in vector, matrix and tensor quantities are to be summed over. If M is a matrix, then $\boldsymbol{M_i}$ is taken to be the ith column of M (note, not the ith row). MATLAB-style index notation is used, such that $M_{i:j}$ refers to the matrix consisting of the columns $i \ldots j$ of M (including columns i and j). $M_{i:j,m:n}$ refers to the submatrix of M with corners at M_{im} and M_{jn}.

Chapter 1

Introduction

1.1 Background

Parabolic vs Hyperbolic Systems

Information in parabolic systems of partial differential equations travels at infinite speed, and a perturbation in the condition of the system at one point has an effect at all other points instantaneously. Thus, parabolic systems (such as the Navier-Stokes equations or the classical Fourier equations of heat transfer) are not amenable to parallelisation. By contrast, solutions to hyperbolic systems are wave-like in structure, with finite speeds of propagation of information. Solutions on different parts of the domain can be calculated independently, leveraging the great advances that have been made recently in parallel computing technologies, particularly in the burgeoning field of general purpose GPU computing. The use of hyperbolic models also allows for the utilisation of Riemann solvers, on which there has been a great deal of work over the years (see Toro [112] for a broad overview).

Even disregarding the practical benefit of employing hyperbolic schemes, there is the more profound issue that we live in a causal universe, and ultimately parabolic systems cannot be a "true" description of reality. Although this discrepancy often does not matter in practice, there are problems to which parabolic models are particularly unsuited (see [23, 40, 45, 46] among many others). Whilst an in-depth discussion of these issues is beyond the scope of this study, it should be noted that there are also philosophical problems with considering hyperbolic systems to be "true" descriptions of reality, as they can permit discontinuous solutions, and it can be argued that true discontinuities do not appear in nature. In any case, the continuum assumption of continuum mechanics is just a useful approximation to the actual underlying physical processes, and no model we devise will reflect completely the real nature of the phenomena that it purports to describe. It suffices to say that the causality issue regarding parabolic systems is more often troublesome than the issues relating specifically to hyperbolic systems.

In addition to the problems already discussed, in the case of the Navier-Stokes formulation in particular, the stress tensor is derived from empirical observation of the macroscopic behaviour of steady, homogeneous flows, rather than from a first-principles microscopic description. As shown by Yakhot [116], this can result in problems when modeling essentially unsteady and non-equilibrium flow. On top of this, the NS equations are second order, making them more sensitive to the quality of the computational mesh than a first order system.

Several attempts to produce a hyperbolic formulation of viscous fluid dynamics have been made (see for example [11, 41, 45, 57, 79, 83, 92]). However, as noted by Peshkov and Romenski [85], the systems described all essentially take the following form for some model-specific dissipative quantity X:

$$\dot{X} = -\frac{1}{\beta}\left(X - X_{NS}\right) \tag{1.1}$$

where β is a relaxation parameter and X_{NS} is the value obtained from the Navier-Stokes equations. This is a hyperbolic relaxation model, constructed as a first-order extension to the second order NS equations.

These models are all based on the series expansion of the distribution function with respect to a set of moments. The physical meanings of the moments are largely ignored, and they have neither microscopic counterparts, nor are they defined as volume-averaged quantities. Additionally, a naive model of the form above is not frame invariant. Often this is remedied by introducing an objective stress rate $\dot{X}$, but as this can be defined in many ways, this results in different solutions to the model, along with violation of the second law of thermodynamics and loss of well-posedness of the initial value problem [85].

The recently proposed model of Peshkov and Romenski (described in Section 1.3) benefits from the advantages of hyperbolicity, while avoiding the deficits inherent in the existing hyperbolic models. It is derived fundamentally from a microscopic description of the continuum phenomena it describes. It is also able to model different materials and phases of matter in the same framework. This feature makes it well-suited to simulating the process of cookoff, to be described next.

Cookoff

The term "cookoff" is used to denote the process by which explosives deflagrate or detonate unintentionally, due to ambient heat from the surrounding environment. It is imperative that this process is properly understood, to avoid repeats of the many fatal and destructive civil and military accidents that have occurred over the years.

Cookoff is extremely complicated, with many different stages. Many different materials and phases may be present at the same time. Large costs, difficulty in experimental design, and safety issues mean that computational modeling has become of paramount importance in predicting the cookoff behaviour of different materials in different scenarios. Computational modeling presents a whole new set of challenges, however.

Despite extensive algorithmic optimisation, computational techniques such as adaptive mesh refinement, and a roughly 1000-fold increase in maximum attained computing power between 2006 and 2016 (~100 TFlop/s - ~100PFlop/s [3]), cookoff simulations remain relatively computationally challenging. As detailed by Asay [8], we are still a long way from being able to perform accurate large-scale simulations of the full systems of equations governing such phenomena on less than a time scale on the order of days. It is noted that computational error is linearly dependent on domain size, and CPU time depends nonlinearly. Thus an increase of 3 orders of magnitude in computational power yields only a tenfold decrease in error in 2D simulations, and a decrease of only 5.6 times in 3D. There is a clear need for new fundamentally-different ways of reducing the computational effort required.

If the time step of the computational method used to model cookoff is restricted by a CFL condition based on the speed of sound, the heating phase will take an excessively long time to calculate, even though the dominating process is thermal conduction; a slow, smooth process. A strict CFL condition will be required to accurately resolve the deflagration/detonation phase, but this phase represents a small fraction of the total time. There have been several attempts to circumvent this issue, described here.

Selesovský [103] models the thermal loading of explosives using the Frank-Kamenetskii model of thermal conduction with Arrhenius reaction kinetics [38] (disregarding the non-conductive features of the process, such as flow and acoustics). The time step in the heating phase is chosen according to a standard stability condition according to the parabolic nature of the system. Once thermal runaway occurs, the time step is

reduced by an amount obtained through trial-and-error (building upon results from Sućeska and Matečić-Muśanić [108]) ensuring that the latter stages of the process are resolved correctly. This reduction is not actually required for numerical stability; it is required for accuracy. Clearly, it is not desirable to obtain the time step experimentally for every reactive process one wishes to model.

A huge amount of the work on cookoff modeling has been performed at the Lawrence Livermore (and to a lesser extent, Sandia) National Laboratories. Much of the work at LLNL has gone into their ALE3D multiphysics code [1]. One of the methods employed in the ALE3D code to circumvent the time step restriction in the heating phase is variable mass scaling. Implemented by Yoh et al. [117–119], this technique is based on the work of Prior [87]. The system is integrated explicitly and the density of the materials in the system is scaled higher so as to reduce the effective speed of sound, and thus artificially increase the time step permitted by the standard CFL condition. In practice, the desired time step is fixed and the density is scaled to its required value. At the transition between the heating and combustion phases, the scaling is reduced incrementally to its natural value. Despite its success in increasing the computational efficiency of the calculations - especially when inertia effects are negligible - this technique appears to have fallen out of favour in recent years in simulations involving large amounts of fluid flow, owing to the associated spurious oscillations in the motions of the heated materials detailed by Howard et al. [55]. It is still used in more static thermal heating problems (see for example Khairallah and Anderson [64], who obtain a 3- to 10-fold speed up using this method).

Lately, a different method has been used by Nichols and Schofield [82] and McClelland et al. [73]. In the heating phase, the fluid is modeled with the incompressible Navier-Stokes equations, which are solved using the semi-implicit pressure projection method presented by Gresho [47, 48]. This removes the stringent CFL condition based on the speed of sound. Although each iteration is more computationally taxing, much larger time steps can be taken than with an explicit solution method. At each step, the advection of the reactive species is calculated with an explicit forward Euler scheme and its diffusion is calculated with an implicit backward Euler scheme. Only one iteration of both of these schemes is performed at each step, meaning that the time step for all processes is in fact limited by a CFL condition based on the velocity of the fluid. These velocities tend to be small in slow cookoff situations, leading to a large time step at this stage. $C_{cfl} = 0.1$ was used in the cited studies. The system

governing the chemical reaction is also iterated at each time step.

In the early stages of the simulation the aforementioned method is efficient, but as the material heats up the time step will reduce to the point that it is faster to perform a full explicit calculation at each step. This was determined experimentally in [82] to occur roughly when the implicit time step is less than 100 times larger than the explicit time step. A complex transition to the explicit solver is then undertaken. Neighbouring nodal values for the chemical composition are linearly interpolated to give element-centred values. The density and internal energy are found iteratively from the average fluid pressure, the averaged temperature, and the compositional state. This is done as inconsistencies in these variables can be introduced in the preceding stages. The velocity field can become chaotic under the implicit solver so this is set to zero everywhere. Owing to the complexity of the transition, the CFL time step is reduced by a factor of 1000 to allow local equilibration of the system and to avoid any macro-scale aberrations.

This transition process introduces large changes to the system at the most critical point in determining its subsequent violent evolution. The time of transition and the time step reduction factor have to be set by trial-and-error, meaning that they may need to be tested for each new simulation set-up. A process of this sort will always be necessary, however, if the heating phase is solved implicitly. In addition to the schemes outlined here, in [73] the diffusivity of the species was artificially increased (by trial-and-error) to avoid numerical instabilities. The fluid viscosity was also increased ten-fold to slow the flow and increase the time step given by the velocity CFL condition on the advection of the species. Clearly, adjustments such as these are not desirable.

Multiphase Systems

The definition of a multiphase system is slightly ambiguous in the literature. Here it will be taken to mean a system consisting of either two or more different materials (possibly in the same phase of matter), or two or more volumes of (possibly the same) material in different phases of matter. There are two aspects of multiphase systems that require attention: multiphase flow, and multiphase heat transfer. The latter becomes important when the phases are at different temperatures. In this study, the different phases will be assumed to be immiscible.

Without a unified model of continuum mechanics, capable of describing all phases in the same framework, different sets of equations may have to be used in the different regions occupied by different phases. These systems arise, for example, in fluid-structure interaction, or oil-water interfaces. An overview of current approaches to multiphase systems will now be given. The examples here are illustrative but not exhaustive.

There has been a huge amount of research activity in the field over the years, but current approaches can be broadly classified as either monolithic or partitioned [54]. In a monolithic scheme, all phases are described by the same set of nonlinear equations. The evolution of the interfaces is implicit to the equations, unlike in partitioned schemes. See for example [56, 76]. The system is solved by a multivariate Newton-type method. It is often ill-conditioned, due to the different scales of the state variables of the different phases. Thus, iterative solvers are required, proving inefficient unless good preconditioners are available. Codes tend to be very specialised to the specific problems they solve, and it requires expertise to develop and maintain such methods.

In a partitioned scheme, the states of the different phases are calculated separately at each time step, possibly using different models. See Rossi and Oñate [96] for a recent overview of some of the common algorithmic features of these schemes. The individual systems do not suffer from the scaling-induced conditioning problems of monolithic schemes, but attention now needs to be payed to the material interfaces. Modeling them can be unstable and relatively computationally expensive (although typically not as expensive as solving the full monolithic systems). One of the great benefits of partitioned schemes is that legacy implementations of common models may be used in the domains occupied by materials that they describe. These implementations are often well-used and relatively bug free, and tend to be written efficiently for the kinds of problems that the solve. As an example of a software suite taking advantage of this, see the Caltech's Virtual Test Facility [4].

Under both types of schemes, the models describing the different phases may be formulated in either a Lagrangian, an Eulerian, or an ALE framework. Solids models tend to come in Lagrangian form, and often these are combined with ALE forms for the fluid phases, so that the fluid meshes may deform to match the deformation of the solid (see, for example, Pin et al. [86]). These schemes tend to be very accurate, but like all Lagrangian schemes, they fail if the meshes become highly contorted. Thus, adaptive remeshing is often necessary. Some authors have coupled a Lagrangian solid scheme with an Eulerian fluid scheme, but extra care must be taken when applying

the boundary conditions to the interface, which corresponds to the intersection of the Eulerian and Lagrangian meshes (see Legay et al. [66] for an implementation using level sets, or Fedkiw [37] for a GFM coupling). Some authors, such as Ryzhakov et al. [97], have found success in using the common Lagrangian formulations for the solid, and a reformulated Lagrangian model for the fluid, implementing the necessary adaptive remeshing. Yet another option is to model both the fluid and the solid in an Eulerian framework, although this now necessitates a level set method or volume of fluid method [53] to track the interfaces. Also, these methods are more prone to losing small-scale geometric features of the media, unless methods such as AMR are employed to combat this [54].

In a recently submitted paper, Michael and Nikiforakis [75] (building on the work of Schoch et al. [101]) couple various Eulerian models of reactive and inert fluids and solids by use of a Riemann Ghost Fluid Method, with the ghost states calculated using specialised mixed-material Riemann solvers for each interaction (see Section 1.4). Whilst these techniques do not suffer from the mesh contortion issues inherent in Lagrangian formulations of continuum mechanics, and the interface coupling tends to be less computationally expensive than the iterative techniques demanded by monolithic schemes, a fair amount of theoretical work needs to be done to derive analytical relations describing the interactions between every pair of models used.

If it were possible to describe all phases with the same Eulerian model, this method could be used, with only one type of Riemann solver needed to cope with any multiphase problem posed. This would effectively be a partitioned scheme with the same system solved in each domain. The HPR model represents such an opportunity. As will be seen, the model also includes terms for heat conduction, which do not appear in the basic formulations of many of the common models used in multiphase systems (e.g. the Euler equations, or the Navier-Stokes equations). Heat conduction is often ignored in multiphase modeling, but such a framework based on the HPR model would almost unavoidably include it. It should be noted, though, that any unified model of continuum mechanics purporting to describe all phases of interest must be at least as descriptive as competing models tailored to each individual phase if the utmost model fidelity is required. Although the results for the HPR model applied to standard test cases have been promising, both here and in other preliminary studies [16, 31], more work is required to determine how faithfully the HPR model reproduces common agreed phenomenological results.

1.2 Purpose and Structure of this Study

The purpose of this study is to develop a hyperbolic framework for modeling cookoff, capable of describing multiple materials simultaneously. To this end, the HPR model of continuum mechanics is for the first time combined with a one-step Arrhenius reaction model and applied to several test problems. Within this framework, two major novel developments are also presented:

1. A method for simulating slow cookoff that doesn't suffer from the problems associated with existing methods, described in Section 1.1

2. A method for simulating material interfaces with the HPR model, permitting heat conduction across the interfaces when desired

The second development enables multimaterial simulations with the HPR model, performed here for the first time. It also presents a simpler option than the current methods of coupling different systems of equations described in Section 1.1, as the HPR model is capable of describing solids and fluids (Newtonian and non-Newtonian).

The mathematical models used in this study are described in Section 1.3 and the background theory regarding ghost fluid methods (required for the second development described above) is detailed in Section 1.4. The numerical methods used in this study are described in Chapter 2 and validated in Chapter 3. Chapter 4 is solely composed of new theoretical material, including an explication of the two main developments of this study, and some more general mathematical results concerning the new framework proposed here. The feasibility of modeling combustive processes with the new framework is assessed numerically in Chapter 5. Development 1 is also tested here. Development 2 is tested numerically in Chapter 6. The numerical results are discussed in Chapter 7, where limitations and possible further improvements are suggested for the new methods presented. For completeness and reproducibility, the analytic forms of various quantities and the HPR system matrices are given in the appendices.

Owing to restrictions on time, only fluids were modeled within the new framework. Thus, "cookoff" refers here strictly to gaseous cookoff, and the multiphase problems encountered are strictly multimaterial problems. It is envisioned, however, that an extension of the results of this study to problems involving solids would be straightforward, and an explanation of how this would be achieved is given in Chapter 7.

1.3 Mathematical Models

The Model of Peshkov and Romenski

The HPR model, first introduced in Peshkov and Romenski [85] and expanded upon in Dumbser et al. [31], takes the following form:

$$\frac{\partial \rho}{\partial t} + \frac{\partial \left(\rho v_k\right)}{\partial x_k} = 0 \tag{1.2a}$$

$$\frac{\partial \left(\rho v_i\right)}{\partial t} + \frac{\partial (\rho v_i v_k + p\delta_{ik} - \sigma_{ik})}{\partial x_k} = 0 \tag{1.2b}$$

$$\frac{\partial A_{ij}}{\partial t} + \frac{\partial \left(A_{ik} v_k\right)}{\partial x_j} + v_k \left(\frac{\partial A_{ij}}{\partial x_k} - \frac{\partial A_{ik}}{\partial x_j}\right) = -\frac{\psi_{ij}}{\theta_1(\tau_1)} \tag{1.2c}$$

$$\frac{\partial \left(\rho J_i\right)}{\partial t} + \frac{\partial \left(\rho J_i v_k + T\delta_{ik}\right)}{\partial x_k} = -\frac{\rho H_i}{\theta_2\left(\tau_2\right)} \tag{1.2d}$$

$$\frac{\partial \left(\rho s\right)}{\partial t} + \frac{\partial \left(\rho s v_k + H_k\right)}{\partial x_k} = \frac{\rho}{\theta_1\left(\tau_1\right) T}\psi_{kl}\psi_{kl} + \frac{\rho}{\theta_2\left(\tau_2\right) T}H_k H_k \tag{1.2e}$$

where θ_1 and θ_2 are positive scalar functions, and $\psi = \frac{\partial E}{\partial A}$ and $\boldsymbol{H} = \frac{\partial E}{\partial \boldsymbol{J}}$. Entropy does not decrease during the dissipative time evolution:

$$\frac{\partial \left(\rho s\right)}{\partial t} + \frac{\partial \left(\rho s v_k + H_k\right)}{\partial x_k} \geq 0 \tag{1.3}$$

(1.2e) can be replaced with the following equation, which will be used instead when solving the model in this study:

$$\frac{\partial \left(\rho E\right)}{\partial t} + \frac{\partial \left(\rho E v_k + \left(p\delta_{ik} - \sigma_{ik}\right) v_i + q_k\right)}{\partial x_k} = 0 \tag{1.4}$$

(1.2a), (1.2b), (1.2c), (1.2d), (1.4) can be written in the following form, with $\boldsymbol{Q}, \boldsymbol{F}, \boldsymbol{B}, \boldsymbol{S}$ given in Chapter B and Chapter C:

$$\frac{\partial \boldsymbol{Q}}{\partial t} + \boldsymbol{\nabla} \cdot \boldsymbol{F} + \boldsymbol{B} \cdot \nabla \boldsymbol{Q} = \boldsymbol{S} \tag{1.5}$$

The following definitions are given:

$$p = \rho^2 \frac{\partial E}{\partial \rho} \tag{1.6a}$$

$$\sigma = -\rho A^T \frac{\partial E}{\partial A} \tag{1.6b}$$

$$T = \frac{\partial E}{\partial s} \tag{1.6c}$$

$$\boldsymbol{q} = \frac{\partial E}{\partial s} \frac{\partial E}{\partial \boldsymbol{J}} \tag{1.6d}$$

To close the system, the EOS must be specified, from which the above quantities and the sources can be derived. E is the sum of the contributions of the energies at the molecular scale (microscale), the material element[1] scale (mesoscale), and the flow scale (macroscale):

$$E = E_1 \left(\rho, s \right) + E_2 \left(A, \boldsymbol{J} \right) + E_3 \left(\boldsymbol{v} \right) \tag{1.7}$$

In this study, E_1 will either be the ideal gas EOS:

$$E_1 = \frac{c_0^2}{\gamma \left(\gamma - 1 \right)} = \frac{\rho^{\gamma-1} e^{\frac{s}{c_v}}}{\gamma - 1} \tag{1.8}$$

or the stiffened gas EOS:

$$E_1 = \frac{c_0^2}{\gamma \left(\gamma - 1 \right)} \left(\frac{\rho}{\rho_0} \right)^{\gamma-1} e^{\frac{s}{c_v}} + \frac{\rho_0 c_0^2 - \gamma p_\infty}{\gamma \rho} \tag{1.9}$$

Owing to the definition of the pressure, E_1 is thus given by:

$$E_1 = \frac{p + \gamma p_\infty}{\left(\gamma - 1 \right) \rho} \tag{1.10}$$

where $p_\infty = 0$ for an ideal gas. The temperature is given by:

$$T = \frac{p + p_\infty}{\left(\gamma - 1 \right) c_v \rho} \tag{1.11}$$

---

[1]The concept of a *material element* corresponds to that of a fluid parcel from fluid dynamics, applied to both fluids and solids.

and the speed of sound by:

$$c_0 = \sqrt{\frac{\gamma\left(p + p_\infty\right)}{\rho}} \tag{1.12}$$

E_2 is chosen to have the following quadratic form:

$$E_2 = \frac{c_s^2}{4}\left\|\mathrm{dev}\left(G\right)\right\|_F^2 + \frac{\alpha^2}{2}\left\|\boldsymbol{J}\right\|^2 \tag{1.13}$$

α is a constant related to the characteristic velocity of propagation of heat waves:

$$c_h = \frac{\alpha}{\rho}\sqrt{\frac{T}{c_v}} \tag{1.14}$$

$G = A^T A$ is the Gramian matrix of the distortion tensor, and $\mathrm{dev}\left(G\right)$ is the deviator (trace-free part) of G:

$$\mathrm{dev}\left(G\right) = G - \frac{1}{3}\,\mathrm{tr}\left(G\right)I \tag{1.15}$$

E_3 is the usual specific kinetic energy per unit mass:

$$E_3 = \frac{1}{2}\left\|\boldsymbol{v}\right\|^2 \tag{1.16}$$

The following forms are chosen:

$$\theta_1\left(\tau_1\right) = \frac{\tau_1 c_s^2}{3\left|A\right|^{\frac{5}{3}}} \tag{1.17a}$$

$$\theta_2\left(\tau_2\right) = \tau_2\alpha^2\frac{\rho T_0}{\rho_0 T} \tag{1.17b}$$

$$\tau_1 = \frac{6\mu}{\rho_0 c_s^2} \tag{1.18a}$$

$$\tau_2 = \frac{\rho_0\kappa}{T_0\alpha^2} \tag{1.18b}$$

11

The justification of these choices is that classical Navier–Stokes–Fourier theory is recovered in the stiff limit $\tau_1, \tau_2 \to 0$ [31]. This results in the following relations:

$$\sigma = -\rho c_s^2 G \operatorname{dev}(G) \tag{1.19a}$$

$$\boldsymbol{q} = \alpha^2 T \boldsymbol{J} \tag{1.19b}$$

$$-\frac{\psi}{\theta_1(\tau_1)} = -\frac{3}{\tau_1} |A|^{\frac{5}{3}} A \operatorname{dev}(G) \tag{1.19c}$$

$$-\frac{\rho \boldsymbol{H}}{\theta_2(\tau_2)} = -\frac{T\rho_0}{T_0 \tau_2} \boldsymbol{J} \tag{1.19d}$$

The following constraint also holds [85]:

$$\det(A) = \frac{\rho}{\rho_0} \tag{1.20}$$

The model as presented here has its roots in Godunov and Romenski's 1970s model of elastoplastic deformation [44]. The two models are very similar in structure. The differences lie in the physical interpretation of A, the appearance of algebraic source terms in the evolution equations for A, and the inclusion of thermal conduction by the evolution of $\boldsymbol{J}$. Whereas the earlier model described only solids, the new model seeks to describe fluids as well. In the former, A was viewed as describing the global deformation of the medium; it is now regarded as describing the local deformability of the material elements comprising the medium, containing information about their rotation and deformation. Unlike in previous continuum models, material elements have not only finite size, but also internal structure.

The strain dissipation time τ_1 of the HPR model is a continuous analogue of Frenkel's "particle settled life time" [39]; the characteristic time taken for a particle to move by a distance of the same order of magnitude as the particle's size. Thus, τ_1 characterises the time taken for a material element to rearrange with its neighbours. $\tau_1 = \infty$ for solids and $\tau_1 = 0$ for inviscid fluids. It is in this way that the HPR model seeks to describe all three major phases of matter, as long as a continuum description is appropriate for the material at hand.

The evolution equation for $\boldsymbol{J}$ and its contribution to the energy of the system are derived from Romenski's model of hyperbolic heat transfer, originally proposed in [71, 95] and implemented in [93, 94]. In this model, $\boldsymbol{J}$ is effectively defined as the

variable conjugate to the entropy flux, in the sense that the latter is the derivative of the specific internal energy with respect to $\boldsymbol{J}$. Romenski remarks that it is more convenient to evolve $\boldsymbol{J}$ and E than the heat flux or the entropy flux, and thus the equations take the form given here. $\boldsymbol{J}$ can intuitively be thought of as a thermal analogue of momentum. τ_2 characterises the speed of relaxation of the thermal impulse due to heat exchange between material elements.

Modeling Reactive Processes

In this study, when modeling reactive gases, the following equation is introduced alongside (1.2a), (1.2b), (1.2c), (1.2d), (1.4):

$$\frac{\partial (\rho \lambda)}{\partial t} + \frac{\partial (\rho \lambda v_k)}{\partial x_k} = -\rho \lambda K (T) \tag{1.21}$$

K is the rate of reaction - a function of temperature, whose form depends on the type of reaction kinetics used. The EOS (1.7) is modified to include:

$$E_r (\lambda) = -Q_c (1 - \lambda) \tag{1.22}$$

In discrete ignition temperature reaction kinetics, no reaction occurs below the ignition temperature, T_i. Above T_i, the reaction proceeds at a constant rate $K_0 > 0$:

$$K (T) = \begin{cases} K_0 & T \geq T_i \\ 0 & T < T_i \end{cases} \tag{1.23}$$

A more sophisticated model of reaction kinetics was devised by Svante Arrhenius in 1889 [6, 7]:

$$K (T) = B_c e^{-E_a/(R_c T)} \tag{1.24}$$

where B_c is some prefactor (with units of frequency), and E_a is the activation energy of the reactive species. Often, the system is characterised by the dimensionless inverse activation energy:

$$\epsilon = \frac{R_c T_0}{E_a} \tag{1.25}$$

1.4   Ghost Fluid Methods

Ghost fluid methods, combined with level set methods, are used to model the evolution of interfaces between different materials. They are detailed here, as it is with such a method that this study proposes to model the interfaces between different materials described by the HPR model.

Level Set Methods

Given a function f on $\mathbb{R}$, the level set of f at level c is defined as:

$$\Gamma_c = \{x : f(x) = c\} \tag{1.26}$$

Given velocity field $v : \mathbb{R} \to \mathbb{R}$, f is advected according to the level set equation [84]:

$$\frac{\partial f}{\partial t} = v \left| \frac{\partial f}{\partial x} \right| \tag{1.27}$$

The advection of a point in a fluid with velocity v can be modeled by taking $f = x - x_0$ where x_0 is the position of the point at time $t = 0$, and tracking Γ_0. (1.27) is solved by an appropriate numerical method. The numerical methods used in this study are described in Chapter 2. f will usually have to be renormalised to resemble a straight line at every time step, to avoid unwanted distortions such as becoming a multivalued function.

The Original Ghost Fluid Method

The Original Ghost Fluid Method of Fedkiw et al. [36] (an adaptation of the work of Glimm et al. [43]) is a numerical method for the Euler equations for simulating interfaces between multiple materials. The primitive variables for the Euler equations in 1D are given by $\boldsymbol{P} = \begin{pmatrix} \rho & v & p \end{pmatrix}^T$.

Suppose the interface between two fluids is modeled on spatial domain $[0, 1]$, divided into N cells with width $\Delta x = \frac{1}{N}$. Let the time step be Δt and let $\boldsymbol{P}_i^n$ be the set of primitive variables in cell i at time $t_n = n\Delta t$. Let the level set function f have root
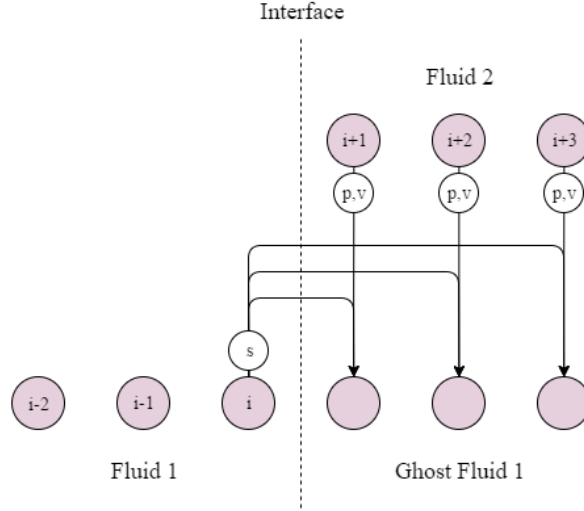
Figure 1.1: The Original Ghost Fluid Method

x_n where $x_n \in \left[\left(i + \frac{1}{2}\right)\Delta x, \left(i + \frac{3}{2}\right)\Delta x\right]$. Thus, at time t_n the interface lies between the cells with primitive variables $\boldsymbol{P}_i^n, \boldsymbol{P}_{i+1}^n$. Define two sets of primitive variables:

$$\boldsymbol{P}_j^{(1)} = \begin{cases} \boldsymbol{P}_j^n & j \leq i \\ \left(\rho\left(s_i^n, p_j^n, \gamma_i^n\right) \ v_j^n \ p_j^n\right) & j > i \end{cases} \tag{1.28}$$

$$\boldsymbol{P}_j^{(2)} = \begin{cases} \boldsymbol{P}_j^n & j \geq i+1 \\ \left(\rho\left(s_{i+1}^n, p_j^n, \gamma_{i+1}^n\right) \ v_j^n \ p_j^n\right) & j < i+1 \end{cases} \tag{1.29}$$

where:

$$\rho\left(s, p, \gamma\right) = \left(\frac{p}{s}\right)^{\frac{1}{\gamma}} \tag{1.30}$$

All cells in $\boldsymbol{P}^{(1)}$ to the left of the interface have the same state variables as those of $\boldsymbol{P}^n$. All cells to the right have the same pressure and velocity as their counterparts in $\boldsymbol{P}^n$, but the same entropy as $\boldsymbol{P}_i^n$. This affects their density. The situation is analogous for $\boldsymbol{P}^{(2)}$. This is demonstrated in Figure 1.1 on page 15.

$\boldsymbol{P}^{(1)}, \boldsymbol{P}^{(2)}$ are stepped forward by time step Δt using a standard Eulerian method. f is advected using (1.27), taking the velocity in each cell to be that of $\boldsymbol{P}^n$. Now let
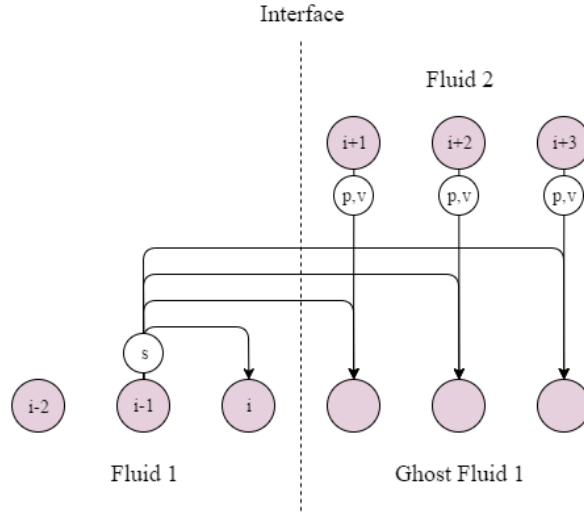
Figure 1.2: The Original Ghost Fluid Method, with the isobaric fix

$f(x_{n+1}) = 0$ where $x_{n+1} \in \left[\left(k + \frac{1}{2}\right)\Delta x, \left(k + \frac{3}{2}\right)\Delta x\right]$ for some k. Define:

$$\boldsymbol{P}_j^{n+1} = \begin{cases} \boldsymbol{P}_j^{(1)} & j \leq k \\ \boldsymbol{P}_j^{(2)} & j > k \end{cases} \tag{1.31}$$

The rationale behind the original GFM is that in most applications, pressure and velocity are continuous across the interface, and thus the ghost cells may take the real pressure and velocity values. Entropy is generally discontinuous at a contact discontinuity, resulting in large truncation errors if a standard finite difference scheme is used to solve the system. Thus, entropy is extrapolated as a constant from the interface boundary cell into the ghost region.

Fedkiw et al. advised to use the *isobaric fix* technique. This involves setting the entropy of cell i, and all cells in the right ghost region, to that of cell $i-1$, and setting the entropy of cell $i+1$, and all cells in the left ghost region, to that of cell $i+2$. This is demonstrated in Figure 1.2 on page 16.

Effectively, the ghost regions behave like they are composed of the same fluid as the regions they extend (as they have the same entropy), facilitating calculation of the next time step, but they have the same pressure and velocity profiles as the real fluids they replace, meaning the boundary conditions at the interface are upheld.
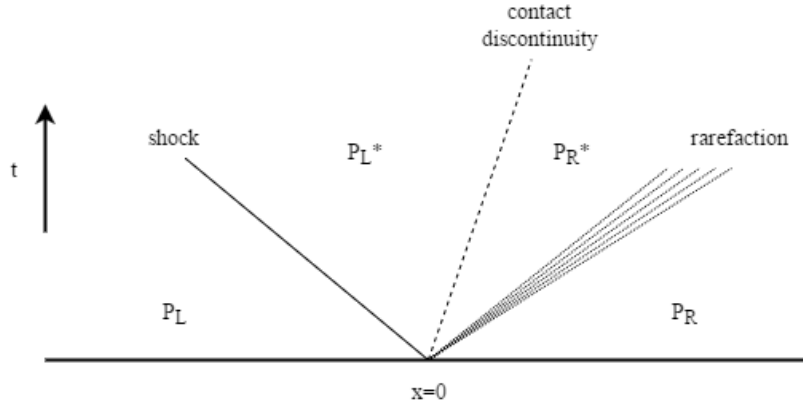
Figure 1.3: The qualitative structure of the solution to the Riemann Problem, showing the different possible types of waves

The Riemann Ghost Fluid Method

The Riemann Problem in its general form is the solution of the following initial value problem. Given a set of variables $\boldsymbol{P}$ dependent on space and time, and a hyperbolic set of equations which govern their spatio-temporal evolution, $\boldsymbol{P}\left(x, t\right)$ is sought for $t > 0$, given the initial condition:

$$\boldsymbol{P}\left(x, 0\right) = \begin{cases} \boldsymbol{P_L} & x < 0 \\ \boldsymbol{P_R} & x > 0 \end{cases} \tag{1.32}$$

This problem is denoted by $RP\left(\boldsymbol{P_L}, \boldsymbol{P_R}\right)$. Exact solvers exist for the Riemann Problem for various sets of governing equations, such as the Euler equations [112], the equations of non-linear elasticity [13], or the shallow water equations [5], among others. There also exist approximate solvers for general conservative [69, 77] or non-conservative [25] hyperbolic systems of PDEs. The references given here form a very small sample of the work that has been done in this area.

The solution of the Riemann Problem usually takes the form of a set of waves, between which $\boldsymbol{P}$ is constant. The waves can either be a contact discontinuity (across which pressure and velocity are continuous), a shock (across which all variables may be discontinuous), or a rarefaction (along which the variables vary continuously between their values on either side of the wave). The number and form of the waves are determined by the governing equations and the initial conditions. The states of the

17
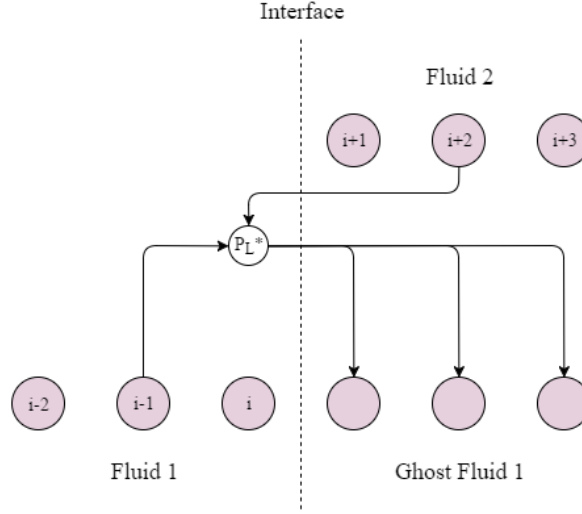
Figure 1.4: The Riemann Ghost Fluid Method

variables either side of the contact discontinuity in the middle are known as the *star states*. This qualitative description is depicted in Figure 1.3 on page 17.

Liu et al. [68] demonstrated that the original GFM fails to resolve strong shocks at material interfaces. This is because the method effectively solves two separate single-fluid Riemann problems. The waves present in these Riemann problems do not necessarily correspond to those in the real Riemann problem across the interface. The Riemann Ghost Fluid Method of Sambasivan et al. [98] aims to rectify this.

Given $\boldsymbol{P}^n$ and $x_n \in \left[\left(i + \frac{1}{2}\right)\Delta x, \left(i + \frac{3}{2}\right)\Delta x\right]$, the ghost cells for fluid 1 are populated with the left star state of $RP\left(\boldsymbol{P}^n_{i-1}, \boldsymbol{P}^n_{i+2}\right)$, and the ghost cells for fluid 2 are populated with the right star state. $RP\left(\boldsymbol{P}^n_{i-1}, \boldsymbol{P}^n_{i+2}\right)$ is solved rather than $RP\left(\boldsymbol{P}^n_i, \boldsymbol{P}^n_{i+1}\right)$, as $\boldsymbol{P}^n_i, \boldsymbol{P}^n_{i+1}$ often contain errors generated by the fact that they lie on the material interface. $\boldsymbol{P}^{n+1}$ is then generated as before from the newly formed $\boldsymbol{P}^{(1)}, \boldsymbol{P}^{(2)}$. This process is demonstrated in Figure 1.4 on page 18.

Chapter 2

Numerical Methods

The HPR model, being non-conservative, with stiff source terms, represents a particularly challenging set of PDEs. In this study they are solved by an ADER-WENO method. First, the cell-wise constant state variable data from the current time step is reconstructed using high-order spatial polynomials according to the WENO method. This reconstruction is then extended to a reconstruction in both space and time for each individual cell in the domain, using the Discontinuous Galerkin method. A finite volume solver is then used to couple neighbouring cells and produce the cell-wise constant data at the next time step. In this study, all simulations were performed in 1D. The methods presented here are easily extensible to higher dimensions, however.

Although this process has been demonstrated to be effective in solving the HPR system [16, 31], it was originally designed for problems involving moving meshes, and is probably more involved than necessary to perform the simulations in this study. The DG step in particular is relatively computationally taxing. The purpose of this study, however, was not to investigate more efficient solution methods for this particular system (see Sverdrup [109] for the latest work on this problem). It was therefore decided that this procedure would be used, being the only confirmed method of solution publicly available.

2.1 The WENO Reconstruction

First introduced by Liu et al. [70] and developed by Jiang and Shu [59], WENO methods are used to produce high order polynomial approximations to piece-wise constant data. In this study, the modified method of Dumbser et al. [35] is used.

Consider the domain $[0, L]$. Take $K, N \in \mathbb{N}$. Take the set of grid points $x_i = \frac{i \cdot L}{K}$ for $i = 0, \ldots, K$ and let $\Delta x = \frac{L}{K}$. Denote cell $[x_i, x_{i+1}]$ by C_i. Given cell-wise constant data u on $[0, L]$, an order $N + 1$ accurate polynomial reconstruction of u in C_i will be performed. Define the scaled space variable:

$$\chi^i = \frac{1}{\Delta x} (x - x_i) \tag{2.1}$$

Denoting the Gauss-Legendre abscissae on $[0,1]$ by $\{\chi_0, \ldots, \chi_N\}$, define the nodal basis of order N: the Lagrange interpolating polynomials $\{\psi_0, \ldots, \psi_N\}$ with the following property:

$$\psi_i\left(\chi_j\right) = \delta_{ij} \tag{2.2}$$

If N is even, take the stencils:

$$\begin{cases} S_1 & = \left\{C_{i-\frac{N}{2}}, \ldots, C_{i+\frac{N}{2}}\right\} \\ S_2 & = \{C_{i-N}, \ldots, C_i\} \\ S_3 & = \{C_i, \ldots, C_{i+N}\} \end{cases} \tag{2.3}$$

If N is odd, take the stencils:

$$\begin{cases} S_1 & = \left\{C_{i-\lfloor\frac{N}{2}\rfloor}, \ldots, C_{i+\lceil\frac{N}{2}\rceil}\right\} \\ S_2 & = \left\{C_{i-\lceil\frac{N}{2}\rceil}, \ldots, C_{i+\lfloor\frac{N}{2}\rfloor}\right\} \\ S_3 & = \{C_{i-N}, \ldots, C_i\} \\ S_4 & = \{C_i, \ldots, C_{i+N}\} \end{cases} \tag{2.4}$$

The data is reconstructed on S_j as:

$$\sum_p \psi_p\left(\chi^i\left(x\right)\right) \hat{w}_p^{ij} \tag{2.5}$$

where the $\hat{w}_p^{ij}$ are solutions to the following linear system:

$$\frac{1}{\Delta x} \int_{x_k}^{x_{k+1}} \psi_p\left(\chi^k\left(x\right)\right) \hat{w}_p^{ij} dx = u_k \qquad \forall C_k \in S_j \tag{2.6}$$

where u_k is the value of u in C_k. Define the oscillation indicator matrix:

$$\Sigma_{mn} = \sum_{\alpha=1}^N \int_0^1 \psi_m^{(\alpha)} \psi_n^{(\alpha)} d\chi \tag{2.7}$$

and the oscillation indicator for each stencil:

$$o_j = \Sigma_{mn} \hat{w}_m^{ij} \hat{w}_n^{ij} \tag{2.8}$$

The full reconstruction in C_i is:

$$w_i(x) = \sum_p \psi_p\left(\chi^i(x)\right) \hat{w}_p^i \tag{2.9}$$

where $\hat{w}_p^i = \omega_j \hat{w}_p^{ij}$ is the weighted coefficient of the pth basis function, with weights:

$$\omega_j = \frac{\tilde{\omega}_j}{\sum_k \tilde{\omega}_k} \qquad \tilde{\omega}_j = \frac{\zeta_j}{(o_s + \varepsilon)^r} \tag{2.10}$$

In this study, $r = 8$, $\varepsilon = 10^{-14}$, $\zeta_j = 10^5$ if S_j is a central stencil, and $\zeta_j = 1$ if S_j is a side stencil, as in [30].

2.2 The Discontinuous Galerkin Predictor

Take a non-conservative, hyperbolic system of the form:

$$\frac{\partial \boldsymbol{Q}}{\partial t} + \frac{\partial \boldsymbol{F}(\boldsymbol{Q})}{\partial x} + B(\boldsymbol{Q}) \cdot \frac{\partial \boldsymbol{Q}}{\partial x} = \boldsymbol{S}(\boldsymbol{Q}) \tag{2.11}$$

where $\boldsymbol{Q}$ is the vector of conserved variables, $\boldsymbol{F}$ is the conservative nonlinear flux, B is the block matrix corresponding to the purely non-conservative component of the system, and $\boldsymbol{S}(\boldsymbol{Q})$ is the algebraic source vector. Defining $M = \frac{\partial \boldsymbol{F}}{\partial \boldsymbol{Q}} + B$ this becomes:

$$\frac{\partial \boldsymbol{Q}}{\partial t} + M(\boldsymbol{Q}) \cdot \frac{\partial \boldsymbol{Q}}{\partial x} = \boldsymbol{S}(\boldsymbol{Q}) \tag{2.12}$$

Take the grid for the previous section, and time steps $t_0 < t_1 < \ldots$ while defining $\Delta t_n = t_{n+1} - t_n$. Combining the techniques presented in [27, 30], the Discontinuous Galerkin method produces at each time step t_n a local polynomial approximation to $\boldsymbol{Q}$ on each space-time cell $C_i \times [t_n, t_{n+1}]$.

Define the scaled time variable:

$$\tau^n = \frac{1}{\Delta t_n}\left(t - t_n\right) \tag{2.13}$$

Using these variables gives:

$$\frac{\partial \boldsymbol{Q}}{\partial \tau^n} + \frac{\partial \boldsymbol{F}^*\left(\boldsymbol{Q}\right)}{\partial \chi^i} + B^*\left(\boldsymbol{Q}\right)\cdot\frac{\partial \boldsymbol{Q}}{\partial \chi^i} = \boldsymbol{S}^*\left(\boldsymbol{Q}\right) \tag{2.14}$$

where

$$\boldsymbol{F}^* = \frac{\Delta t_n}{\Delta x}\boldsymbol{F} \qquad B^* = \frac{\Delta t_n}{\Delta x}B \qquad \boldsymbol{S}^* = \Delta t_n \boldsymbol{S} \tag{2.15}$$

The non-dimensionalisation notation and spacetime cell indexing notation will be dropped for simplicity in what follows. Using the same nodal basis as in the previous section, define the set of spatio-temporal basis functions:

$$\left\{\theta_k\left(\chi,\tau\right) = \psi_p\left(\chi\right)\psi_s\left(\tau\right) : 0 \leq p, s \leq N\right\} \tag{2.16}$$

The *nodal basis representation* is the following set of approximations:

$$\boldsymbol{Q} \approx \boldsymbol{q_h} = \theta_\beta \boldsymbol{q_\beta} \tag{2.17a}$$

$$\boldsymbol{F}\left(\boldsymbol{Q}\right) \approx \theta_\beta \boldsymbol{F}\left(\boldsymbol{q_\beta}\right) \tag{2.17b}$$

$$B\left(\boldsymbol{Q}\right)\cdot\frac{\partial \boldsymbol{Q}}{\partial \chi} \approx \theta_\beta B\left(\boldsymbol{q_\beta}\right)\cdot\left(\frac{\partial \theta_\gamma\left(\chi_\beta,\tau_\beta\right)}{\partial \chi}\boldsymbol{q_\gamma}\right) \tag{2.17c}$$

$$\boldsymbol{S}\left(\boldsymbol{Q}\right) \approx \theta_\beta \boldsymbol{S}\left(\boldsymbol{q_\beta}\right) \tag{2.17d}$$

where $\left(\chi_\beta, \tau_\beta\right)$ are the coordinates of the Legendre node corresponding to basis function θ_β. Define the integral operators:

$$\left[f, g\right]^\tau = \int_0^1 f\left(\chi,\tau\right)g\left(\chi,\tau\right)d\chi \tag{2.18a}$$

$$\langle f, g\rangle = \int_0^1 \int_0^1 f\left(\chi,\tau\right)g\left(\chi,\tau\right)d\chi d\tau \tag{2.18b}$$

Using the nodal basis representation, multiplying (2.14) by test function θ_α and integrating over space and time gives:

$$\left\langle \theta_\alpha, \frac{\partial \theta_\beta}{\partial \tau} \right\rangle \boldsymbol{q}_\beta = - \left\langle \theta_\alpha, \frac{\partial \theta_\beta}{\partial \chi} \right\rangle \boldsymbol{F}(\boldsymbol{q}_\beta) \tag{2.19}$$

$$+ \langle \theta_\alpha, \theta_\beta \rangle \left(\boldsymbol{S}(\boldsymbol{q}_\beta) - B(\boldsymbol{q}_\beta) \cdot \left(\frac{\partial \theta_\gamma(\chi_\beta, \tau_\beta)}{\partial \chi} \boldsymbol{q}_\gamma \right) \right) \tag{2.20}$$

Integrating by parts in time gives:

$$\left([\theta_\alpha, \theta_\beta]^1 - \left\langle \frac{\partial \theta_\alpha}{\partial \tau}, \theta_\beta \right\rangle \right) \boldsymbol{q}_\beta = [\theta_\alpha, \boldsymbol{w}]^0 - \left\langle \theta_\alpha, \frac{\partial \theta_\beta}{\partial \chi} \right\rangle \boldsymbol{F}(\boldsymbol{q}_\beta) \tag{2.21}$$

$$+ \langle \theta_\alpha, \theta_\beta \rangle \left(\boldsymbol{S}(\boldsymbol{q}_\beta) - B(\boldsymbol{q}_\beta) \cdot \left(\frac{\partial \theta_\gamma(\chi_\beta, \tau_\beta)}{\partial \chi} \boldsymbol{q}_\gamma \right) \right)$$

where $\boldsymbol{w} = \boldsymbol{w}_\gamma \psi_\gamma$ is the reconstruction obtained at the start of the time step with the WENO method. Define the following notation:

$$U_{\alpha\beta} = [\theta_\alpha, \theta_\beta]^1 - \left\langle \frac{\partial \theta_\alpha}{\partial \tau}, \theta_\beta \right\rangle \tag{2.22a}$$

$$V_{\alpha\beta} = \left\langle \theta_\alpha, \frac{\partial \theta_\beta}{\partial \chi} \right\rangle \tag{2.22b}$$

$$W_{\alpha\gamma} = [\theta_\alpha, \psi_\gamma]^0 \tag{2.22c}$$

$$Z_{\alpha\beta} = \langle \theta_\alpha, \theta_\beta \rangle \tag{2.22d}$$

Thus:

$$U_{\alpha\beta}\boldsymbol{q}_\beta = W_{\alpha\gamma}\boldsymbol{w}_\gamma - V_{\alpha\beta}\boldsymbol{F}(\boldsymbol{q}_\beta) + Z_{\alpha\beta}\left(\boldsymbol{S}(\boldsymbol{q}_\beta) - B(\boldsymbol{q}_\beta) \cdot \left(\frac{\partial \theta_\gamma(\chi_\beta, \tau_\beta)}{\partial \chi} \boldsymbol{q}_\gamma \right) \right) \tag{2.23}$$

This nonlinear system in $\boldsymbol{q}_\beta$ is solved by a Newton method. The source terms must be solved implicitly if they are stiff.

The Predictor Initial Guess

Let the initial guess for the nonlinear system of the DG predictor be $\boldsymbol{q}_h^0 = \theta_k \hat{\boldsymbol{q}}_k$. In [29] this is taken to be the WENO reconstruction, i.e. $\boldsymbol{q}_h^0(\chi, \tau) = \boldsymbol{w}(\chi)$ for $\tau \in [0, 1]$.

In [52], a more sophisticated initial guess is used for systems of the form (2.11) with $B = 0$. Denote the Gauss-Legendre abscissae on $[0, 1]$ by $\{\tau_0, \ldots, \tau_N\}$. Let $\Delta\tau_j = \tau_{j+1} - \tau_j$. Letting $\boldsymbol{q}_h^0 = \psi_i(\chi)\,\psi_j(\tau)\,\hat{\boldsymbol{q}}_{ij}$:

$$\hat{\boldsymbol{q}}_{i,j+1} = \hat{\boldsymbol{q}}_{ij} - \Delta\tau_j \frac{\partial \boldsymbol{F}(\hat{\boldsymbol{q}}_{ij})}{\partial x} + \frac{\Delta\tau_j}{2}\left(\boldsymbol{S}(\hat{\boldsymbol{q}}_{i,j+1}) + \boldsymbol{S}(\hat{\boldsymbol{q}}_{ij})\right) \tag{2.24a}$$

$$\hat{\boldsymbol{q}}_{i0} = \boldsymbol{w}_i \tag{2.24b}$$

An explicit second order Taylor method is used to solve the flux term, combined with a second order Crank–Nicholson scheme for the stiff source term. In this study, this method was adapted to deal with the non-conservative terms:

$$\hat{\boldsymbol{q}}_{i,j+1} = \hat{\boldsymbol{q}}_{ij} - \Delta\tau_j M(\hat{\boldsymbol{q}}_{ij}) \cdot \left(\frac{\partial \psi_k}{\partial \chi}\hat{\boldsymbol{q}}_{kj}\right) + \frac{\Delta\tau_j}{2}\left(\boldsymbol{S}(\hat{\boldsymbol{q}}_{i,j+1}) + \boldsymbol{S}(\hat{\boldsymbol{q}}_{ij})\right) \tag{2.25a}$$

$$\hat{\boldsymbol{q}}_{i0} = \boldsymbol{w}_i \tag{2.25b}$$

where M is given in (2.12). The Taylor method for the flux term is no longer necessary. The system was solved by a Newton method to deal with the stiff source term.

It was found that the more sophisticated initial guess would reduce overall computation times on some problems, owing to a faster convergence of the DG calculation. On other problems, the total computation time would increase, owing to the added cost of calculating the initial guess. See [26, 28, 34] for other choices for the initial guess.

2.3 The Finite Volume Scheme

Following the formulation of [30], integrating (2.11) over $[t_n, t_{n+1}] \times C_i$ gives:

$$\boldsymbol{Q}_i^{n+1} = \boldsymbol{Q}_i^n + \Delta t_n\left(\boldsymbol{S}_i^n - \boldsymbol{P}_i^n\right) - \frac{\Delta t_n}{\Delta x}\left(\boldsymbol{D}_{i+1}^n - \boldsymbol{D}_i^n\right) \tag{2.26}$$

where

$$\boldsymbol{Q}_i^n = \frac{1}{\Delta x} \int_{x_i}^{x_{i+1}} \boldsymbol{Q}\left(x, t_n\right) dx \tag{2.27a}$$

$$\boldsymbol{S}_i^n = \frac{1}{\Delta t_n \Delta x} \int_{t_n}^{t_{n+1}} \int_{x_i}^{x_{i+1}} \boldsymbol{S}\left(\boldsymbol{Q}\right) dx dt \tag{2.27b}$$

$$\boldsymbol{P}_i^n = \frac{1}{\Delta t_n \Delta x} \int_{t_n}^{t_{n+1}} \int_{x_i}^{x_{i+1}} B\left(\boldsymbol{Q}\right) \cdot \frac{\partial \boldsymbol{Q}}{\partial x} dx dt \tag{2.27c}$$

$$\boldsymbol{D}_i^n = \frac{1}{\Delta t_n} \int_{t_n}^{t_{n+1}} \boldsymbol{\mathcal{D}}\left(\boldsymbol{Q}^-\left(x_i, t\right), \boldsymbol{Q}^+\left(x_i, t\right)\right) dt \tag{2.27d}$$

$\boldsymbol{Q}^-, \boldsymbol{Q}^+$ are the left and right extrapolated states at the x_i boundary. $\boldsymbol{S}_i^n, \boldsymbol{P}_i^n, \boldsymbol{D}_i^n$ are calculated using an $N+1$-point Gauss-Legendre quadrature, replacing $\boldsymbol{Q}$ with $\boldsymbol{q_h}$.

M, as defined in Section 2.2, is a diagonalisable matrix with decomposition $M = R \Lambda R^{-1}$ where the columns of R are the right eigenvectors and Λ is the diagonal matrix of eigenvalues. Define the following matrix:

$$|M| = R\left|\Lambda\right| R^{-1} \tag{2.28}$$

Using these definitions, the interface terms arising in the FV formula have the following form:

$$\boldsymbol{\mathcal{D}}\left(\boldsymbol{q}^-, \boldsymbol{q}^+\right) = \frac{1}{2}\left(\boldsymbol{F}\left(\boldsymbol{q}^-\right) + \boldsymbol{F}\left(\boldsymbol{q}^+\right) + \hat{B} \cdot \left(\boldsymbol{q}^+ - \boldsymbol{q}^-\right) - \hat{M} \cdot \left(\boldsymbol{q}^+ - \boldsymbol{q}^-\right)\right) \tag{2.29}$$

$\hat{M}$ is chosen to either correspond to a Rusanov/Lax-Friedrichs flux [112]:

$$\hat{M} = \max\left(\max\left|\Lambda\left(\boldsymbol{q}^-\right)\right|, \max\left|\Lambda\left(\boldsymbol{q}^+\right)\right|\right) \tag{2.30}$$

or a simplified Osher–Solomon flux [32, 33]:

$$\hat{M} = \int_0^1 \left|M\left(\boldsymbol{q}^- + z\left(\boldsymbol{q}^+ - \boldsymbol{q}^-\right)\right)\right| dz \tag{2.31}$$

$\hat{B}$ takes the following form:

$$\hat{B} = \int_0^1 B\left(\boldsymbol{q}^- + z\left(\boldsymbol{q}^+ - \boldsymbol{q}^-\right)\right) dz \tag{2.32}$$

It was found that the Osher-Solomon flux would often produce slightly less diffusive results, but that it was more computationally expensive, and also had a greater tendency to introduce numerical artefacts.

2.4 Time Step and Boundary Conditions

Let Λ_i^n be the set of eigenvalues of the HPR system evaluated at $\boldsymbol{Q_i^n}$. $C_{cfl} < 1$ is a constant (usually taken to be 0.9, unless the problem being simulated is particularly demanding, requiring a lower value). A semi-analytic form for Λ is given in Section 4.3. The eigenvalues determine the speed of propagation of information in the solution to the Riemann Problem at the cell interfaces, and the time step is chosen to ensure that the characteristics do not enter into other cells between t_n and t_{n+1}:

$$\Delta t_n = \frac{C_{cfl} \cdot \Delta x}{\max_i |\Lambda_i^n|} \tag{2.33}$$

Transmissive boundary conditions (allowing material and heat to pass through) are implemented by setting the state variables in the boundary cells to the same value as their non-boundary neighbours. Reflective boundary conditions are implemented in the same way, except that the directions of the velocity and thermal impulse vectors in the boundary cells are reversed. Where fixed temperature boundary conditions are used, reflective boundary conditions are first imposed, after which the pressure is altered so that the boundary cell has the desired temperature T_{fixed}:

$$p = \rho \left(\gamma - 1 \right) c_v T_{fixed} - p_\infty \tag{2.34}$$

Where a fixed boundary heat flux q is specified, the quantity $\frac{q \cdot \Delta t}{\Delta x}$ is added to the value of ρE in the boundary cell. It may be appropriate to also fix $\boldsymbol{J}$ in the boundary cell in accordance with the specified heat flux (as $\boldsymbol{q} = \alpha^2 T \boldsymbol{J}$), but this was not done here, as no analogous procedure was undertaken in the studies with which this study compares its results. The effect of this measure is a potential area of further research.

2.5 Operator Splitting

Although not applicable to the full HPR system in the form given here, the operator splitting method is used when solving the reduced HPR system in slow cookoff simulations. Take the following conservative hyperbolic system with sources:

$$\frac{\partial \boldsymbol{Q}}{\partial t} + \frac{\partial \boldsymbol{F}(\boldsymbol{Q})}{\partial x} = \boldsymbol{S}(\boldsymbol{Q}) \tag{2.35}$$

At time step n, using $\boldsymbol{Q^n}$ as initial data, the homogeneous system is evolved by time step Δt to produce an intermediate state $\tilde{\boldsymbol{Q}}^{n+1}$:

$$\frac{\partial \boldsymbol{Q}}{\partial t} + \frac{\partial \boldsymbol{F}(\boldsymbol{Q})}{\partial x} = \boldsymbol{0} \tag{2.36}$$

There exist many methods with which to accomplish this (see Toro for an overview [112]). In this study, the following scheme is used:

$$\tilde{\boldsymbol{Q}}_i^{n+1} = \boldsymbol{Q}_i^n + \frac{\Delta t}{\Delta x}\left(\boldsymbol{F}_{i+\frac{1}{2}} - \boldsymbol{F}_{i-\frac{1}{2}}\right) \tag{2.37}$$

The subscript $i+\frac{1}{2}$ is used to denote the value between cells i and $i+1$. $\boldsymbol{F}_{i+\frac{1}{2}}$ was chosen to be the first-order First-Order Centred flux of Toro [111]:

$$\boldsymbol{F}_{i+\frac{1}{2}} = \frac{1}{2}\left(\boldsymbol{F}_{i+\frac{1}{2}}^{LF} + \boldsymbol{F}_{i+\frac{1}{2}}^{RI}\right) \tag{2.38}$$

where $\boldsymbol{F}_{i+\frac{1}{2}}^{LF}$ is the Lax-Friedrichs flux:

$$\boldsymbol{F}_{i+\frac{1}{2}}^{LF} = \frac{1}{2}\left(\boldsymbol{F}(\boldsymbol{Q}_i) + \boldsymbol{F}(\boldsymbol{Q}_{i+1})\right) + \frac{1}{2}\frac{\Delta x}{\Delta t}\left(\boldsymbol{Q}_i - \boldsymbol{Q}_{i+1}\right) \tag{2.39}$$

and $\boldsymbol{F}_{i+\frac{1}{2}}^{RI}$ is the Richtmyer flux [91]:

$$\boldsymbol{Q}_{i+\frac{1}{2}}^{RI} = \frac{1}{2}\left(\boldsymbol{Q}_i + \boldsymbol{Q}_{i+1}\right) + \frac{1}{2}\frac{\Delta t}{\Delta x}\left(\boldsymbol{F}(\boldsymbol{Q}_i) - \boldsymbol{F}(\boldsymbol{Q}_{i+1})\right) \tag{2.40a}$$
$$\boldsymbol{F}_{i+\frac{1}{2}}^{RI} = \boldsymbol{F}\left(\boldsymbol{Q}_{i+\frac{1}{2}}^{RI}\right) \tag{2.40b}$$
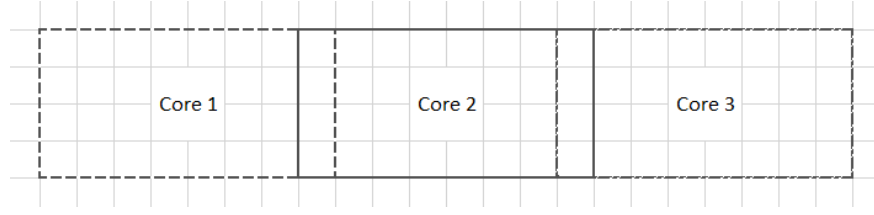
Figure 2.1: Overlapping groups of cells assigned to different computational cores during the Discontinuous Galerkin and Finite Volume steps

Next, $\boldsymbol{Q}_i^{\tilde{n}+1}$ is used as initial data to the following system of ODEs.

$$\frac{d\boldsymbol{Q}}{dt} = \boldsymbol{S}\left(\boldsymbol{Q}\left(t\right)\right) \tag{2.41}$$

This system is evolved by time step Δt to produce $\boldsymbol{Q}_i^{n+1}$. There are many ways to achieve this, both analytical and numerical. Only analytical methods are used in this study.

2.6 Computational Considerations

The solution of the nonlinear Discontinuous Galerkin system and the calculation of the Finite Volume interface terms are the most computationally taxing parts of the ADER-WENO scheme. Luckily, they are also trivially parallelisable. The DG predictor is calculated locally to each cell, so once the WENO reconstruction has been produced across the domain, each cell can be assigned to a core and no inter-process communication is required. To perform the FV step for a cell, information from its neighbours is required. Thus, blocks of cells are assigned to each core, with overlapping sections one cell thick, as demonstrated in Figure 2.1 on page 28.

The WENO and DG system matrices are precalculated and stored, to avoid having to calculate them at every time step. Analytic forms of various quantities (such as (4.32a), (4.35), (4.37), or those found in the appendices) are used wherever possible, for reasons of speed and accuracy.

The algorithmic implementations in this study were performed using the Python programming language, as the resulting speed and ease of development were desirable when dealing with the large amount of new theoretical material encountered. Heavy

use was made of the NumPy library for its data structures, and the SciPy library [61] for its multidimensional root finding algorithms. Both libraries were compiled against the Intel Math Kernel Library [2] for speed. Performance-critical sections of code were either compiled to machine code using the Numba library [65], or were implemented using direct calls to the relevant BLAS and LAPACK functions. Thus, much of the usual performance hits associated with using Python rather than a lower-level language such as C++ or Fortran were avoided. The joblib library was used to parallelise the DG and FV calculations, and the SymPy library (part of the SciPy/NumPy stack) was used to confirm the analytic forms of the system matrices and eigenstructure of the HPR model, given in Chapter C and Section 4.3, respectively. The plots in this dissertation were generated with the matplotlib library.

Chapter 3

Validation of Numerical Methods

3.1 Slow Opposing Shear Flow

This problem, incorrectly referred to as Stokes' First Problem in [31][1], is one of the few test cases with an analytic solution for the Navier-Stokes equations. The problem consists of two ideal gases in an infinite domain, meeting at the plane $x = 0$, initially flowing with equal and opposite velocity ± 0.1 in the y-axis. The initial conditions are given in Table 3.1 on page 30.

The flow has a low Mach number of 0.1, and this test case is designed to demonstrate the efficacy of the numerical methods in this flow regime. The exact solution to the Navier-Stokes equations is given by[2]:

$$v = v_0 \operatorname{erf}\left(\frac{x}{2\sqrt{\mu t}}\right) \tag{3.1}$$

The viscosity is variously taken to be $\mu = 10^{-2}$, $\mu = 10^{-3}$, $\mu = 10^{-4}$. Heat conduction is neglected, and $\gamma = 1.4$, $c_v = 1$, $\rho_0 = 1$, $c_s = 1$. The results of simulations with 200 cells at time $t = 1$ are presented in Figure 3.1 on page 31. The HPR results closely match the exact Navier-Stokes solution.

	ρ	p	$\boldsymbol{v}$	A	$\boldsymbol{J}$
$x < 0$	1	$1/\gamma$	$(0, -0.1, 0)$	I_3	$\boldsymbol{0}$
$x \geq 0$	1	$1/\gamma$	$(0, 0.1, 0)$	I_3	$\boldsymbol{0}$

Table 3.1: Initial conditions for the slow opposing shear flow test

---

[1]See the original papers of Stokes [107] and Rayleigh [88], and the analysis of Schlichting [100] for Stokes' First Problem, which is similar to the problem presented here, and also has an analytic solution for the Navier-Stokes equations.

[2]In this problem, the Navier-Stokes equations reduce to $v_t = \mu v_{xx}$. Defining $\eta = \frac{x}{2\sqrt{\mu t}}$, and assuming $v = f(\eta)$, this becomes $f'' + 2\eta f' = 0$. The result follows by solving this equation with the boundary conditions $v(\pm\infty) = \pm v_0$.
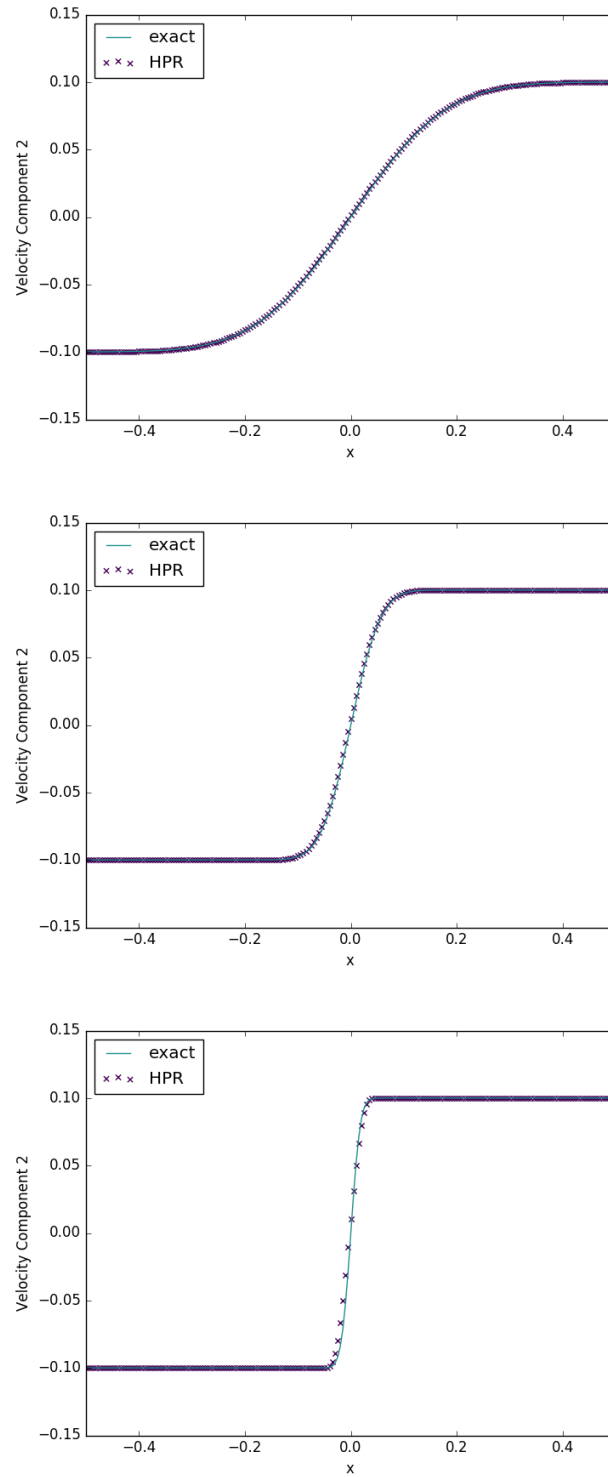
Figure 3.1: Velocity component 2 for the slow opposing shear flow test for viscosities $\mu = 10^{-2}$, $\mu = 10^{-3}$, $\mu = 10^{-4}$ (from top to bottom)

3.2   Viscous Shock

This test is designed to demonstrate that the numerical methods used are also able to cope with fast flows. First demonstrated by Becker [15], the Navier-Stokes equations have an analytic solution for $P_r = 0.75$ (see Johnson [60] for a full analysis). As noted by Dumbser [31], if the wave has nondimensionalised upstream velocity $\bar{v} = 1$ and Mach number M_c, then its nondimensionalised downstream velocity is:

$$a = \frac{1 + \frac{\gamma-1}{2}M_c^2}{\frac{\gamma+1}{2}M_c^2} \tag{3.2}$$

The wave's velocity profile $\bar{v}(x)$ is given by the roots of the following equation:

$$\frac{1 - \bar{v}}{(\bar{v} - a)^a} = c_1 \exp(-c_2 x) \tag{3.3a}$$

$$c_1 = \left(\frac{1-a}{2}\right)^{1-a} \tag{3.3b}$$

$$c_2 = \frac{3}{4}R_e \frac{M_c^2 - 1}{\gamma M_c^2} \tag{3.3c}$$

c_1, c_2 are constants that affect the position of the center of the wave, and its stretch factor, respectively. Following the analysis of Morduchow and Libby [80], the nondimensional pressure and density profiles are given by:

$$\bar{p} = \frac{1}{\bar{v}}\left(1 + \frac{\gamma-1}{2}M_c^2\left(1 - \bar{v}^2\right)\right) \tag{3.4}$$

$$\bar{\rho} = \frac{1}{\bar{v}} \tag{3.5}$$

To obtain an unsteady shock traveling into a region at rest, a constant velocity field $v = M_c c_0$ is imposed on the traveling wave solution presented here. Thus, if p_0, ρ_0 are the downstream (reference) values for pressure and density:

$$v = M c_0 (1 - \bar{v}) \tag{3.6a}$$

$$p = p_0 \bar{p} \tag{3.6b}$$

$$\rho = \rho_0 \bar{\rho} \tag{3.6c}$$

	ρ	p	$\boldsymbol{v}$	A	$\boldsymbol{J}$
$x < 0$	2	1	$\boldsymbol{0}$	$\sqrt[3]{2} \cdot I_3$	$\boldsymbol{0}$
$x \geq 0$	0.5	1	$\boldsymbol{0}$	$\frac{1}{\sqrt[3]{2}} \cdot I_3$	$\boldsymbol{0}$

Table 3.2: Initial conditions for the heat conduction test

These functions are used as initial conditions, along with $A = \sqrt[3]{\bar{\rho}}I$ and $\boldsymbol{J} = \boldsymbol{0}$. The downstream density and pressure are taken to be $\rho_0 = 1$ and $p_0 = \frac{1}{\gamma}$ (so that $c_0 = 1$). $M_c = 2$ and $R_e = 100$. The material parameters are taken to be: $\gamma = 1.4$, $p_\infty = 0$, $c_v = 2.5$, $c_s = 5$, $\alpha = 5$, $\mu = 2 \times 10^{-2}$, $\kappa = \frac{28}{3} \times 10^{-2}$.

The results of a simulation with 200 cells at time $t = 0.2$ are presented in Figure 3.2 on page 34. The shock was initially centered at $x = 0.25$, reaching $x = 0.65$ at the final time. The results match very well those found in [31], except that the spurious wave appearing in that study does not seem to appear here.

3.3   Heat Conduction

This is a simple test case to ensure that the heat transfer terms in the implementation are working correctly. Two ideal gases at different temperatures are initially in contact at position $x = 0$. The initial conditions for this problem are given in Table 3.2 on page 33.

The material parameters are taken to be: $\gamma = 1.4$, $c_v = 2.5$, $\rho_0 = 1$, $p_0 = 1$, $c_s = 1$, $\alpha = 2$, $\mu = 10^{-2}$, $\kappa = 10^{-2}$. The results of a simulation with 200 cells at time $t = 1$ are presented in Figure 3.3 on page 35. Note the excellent agreement with the results in [31] for both the HPR model, and the Navier-Stokes equations with the classical Fourier heat flux equation.

3.4   Semenov's Explosion Test

This test ensures that the Arrhenius reaction terms are working correctly. The test consists of a homogeneous, combustible, ideal gas at rest, initially at a temperature at which an Arrhenius reaction will start to occur, eventually leading to full combustion.
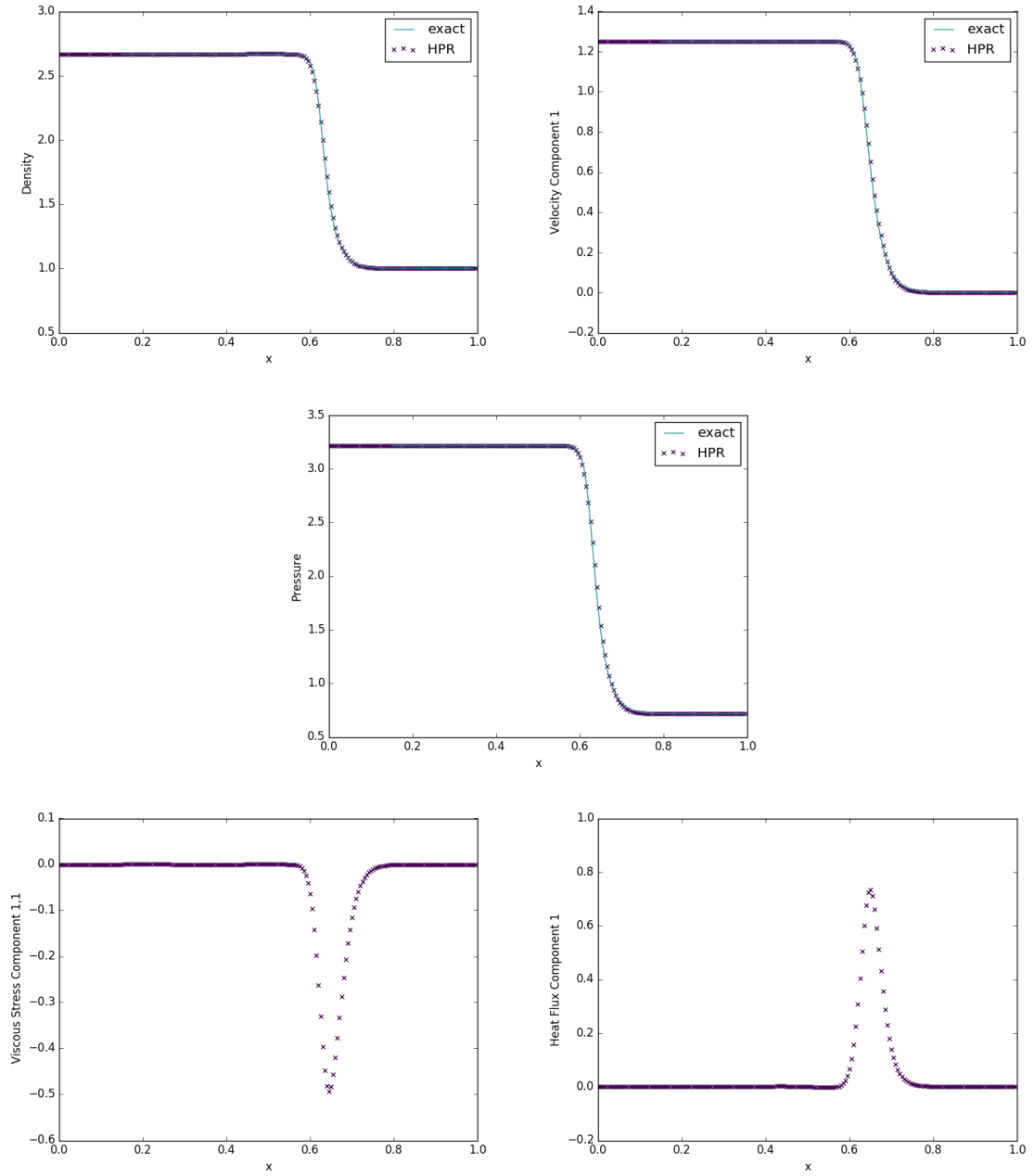
Figure 3.2: Density, velocity, pressure, viscous stress, and heat flux for the viscous shock test
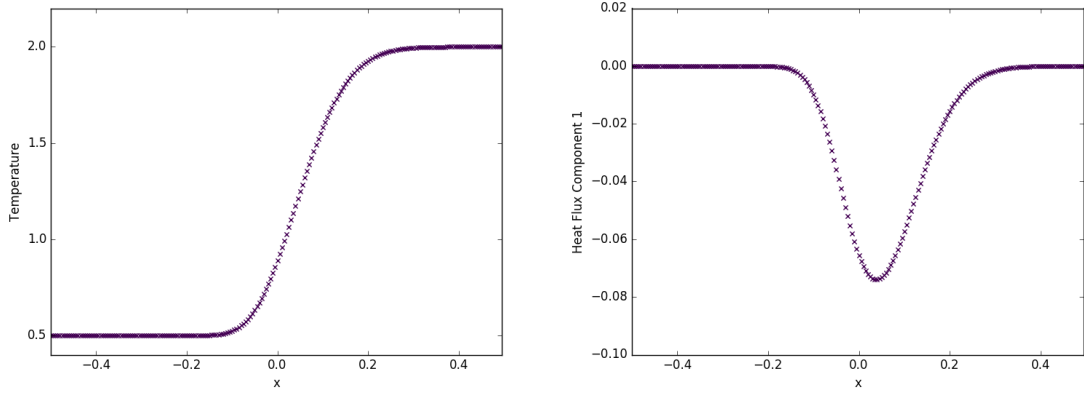
Figure 3.3: Temperature and heat flux for the heat conduction test
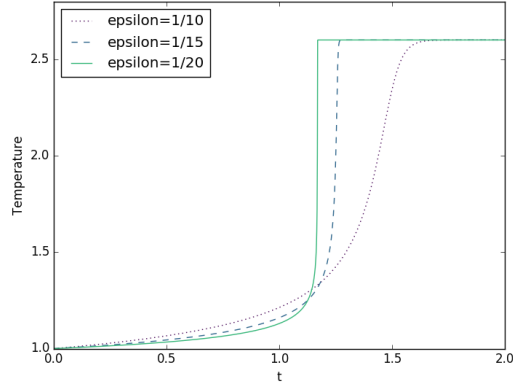
Figure 3.4: Temperature against time for Semenov's explosion test

The test was performed at $\epsilon = \frac{1}{10}, \frac{1}{15}, \frac{1}{20}$ with initial conditions $\rho = 1$, $p = 1$, $\boldsymbol{v} = \boldsymbol{0}$, $A = I_3$, $\boldsymbol{J} = \boldsymbol{0}$, $\lambda = 1$. Viscous effects and heat conduction were neglected. The material parameters were chosen to be $\gamma = 1.4$, $c_v = 2.5$, $\rho_0 = 1$, $T_0 = 1$, $Q_c = 4$. To match the scaling used by Sharpe and Short [104]:

$$B_c = \frac{c_v R_c}{E_a Q_c} \exp\left(\frac{E_a}{R_c}\right) \tag{3.7}$$

The results displayed in Figure 3.4 on page 35 should be compared with figure 1a in [104]. There is perfect agreement between the studies.

Chapter 4

Theoretical Results and Proposals

The results in this chapter are entirely novel. Section 4.1 presents a solution to a conjecture concerning general Discontinuous Galerkin systems. Section 4.2 presents the new method for simulating slow cookoff with the reactive HPR framework. Section 4.3 presents an eigenstructure analysis of the HPR model. The results in this section are used in Section 4.4, where the new method for simulating interfaces between different materials in the HPR framework is presented.

4.1   Eigenvalues of the DG System

Extending the DG method described in Section 2.2 to 3 dimensions, the following system must be solved for $\boldsymbol{q_\beta}$:

$$U_{\alpha\beta}\boldsymbol{q_\beta} = W_{\alpha\gamma}\boldsymbol{w_\gamma} - V_{\alpha\beta}^1\boldsymbol{F_1}\left(\boldsymbol{q_\beta}\right) - V_{\alpha\beta}^2\boldsymbol{F_2}\left(\boldsymbol{q_\beta}\right) - V_{\alpha\beta}^3\boldsymbol{F_3}\left(\boldsymbol{q_\beta}\right) \tag{4.1}$$
$$+ Z_{\alpha\beta}\left(\boldsymbol{S}\left(\boldsymbol{q_\beta}\right) - \boldsymbol{B}\left(\boldsymbol{q_\beta}\right)\cdot\nabla\theta_\gamma\left(\overrightarrow{\chi_\beta},\tau_\beta\right)\boldsymbol{q_\gamma}\right)$$

where now $\overrightarrow{\chi}$ represents the 3 scaled spatial variables χ_1,χ_2,χ_3.

$$V_{\alpha\beta}^i = \left\langle\theta_\alpha,\frac{\partial\theta_\beta}{\partial\chi_i}\right\rangle \tag{4.2a}$$

$$Z_{\alpha\beta} = \langle\theta_\alpha,\theta_\beta\rangle \tag{4.2b}$$

and either

$$U_{\alpha\beta} = \left\langle\theta_\alpha,\frac{\partial\theta_\beta}{\partial\tau}\right\rangle \tag{4.3a}$$

$$W_{\alpha\gamma} = 0 \tag{4.3b}$$

or, after integrating by parts in time:

$$U_{\alpha\beta} = [\theta_\alpha, \theta_\beta]^1 - \left\langle \frac{\partial \theta_\alpha}{\partial \tau}, \theta_\beta \right\rangle \tag{4.4a}$$

$$W_{\alpha\gamma} = [\theta_\alpha, \Psi_\gamma]^0 \tag{4.4b}$$

where $\Psi_\gamma (\chi_1, \chi_2, \chi_3)$ is an element of the following set, enumerated by γ:

$$\{\psi_a (\chi_1) \cdot \psi_b (\chi_2) \cdot \psi_c (\chi_3) : 0 \le a, b, c \le N\} \tag{4.5}$$

Taking the definition of N from Section 2.2, Dumbser [26] et al. remark that for the first definition of U, the eigenvalues of $U^{-1}V^i$ are all 0 for $0 \le N \le 5$, for $i = 1, 2, 3$. Dumbser and Olindo [34] state the same result for the second definition of U. This implies that in the conservative, homogeneous case ($\boldsymbol{B} = \boldsymbol{S} = \boldsymbol{0}$), owing to the Banach Fixed Point Theorem, existence and uniqueness of a solution are established, and convergence to this solution is guaranteed. As noted in [34], in the linear case it is implied that the iterative procedure converges after at most $N + 1$ iterations.

In [26] it is conjectured that the result concerning the eigenvalues of $U^{-1}V^i$ holds for any N, and any number of spatial dimensions. As of the time of writing, there doesn't appear to be a published solution to the conjecture. A solution is provided here.

First, given the orthogonal set of polynomials $\{\psi_0, \ldots, \psi_N\}^1$, define the following matrices:

$$\aleph_{ij} = \langle \psi_i, \psi_j \rangle \tag{4.6a}$$

$$\beth_{ij} = \left\langle \psi_i, \psi_j' \right\rangle \tag{4.6b}$$

WLOG, take the ordering $\alpha = \alpha_t (N + 1)^3 + \alpha_x (N + 1)^2 + \alpha_y (N + 1) + \alpha_z$ where $0 \le \alpha_t, \alpha_x, \alpha_y, \alpha_z \le N$. Using a similar ordering for β, according to the first definition of U:

$$U_{\alpha\beta} = \beth_{\alpha_t\beta_t} \cdot \aleph_{\alpha_x\beta_x} \cdot \aleph_{\alpha_y\beta_y} \cdot \aleph_{\alpha_z\beta_z} \tag{4.7a}$$

$$V_{\alpha\beta}^1 = \aleph_{\alpha_t\beta_t} \cdot \beth_{\alpha_x\beta_x} \cdot \aleph_{\alpha_y\beta_y} \cdot \aleph_{\alpha_z\beta_z} \tag{4.7b}$$

---

[1]Orthogonality is demonstrated by applying $N+1$-point Gaussian quadrature to $\langle \psi_i, \psi_j \rangle$ for each i, j (this quadrature is exact for polynomials of degree $\le 2N + 1$).

For the second definition:

$$U_{\alpha\beta} = \left(\psi_{\alpha_t}\left(1\right)\psi_{\beta_t}\left(1\right) - \beth_{\beta_t\alpha_t}\right) \cdot \aleph_{\alpha_x\beta_x} \cdot \aleph_{\alpha_y\beta_y} \cdot \aleph_{\alpha_z\beta_z} \tag{4.8}$$

Thus:

$$U = C \otimes \aleph \otimes \aleph \otimes \aleph \tag{4.9a}$$

$$V^1 = \aleph \otimes \beth \otimes \aleph \otimes \aleph \tag{4.9b}$$

where C is a matrix which varies between the two definitions of U. Thus:

$$U^{-1}V^1 = \left(C^{-1}\aleph\right) \otimes \left(\aleph^{-1}\beth\right) \otimes I \otimes I \tag{4.10}$$

Therefore:

$$\left(U^{-1}V^1\right)^k = \left(C^{-1}\aleph\right)^k \otimes \left(\aleph^{-1}\beth\right)^k \otimes I \otimes I \tag{4.11}$$

A matrix X is nilpotent ($X^k = 0$ for some $k \in \mathbb{N}$) if and only if all its eigenvalues are 0[2]. The conjecture will be proved if it is shown that $X = \aleph^{-1}\beth$ is nilpotent (as this would imply that $U^{-1}V^1$ is nilpotent). Note that:

$$X_{ij} = \frac{\left\langle \psi_i, \psi_j^{'} \right\rangle}{\left\langle \psi_i, \psi_i \right\rangle} \tag{4.12}$$

Taking $\boldsymbol{a} \in \mathbb{R}^{N+1}$, define:

$$p\left(x\right) = a_0\psi_0\left(x\right) + \ldots + a_N\psi_N\left(x\right) \in P_N \tag{4.13}$$

Note that:

$$\left(X\boldsymbol{a}\right)_i = a_0\frac{\left\langle \psi_i, \psi_0^{'} \right\rangle}{\left\langle \psi_i, \psi_i \right\rangle} + \ldots + a_N\frac{\left\langle \psi_i, \psi_N^{'} \right\rangle}{\left\langle \psi_i, \psi_i \right\rangle} = \frac{\left\langle \psi_i, p^{'} \right\rangle}{\left\langle \psi_i, \psi_i \right\rangle} \tag{4.14}$$

---

[2]For the theory in linear algebra required for this section, please consult a standard textbook on the subject, such as Nering [81].

As $\{\psi_0, \dots, \psi_N\}$ is an orthogonal basis for $P_N{}^3$:

$$p^{'}(x) = \frac{\left\langle \psi_0, p^{'} \right\rangle}{\left\langle \psi_0, \psi_0 \right\rangle} \psi_0 + \dots + \frac{\left\langle \psi_N, p^{'} \right\rangle}{\left\langle \psi_N, \psi_N \right\rangle} \psi_N \tag{4.15}$$

Applying X to the coefficients of $p^{'}$:

$$\left(X^2 \boldsymbol{a}\right)_i = \frac{\left\langle \psi_i, p^{''} \right\rangle}{\left\langle \psi_i, \psi_i \right\rangle} \tag{4.16}$$

By induction:

$$\left(X^k \boldsymbol{a}\right)_i = \frac{\left\langle \psi_i, p^{(k)} \right\rangle}{\left\langle \psi_i, \psi_i \right\rangle} \tag{4.17}$$

for any $k \in \mathbb{N}$. As $p \in P_N$, $X^{N+1}\boldsymbol{a} = \boldsymbol{0}$. As $\boldsymbol{a}$ was chosen arbitrarily, $X^{N+1} = 0$. Thus, $\beth^{-1}\aleph$ is nilpotent and the conjecture is solved. This proof is easily adapted to show that $U^{-1}V^2$ and $U^{-1}V^3$ are nilpotent, and clearly extends to any number of spatial dimensions.

4.2 Slow Cookoff on Short Bounded Domains

Take domain $x \in [0, L]$ with heating at the left boundary using either a fixed temperature or a fixed heat flux boundary condition, as described in Section 2.4. If the heating phase of the cookoff process (described in Section 1.1) takes time t^*, we require $L \ll c_0 \cdot t^*$. This requirement is explained in Section 7.1. The domain is initially occupied by a reactive fluid with concentration 1. The following technique accelerates the computation of the long heating phase.

Take the reactive thermal subsystem of the motionless reactive HPR model:

$$\frac{\partial \left(\rho J_i \right)}{\partial t} + \frac{\partial T}{\partial x_i} = -\frac{\rho H_i}{\theta_2 \left(\tau_2 \right)} \tag{4.18a}$$

$$\frac{\partial \left(\rho E \right)}{\partial t} + \frac{\partial q_k}{\partial x_k} = 0 \tag{4.18b}$$

$$\frac{\partial \left(\rho \lambda \right)}{\partial t} = -\rho \lambda K \left(T \right) \tag{4.18c}$$

---

[3]$\{\psi_0, \dots, \psi_N\}$ is a linearly independent set of size $\dim P_N$, and is thus a basis.

$$E = \frac{p + \gamma p_\infty}{(\gamma - 1)\rho} + \frac{\alpha^2}{2}\|\boldsymbol{J}\|^2 - Q_c(1 - \lambda) \tag{4.19}$$

In [31] it is shown that the heat characteristic of this system has speed:

$$c_h = \frac{\alpha}{\rho}\sqrt{\frac{T}{c_v}} \tag{4.20}$$

It is also demonstrated that around equilibrium ($\boldsymbol{v} = \boldsymbol{0}$, $A = I$, $\boldsymbol{J} = \boldsymbol{0}$), the largest eigenvalue of the full HPR system has the following magnitude:

$$\sqrt{\frac{C\rho + \sqrt{C^2 - 4\rho^2 c_h^2\left(p + \frac{4}{3}c_s^2\right)}}{2\rho}}, \quad C = c_0^2 + c_h^2 + \frac{4}{3}c_s^2 \tag{4.21}$$

For example, with the conditions $\rho = 1$, $p = 1$ and parameters $c_s = 1$, $\alpha = 1$, $c_v = 2.5$, $\gamma = 1.4$ (as featured in many of the numerical tests in [31]), the heat characteristic has speed $c_h = \sqrt{\frac{2}{5}} \approx 0.632$, and the largest eigenvalue of the full system is approximately 2.20. Thus, by the definition in Section 2.4, the time step used in an explicit solver for the reduced system will be around 3.5 times larger than that for the full system. In this study, it is proposed that in simulating slow cookoff, the thermal subsystem alone is solved (similarly to the method employed in [72]). Unlike in the cited paper, however, the full reactive HPR system will be employed when the rate of the chemical reaction becomes appreciable (which, of course, will be open to interpretation), to capture the full dynamics of the violent combustion.

The reduced system is still hyperbolic but is now also conservative (unlike the full system). The ADER-WENO solver is no longer necessary, and a less expensive operator splitting scheme can be used, as described in Section 2.5. The homogeneous subsystem is solved to first order, as higher-order accuracy is not needed here, owing to the smooth dynamics of the heating process.

The ODE subsystem is:

$$\frac{dJ_i}{dt} = -\frac{\alpha^2}{\theta_2(\tau_2)}J_i \tag{4.22a}$$

$$\frac{d\lambda}{dt} = -K(T)\lambda \tag{4.22b}$$

ρ is treated as constant in time in the reduced system and p does not evolve over the time step of the ODE subsystem, so T is constant over this period, giving the analytical solution:

$$J_i^{n+1} = \exp\left(-\frac{\alpha^2 \Delta t}{\theta_2\left(\tau_2\right)}\right) \tilde{J}_i^{n+1} \tag{4.23a}$$

$$\lambda^{n+1} = \exp\left(-K\left(\tilde{T}^{n+1}\right)\Delta t\right) \tilde{\lambda}^{n+1} \tag{4.23b}$$

The reduced system does not contain evolution terms for the density. It produces roughly the correct temperature profile, but ρ remains static, with pressure given by $p = (\gamma - 1) c_v T \rho - p_\infty$. On the timescale produced by the slow heating rate, the pressure in the full system in fact tends to equilibrate across the domain quickly. A process is required to calculate ρ, p correctly from T in the reduced system.

p is approximated as being spatially constant, and the velocity as $\mathbf{0}$. The velocity of the fluid in the heating phase is shown to have little effect on the combustive process in [73]. This is confirmed in Section 5.4, where the constant pressure assumption is also shown to work well. The average specific microscale energy in each cell is:

$$\overline{\rho E_1} = \frac{1}{n}\sum_i \rho_i \left(E_i - \frac{\alpha^2}{2}\|\boldsymbol{J_i}\|^2 + Q_c\left(1 - \lambda_i\right)\right) \tag{4.24}$$

Thus:

$$\bar{p} = (\gamma - 1)\overline{\rho E_1} - \gamma p_\infty \tag{4.25a}$$

$$\rho_i = \frac{\bar{p} + p_\infty}{(\gamma - 1) c_v T_i} \tag{4.25b}$$

Pressure and density are recalculated at every time step. This approximation is very computationally cheap, and works well under the circumstances investigated in Section 5.4. Not only is the time restriction based on the characteristic speeds of the system reduced, but the computational cost is reduced by solving a much smaller system.

In [31] it is shown that c_s can be derived experimentally from:

$$c_s = \sqrt{\frac{3}{4}\left(c_\infty^2 - c_0^2\right)} \tag{4.26}$$

Similarly, it is suggested that α is derived experimentally by measuring c_h. Thus, the factor gain in the time step as a result of this procedure depends on the properties of the material being modeled, and may be significantly better or worse than the example value given here. Even in the worst-case scenario where the characteristics of the heat waves travel faster than those of the longitudinal pressure waves (and so there is not improvement in the time step), the computational cost is still greatly reduced.

The procedure is named *the isobaric cookoff technique.*

4.3 Eigenstructure of the HPR Model

Eigenvalues

The primitive form of the HPR model is derived in Chapter B. Considering the primitive system matrices M_i given in Chapter C, it is clear that the eigenvalues of the HPR system in the first spatial axis consist of v_1 repeated 8 times, along with the roots of:

$$\begin{vmatrix} (v_1 - \lambda)\, I & \Xi_2 \\ \Xi_1 & (v_1 - \lambda)\, I \end{vmatrix} = 0 \tag{4.27}$$

where

$$\Xi_1 = \begin{pmatrix} -\frac{\sigma_{11}}{\rho^2} & \frac{1}{\rho} & -\frac{1}{\rho}\frac{\partial\sigma_{11}}{\partial A_{11}} & -\frac{1}{\rho}\frac{\partial\sigma_{11}}{\partial A_{21}} & -\frac{1}{\rho}\frac{\partial\sigma_{11}}{\partial A_{31}} \\ -\frac{\sigma_{21}}{\rho^2} & 0 & -\frac{1}{\rho}\frac{\partial\sigma_{21}}{\partial A_{11}} & -\frac{1}{\rho}\frac{\partial\sigma_{21}}{\partial A_{21}} & -\frac{1}{\rho}\frac{\partial\sigma_{21}}{\partial A_{31}} \\ -\frac{\sigma_{31}}{\rho^2} & 0 & -\frac{1}{\rho}\frac{\partial\sigma_{31}}{\partial A_{11}} & -\frac{1}{\rho}\frac{\partial\sigma_{31}}{\partial A_{21}} & -\frac{1}{\rho}\frac{\partial\sigma_{31}}{\partial A_{31}} \\ -\frac{T}{\rho^2} & \frac{T}{\rho(p+p_\infty)} & 0 & 0 & 0 \end{pmatrix} \tag{4.28}$$

$$\Xi_2 = \begin{pmatrix} \rho & 0 & 0 & 0 \\ \gamma p & 0 & 0 & (\gamma-1)\,\alpha^2 T \\ A_{11} & A_{12} & A_{13} & 0 \\ A_{21} & A_{22} & A_{23} & 0 \\ A_{31} & A_{32} & A_{33} & 0 \end{pmatrix} \tag{4.29}$$

By the properties of block matrices[4], the remaining eigenvalues are v_1 and the roots of $\left|(v_1 - \lambda)^2 I - \Xi_1 \Xi_2\right| = 0$. Thus, $\lambda_i = v_1 \pm \sqrt{\tilde{\lambda}_i}$ where the $\tilde{\lambda}_i$ are the eigenvalues of the following matrix:

$$\Xi = \Xi_1 \Xi_2 = \begin{pmatrix} \frac{\gamma p - \sigma_{11}}{\rho} + \Omega_{11}^1 & \Omega_{12}^1 & \Omega_{13}^1 & \frac{(\gamma-1)\alpha^2 T}{\rho} \\ \frac{-\sigma_{21}}{\rho} + \Omega_{21}^1 & \Omega_{22}^1 & \Omega_{23}^1 & 0 \\ \frac{-\sigma_{31}}{\rho} + \Omega_{31}^1 & \Omega_{32}^1 & \Omega_{33}^1 & 0 \\ \frac{((\gamma-1)p - p_\infty)T}{\rho(p+p_\infty)} & 0 & 0 & \frac{(\gamma-1)\alpha^2 T^2}{\rho(p+p_\infty)} \end{pmatrix} \tag{4.30}$$

where an analytic form for Ω is given in the next section. Similar results hold for the other two spatial directions. In general it is not possible to express the eigenvalues of Ξ in terms of the eigenvalues of its submatrices. Note, however, that if $\alpha = 0$ then one of the eigenvalues is 0 and the remaining eigenvalues can be found analytically, using the form given in the appendix of [31].

The Acoustic Tensor

The quantity Ω is named here the *acoustic tensor*, due to its similarity to the acoustic tensor described in [13]. Using (A.9):

$$\Omega_{ij}^d = -\frac{1}{\rho}\frac{\partial \sigma_{id}}{\partial A_{kd}} A_{kj} \tag{4.31}$$

$$= c_s^2 \left(\delta_{id} \left(A\,\text{dev}\,(G) \right)_{kd} + \left(A\,\text{dev}\,(G) \right)_{ki} + A_{ki}G_{dd} + A_{kd}G_{id} - \frac{2}{3}G_{id}A_{kd} \right) A_{kj}$$

$$= c_s^2 \left(\delta_{id} \left(G\,\text{dev}\,(G) \right)_{dj} + \left(G\,\text{dev}\,(G) \right)_{ij} + G_{ij}G_{dd} + \frac{1}{3}G_{dj}G_{id} \right)$$

Thus:

$$\Omega^d = c_s^2 \left(\Delta^d G\,\text{dev}\,(G) + G_{dd}G + \frac{1}{3}g^d \right) \tag{4.32a}$$

$$g^d = G_d G_d^T \tag{4.32b}$$

$$\Delta_{ij}^d = \delta_{ij} + \delta_{id}\delta_{jd} \tag{4.32c}$$

---

[4]If A is invertible, $\det\begin{pmatrix} A & B \\ C & D \end{pmatrix} = \det(A)\det\left(D - CA^{-1}B\right)$

Eigenvectors

By hyperbolicity of the system, Ξ can be expressed as:

$$\Xi = Q^{-1}D^2Q \tag{4.33}$$

where D is a diagonal matrix with positive diagonal entries. The eigenvectors corresponding to $\lambda_i = v_1 \pm \sqrt{\tilde{\lambda}_i}$ take the form $\begin{pmatrix} \boldsymbol{u_1} & \boldsymbol{0_6} & \boldsymbol{u_2} & \boldsymbol{0_2} \end{pmatrix}^T$ where $\boldsymbol{u_1} \in \mathbb{R}^5$, $\boldsymbol{u_2} \in \mathbb{R}^4$ satisfy:

$$\begin{pmatrix} v_1 I & \Xi_2 \\ \Xi_1 & v_1 I \end{pmatrix} \begin{pmatrix} \boldsymbol{u_1} \\ \boldsymbol{u_2} \end{pmatrix} = \left(v_1 \pm \sqrt{\tilde{\lambda}_i} \right) \begin{pmatrix} \boldsymbol{u_1} \\ \boldsymbol{u_2} \end{pmatrix} \tag{4.34}$$

Thus, $\Xi_2 \boldsymbol{u_2} = \pm\sqrt{\tilde{\lambda}_i}\boldsymbol{u_1}$ and $\Xi_1 \boldsymbol{u_1} = \pm\sqrt{\tilde{\lambda}_i}\boldsymbol{u_2}$. Combining these results, $\Xi\boldsymbol{u_2} = \tilde{\lambda}_i\boldsymbol{u_2}$. Thus, $\boldsymbol{u_2}$ is a right eigenvector of Ξ and, taking the form $Q^{-1}\boldsymbol{e_i}$ for some $i = 1 \dots 4$.

Let $\Pi_k^{ij} = \frac{\partial \sigma_{i1}}{\partial A_{jk}}$. Using the result just obtained, the four eigenvectors corresponding to eigenvalues of the form $v_1 + \sqrt{\tilde{\lambda}_i}$ are columns 1-4 of matrix R below. Those corresponding to eigenvalues of the form $v_1 - \sqrt{\tilde{\lambda}_i}$ are columns 5-8. By inspection, it can be verified that the remaining 9 eigenvectors (corresponding to eigenvalue v_1) are the remaining columns.

$$R = \frac{1}{2} \begin{pmatrix} \left(\Xi_2 \left(DQ\right)^{-1}\right)_{1,:} & \left(\Xi_2 \left(DQ\right)^{-1}\right)_{1,:} & c\rho & 0 & 0 & 0 \\ \left(\Xi_2 \left(DQ\right)^{-1}\right)_{2,:} & \left(\Xi_2 \left(DQ\right)^{-1}\right)_{2,:} & c\left(p+p_\infty\right) & 0 & 0 & 0 \\ \left(\Xi_2 \left(DQ\right)^{-1}\right)_{3:5,:} & \left(\Xi_2 \left(DQ\right)^{-1}\right)_{3:5,:} & c\Pi_1^{-1}b & -2\Pi_1^{-1}\Pi_2 & -2\Pi_1^{-1}\Pi_3 & 0 \\ 0 & 0 & 0 & 2I_3 & 0 & 0 \\ 0 & 0 & 0 & 0 & 2I_3 & 0 \\ Q^{-1} & -Q^{-1} & 0 & 0 & 0 & 0 \\ 0 & 0 & 0 & 0 & 0 & 2I_2 \end{pmatrix} \tag{4.35}$$

where

$$b = \begin{pmatrix} p + p_\infty - \sigma_{11} \\ -\sigma_{12} \\ -\sigma_{13} \end{pmatrix} \tag{4.36a}$$

$$c = \frac{2}{e_1^T \left(\Pi_1 A\right)^{-1} b - 1} \tag{4.36b}$$

A similar analysis yields the left eigenvectors as the rows of the following matrix:

$$L = \begin{pmatrix} (D^{-1}Q\Xi_1)_1 & (D^{-1}Q\Xi_1)_2 & (D^{-1}Q\Xi_1)_{3:5} & -\frac{1}{\rho}D^{-1}Q_{1:3}\Pi_2 & -\frac{1}{\rho}D^{-1}Q_{1:3}\Pi_3 & Q & 0 \\ (D^{-1}Q\Xi_1)_1 & (D^{-1}Q\Xi_1)_2 & (D^{-1}Q\Xi_1)_{3:5} & -\frac{1}{\rho}D^{-1}Q_{1:3}\Pi_2 & -\frac{1}{\rho}D^{-1}Q_{1:3}\Pi_3 & -Q & 0 \\ -\frac{1}{\rho} & 0 & e_1^T A^{-1} & e_1^T A^{-1}\Pi_1^{-1}\Pi_2 & e_1^T A^{-1}\Pi_1^{-1}\Pi_3 & 0 & 0 \\ 0 & 0 & 0 & I_3 & 0 & 0 & 0 \\ 0 & 0 & 0 & 0 & I_3 & 0 & 0 \\ 0 & 0 & 0 & 0 & 0 & 0 & I_2 \end{pmatrix} \tag{4.37}$$

In the form given here, $L = R^{-1}$.

4.4 An HPR Riemann Ghost Fluid Method

Barton et al. have presented an RGFM for the equations of non-linear elasticity [12, 14]. Owing to the similarity of the structure of the non-linear elasticity equations to those of the HPR model (differing only in the presence of source terms and the form of the shear stress tensor, and possibly the EOS), their method is built upon here. The resulting method is named *the HPR-RGFM*.

The Riemann Problem of the HPR model takes the form demonstrated in Figure 4.1 on page 46. Assuming all waves are distinct, there are four waves on either side of the contact discontinuity. On each side, one wave corresponds to the thermal impulse (manifesting as a heat wave) and the other three correspond to the distortion components in the axis in which the Riemann Problem is considered (manifesting as two shear waves and one longitudinal pressure wave). In the following the effect of the source terms on the solution to the RP is neglected. This is thought to be a reasonable assumption for the problem at hand, as only the star states are required, and the time
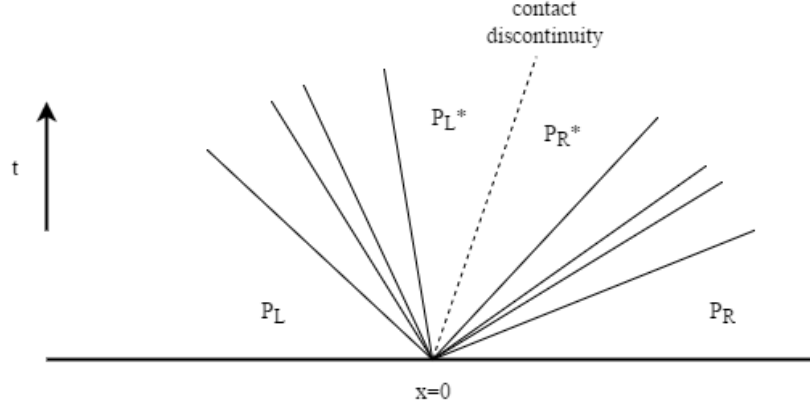
Figure 4.1: The Riemann Problem for the HPR model, assuming all waves are distinct

step over which the RP is taken is very small. The method is presented here along the first spatial axis. It can easily be adapted along any axis.

Denote the vector of primitive variables by $\boldsymbol{P}$. Take the set of left eigenvectors L (4.37) with eigenvalues $\{\lambda_i\}$. Neglecting the effect of the source terms produces the standard set of relations along characteristics (curves along which $\frac{dx}{dt} = \lambda_i$):[5]

$$L \cdot d\boldsymbol{P} = \boldsymbol{0} \tag{4.38}$$

$\boldsymbol{P_K^*}$ is now sought, where $K = L$ or $K = R$, denoting the left or right sides of the interface, respectively. Take the following linearisation:

$$d\boldsymbol{P} \approx \boldsymbol{P_K^*} - \boldsymbol{P_K} \tag{4.39}$$

13 relations from (4.38) are taken: four regarding the 4 sets of characteristics traveling into the contact discontinuity from side K (with speeds greater or less than v for $K = L$ or $K = R$, respectively), and nine relating to the contact discontinuity itself. This is

---

[5]Take the hyperbolic system $\frac{\partial \boldsymbol{P}}{\partial t} + M \frac{\partial \boldsymbol{P}}{\partial x} = \boldsymbol{S}$. Let $\boldsymbol{l_i}^T M = \lambda_i \boldsymbol{l_i}^T$. Along characteristics corresponding to λ_i:

$$\boldsymbol{l_i^T} \left(\frac{\partial \boldsymbol{P}}{\partial t} + M \frac{\partial \boldsymbol{P}}{\partial x} \right) = \boldsymbol{l_i^T} \left(\frac{\partial \boldsymbol{P}}{\partial t} + \frac{dx}{dt} \frac{\partial \boldsymbol{P}}{\partial x} \right)$$
$$= \boldsymbol{l_i^T} \frac{d\boldsymbol{P}}{dt} = \boldsymbol{l_i^T} \boldsymbol{S}$$
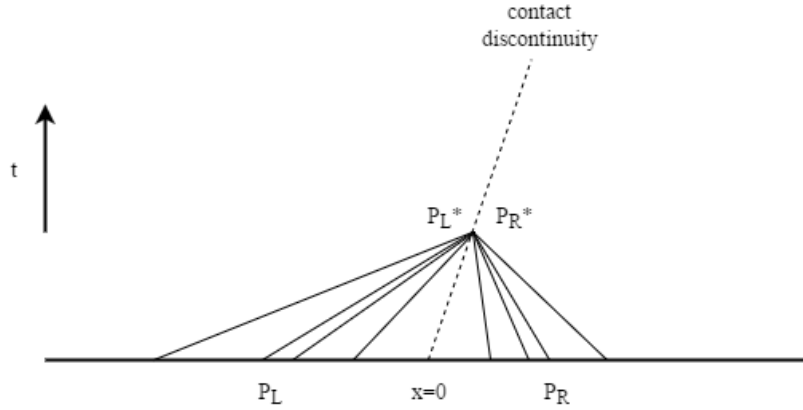
Figure 4.2: Different sets of characteristic curves, traveling from their respective initial points to the star region

demonstrated in Figure 4.2 on page 47. Four more relations must be derived to solve the system for $\boldsymbol{P_K^*}$. Expanding the Taylor series of $q_1^*, \boldsymbol{\sigma_1^*}$:

$$q_1^* = q_1 + \frac{\partial q_1}{\partial \rho} (\rho^* - \rho) + \frac{\partial q_1}{\partial p} (p^* - p) + \frac{\partial q_1}{\partial J_1} (J_1^* - J_1) + \cdots \tag{4.40a}$$

$$\boldsymbol{\sigma_1^*} = \boldsymbol{\sigma_1} + \frac{\partial \boldsymbol{\sigma_1}}{\partial \rho} (\rho^* - \rho) + \frac{\partial \boldsymbol{\sigma_1}}{\partial A_{mn}} (A_{mn}^* - A_{mn}) + \cdots \tag{4.40b}$$

Thus, using the results derived in Chapter A (which contains an analytic form for $\frac{\partial \sigma}{\partial A}$):

$$-\frac{q_1}{\rho} (\rho^* - \rho) + \frac{q_1}{p + p_\infty} (p^* - p) + \alpha^2 T (J_1^* - J_1) \approx q_1^* - q_1 \tag{4.41a}$$

$$\frac{\boldsymbol{\sigma_1}}{\rho} (\rho^* - \rho) + \frac{\partial \boldsymbol{\sigma_1}}{\partial A_{mn}} (A_{mn}^* - A_{mn}) \approx \boldsymbol{\sigma_1^*} - \boldsymbol{\sigma_1} \tag{4.41b}$$

These are the extra required relations. Thus:

$$\hat{L}_K \cdot \left(\boldsymbol{P_K^*} - \boldsymbol{P_K} \right) = \boldsymbol{c_K} \tag{4.42}$$

47

where $\hat{L}_K$ takes the following form, with $\xi = 1$ for $K = R$ and $\xi = -1$ for $K = L$:

$$
\begin{pmatrix}
-\frac{q_1}{\rho} & \frac{q_1}{p+p_\infty} & 0 & 0 & 0 & 0 & \alpha^2 T & 0 \\
\frac{\sigma_1}{\rho} & 0 & \Pi_1 & \Pi_2 & \Pi_3 & 0 & 0 & 0 \\
(D^{-1}Q\Xi_1)_1 & (D^{-1}Q\Xi_1)_2 & (D^{-1}Q\Xi_1)_{3:5} & -\frac{1}{\rho}D^{-1}Q_{1:3}\Pi_2 & -\frac{1}{\rho}D^{-1}Q_{1:3}\Pi_3 & \xi Q_{1:3} & \xi(Q)_4 & 0 \\
-\frac{1}{\rho} & 0 & e_1^T A^{-1} & e_1^T A^{-1}\Pi_1^{-1}\Pi_2 & e_1^T A^{-1}\Pi_1^{-1}\Pi_3 & 0 & 0 & 0 \\
0 & 0 & 0 & I_3 & 0 & 0 & 0 & 0 \\
0 & 0 & 0 & 0 & I_3 & 0 & 0 & 0 \\
0 & 0 & 0 & 0 & 0 & 0 & 0 & I_2
\end{pmatrix}
\tag{4.43}
$$

$$
c_K = \begin{pmatrix}
(q_1^*)_K - (q_1)_K \\
\left(\sigma_1^*\right)_K - (\sigma_1)_K \\
\mathbf{0}
\end{pmatrix}
\tag{4.44}
$$

$\hat{L}_K$ is evaluated at $\boldsymbol{P_K}$. It remains to find expressions for $\boldsymbol{\sigma_1^*}$ and q_1^* in terms of $\boldsymbol{P_L}, \boldsymbol{P_R}$ to close the system. The following boundary conditions are used:

$$
\left(\boldsymbol{\sigma_1^*}\right)_L = \left(\boldsymbol{\sigma_1^*}\right)_R
\tag{4.45a}
$$

$$
(q_1^*)_L = (q_1^*)_R
\tag{4.45b}
$$

$$
\boldsymbol{v_L^*} = \boldsymbol{v_R^*}
\tag{4.45c}
$$

$$
p_L^* = p_R^*
\tag{4.45d}
$$

Define $\hat{R} = \hat{L}^{-1}$. The last 8 columns of $\hat{R}$ are equal to the last 8 columns of R, given in Section 4.3. Although it is possible to find an analytic form of the remaining columns of $\hat{R}$ in terms of Ξ_1, Ξ_2 and their submatrices, it is highly inelegant and not particularly instructive, so it is not given here. In this study, when $\hat{R}$ was required, it was found numerically. Note that:

$$
\boldsymbol{P_K^*} = \boldsymbol{P_K} + \left(\hat{R}_K\right)_1 (q_1^* - q_1) + \left(\hat{R}_K\right)_{2:4} \left(\boldsymbol{\sigma_1^*} - \boldsymbol{\sigma_1}\right)
\tag{4.46}
$$

Thus:

$$p_K^* = p_K + \left(\hat{R}_K\right)_{2,1} (q_1^* - (q_1)_K) + \left(\hat{R}_K\right)_{2,2:4} \left(\boldsymbol{\sigma_1^*} - (\boldsymbol{\sigma_1})_K\right) \qquad (4.47\text{a})$$

$$\boldsymbol{v_K^*} = \boldsymbol{v_K} + \left(\hat{R}_K\right)_{12:14,1} (q_1^* - (q_1)_K) + \left(\hat{R}_K\right)_{12:14,2:4} \left(\boldsymbol{\sigma_1^*} - (\boldsymbol{\sigma_1})_K\right) \qquad (4.47\text{b})$$

Define:

$$\Theta_K = \begin{pmatrix} \left(\hat{R}_K\right)_{2,1} & \left(\hat{R}_K\right)_{2,2:4} \\ \left(\hat{R}_K\right)_{12:14,1} & \left(\hat{R}_K\right)_{12:14,2:4} \end{pmatrix} \qquad (4.48)$$

Thus, using the boundary conditions:

$$\begin{pmatrix} p^* \\ \boldsymbol{v^*} \end{pmatrix} = \begin{pmatrix} p_K \\ \boldsymbol{v_K} \end{pmatrix} + \Theta_K \left(\begin{pmatrix} q_1^* \\ \boldsymbol{\sigma_1^*} \end{pmatrix} - \begin{pmatrix} (q_1)_K \\ (\boldsymbol{\sigma_1})_K \end{pmatrix} \right) \qquad (4.49)$$

$$\therefore \begin{pmatrix} q_1^* \\ \boldsymbol{\sigma_1^*} \end{pmatrix} = (\Theta_L - \Theta_R)^{-1} \left(\begin{pmatrix} p_R \\ \boldsymbol{v_R} \end{pmatrix} - \begin{pmatrix} p_L \\ \boldsymbol{v_L} \end{pmatrix} + \Theta_L \begin{pmatrix} (q_1)_L \\ (\boldsymbol{\sigma_1})_L \end{pmatrix} - \Theta_R \begin{pmatrix} (q_1)_R \\ (\boldsymbol{\sigma_1})_R \end{pmatrix} \right)$$
$$(4.50)$$

Thus, $\boldsymbol{P_L^*}, \boldsymbol{P_R^*}$ are obtained with (4.42) and used in the RGFM, as described in Section 1.4.

It may be necessary to iterate this process a few times to ensure convergence to star states for which the boundary conditions hold. The convergence properties of this process are unknown, and there may be issues with stability and robustness. No significant issues were encountered in this study, however.

The Temperature Fix

In the original GFM, the entropy in the ghost region is fixed to the value of the interface cell in the real region (or, in the case of the isobaric fix, the second cell away from the interface). This was found to be inadequate in problems in which heat conduction across the material interface was desired, as the temperature in the ghost region then takes on an unrealistic value. Thus, when modeling problems involving intermaterial heat conduction with the HPR-RGFM, the density in the ghost region was fixed by a

temperature requirement, rather than an entropy requirement. If the temperatures of materials 1 and 2 were T_1, T_2 at the interface, the temperature in both of their ghost regions was set to $T^{ghost} = \frac{T_1+T_2}{2}$; a simple, intuitive choice to make.

$p^{ghost} = p^*$. Thus, when using a stiffened gas EOS, the ghost density for both fluids is:

$$\rho^{ghost} = \frac{p^* + p_\infty}{(\gamma - 1)\, c_v T^{ghost}} \tag{4.51}$$

Let $K = L$ or $K = R$. To ensure condition (1.20) is satisfied, the following transformation is required:

$$A_K^* \to \left(\frac{\rho^{ghost}}{\rho_K^*}\right)^{\frac{1}{3}} A_K^* \tag{4.52}$$

To ensure that $q_1^{ghost} = q_1^*$ after the temperature fix, the following transformation is required:

$$J_K^* \to \frac{T_K^*}{T^{ghost}} J_K^* \tag{4.53}$$

Chapter 5

Numerical Results: Cookoff

5.1 Viscous Shock-Induced Detonation

The HPR model is now combined with discrete ignition temperature reaction kinetics to model a ZND detonation wave[1] in a viscous, reactive, ideal gas. The test consists of a CJ wave with speed 1, traveling into a region of totally unburnt gas. The initial conditions are taken from Helzel et al. [51] and are given in Table 5.1 on page 51.

The material parameters are taken to be: $\gamma = 1.4$, $c_v = 2.5$, $\rho_0 = 1$, $p_0 = 1$, $c_s = 1$, $\alpha = 1$, $\mu = 10^{-4}$, $P_r = 0.75$, $Q_c = 1$, $K_0 = 250$, $T_i = 0.25$. The results for grids of 400 and 1600 cells at time $t = 0.5$ are found in Figure 5.1 on page 52. They are to be compared with those by Hidalgo and Dumbser [52]. The simulation with 400 cells corresponds well with that found in [52], and the simulation with 1600 cells is very close to Hidalgo's total variation diminishing reference solution calculated with 10,000 cells.

The von Neumann spike is well resolved, with the thin reaction zone behind it (corresponding to the region in which the concentration decreases from 1 to 0). The CJ state is maintained correctly behind the reaction zone. The spurious wave in the density is explained in [52] as being due to initialisation errors occurring as a result of using exact algebraic conditions for an ideal (infinitely thin) CJ detonation wave, which are solved with a viscous model with finite reaction rate.

	ρ	p	$\boldsymbol{v}$	A	$\boldsymbol{J}$	λ
$x < 0.25$	1.4	1	$\mathbf{0}$	$\sqrt[3]{1.4} \cdot I_3$	$\mathbf{0}$	0
$x \geq 0.25$	0.887565	0.191709	$(-0.577350, 0, 0)$	$\sqrt[3]{0.887565} \cdot I_3$	$\mathbf{0}$	1

Table 5.1: Initial conditions for the viscous shock-induced detonation test

---

[1]Zel'dovich [120], von Neumann [113], and Döring [24] independently proposed this detonation model, whereby reactive gas is compressed to high pressure by an infinitely thin shock wave into a *von Neumann spike*, initiating the reaction. The reaction zone is located behind the spike. In the reference frame of the shock, the gas moves supersonically ahead of the shock, subsonically in the reaction zone, and sonically in the region behind the reaction zone (which is described by the Chapman-Jouget state [17, 62]. The energy released in the reaction is transported acoustically to the shock to support it.
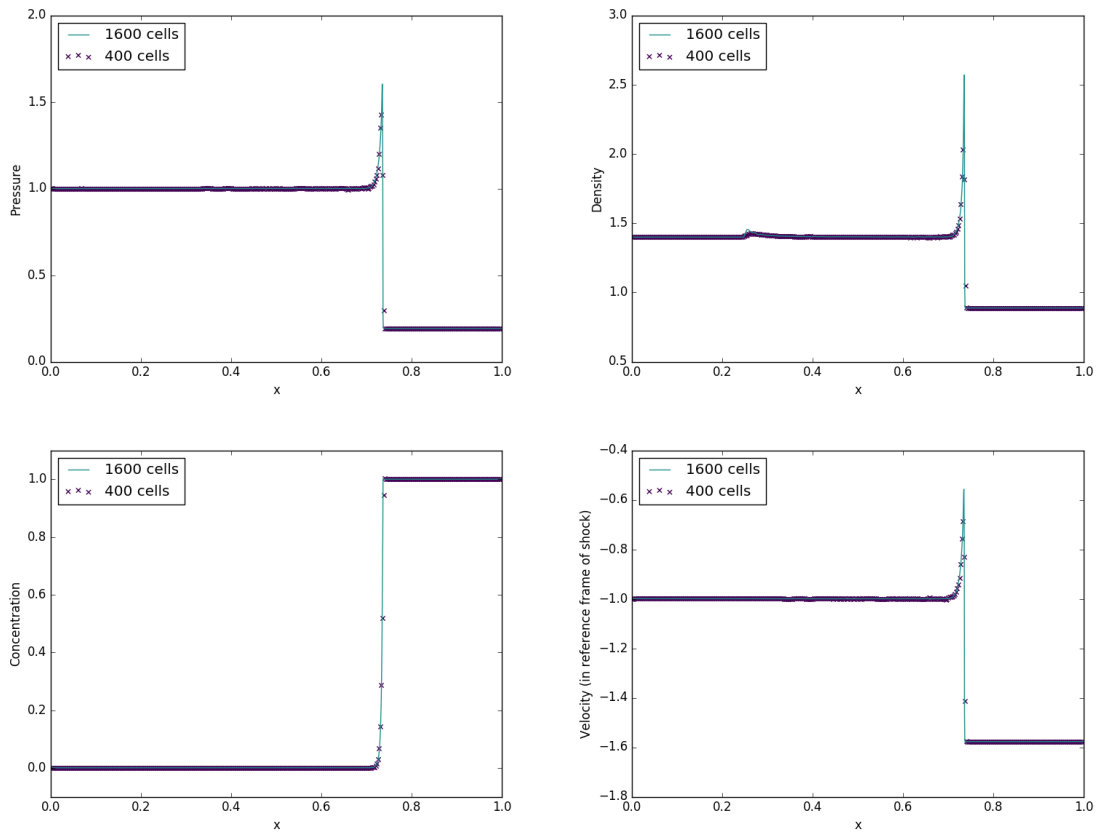
Figure 5.1: Pressure, density, concentration of reactant, and velocity (in the reference frame of the shock) in the viscous shock-induced detonation test

5.2   Heating-Induced Deflagration

As a step towards modeling the slow cooking off problem, the HPR model is now applied to the situation presented by Clarke, Kassoy and Riley [19–21]. Here, the domain $x \in [0, 8.5 \times 10^{-6}]$ is occupied by an ideal gas with initial conditions $\rho = \rho_0 = 1.176$, $p = p_0 = 101325$, $\boldsymbol{v} = \boldsymbol{0}$, $A = I_3$, $\boldsymbol{J} = \boldsymbol{0}$ and material parameters $\gamma = 1.4$, $c_v = 718$, $c_s = 55$, $\alpha = 500$, $\mu = 1.98 \times 10^{-5}$, $P_r = 0.72$. These values are chosen to be similar to air at room temperature.

Thermal energy is added at the left boundary at a high power of $\frac{\gamma p_0 c_0}{P_r(\gamma - 1)}$ (around $1.7 \times 10^8 W m^{-2}$). The test is performed with both a combustible and an inert gas. In the former case, the initial concentration is set to $\lambda = 1$. Arrhenius reaction kinetics are used, with $Q_c = 6\gamma c_v T_0$, $B_c = 7 \times 10^{10}$, $\epsilon = \frac{1}{20}$. The subsequent evolutions of the systems for 400 cells are shown in Figure 5.2 on page 54. Nondimensionalised time and length variables t^*, x^* are used, as in [20]:

$$t = \frac{\mu}{p_0 \gamma} t^* \tag{5.1a}$$

$$x = \frac{\mu c_0}{p_0 \gamma} x^* \tag{5.1b}$$

There are no analogues for α and c_s in the models used by Clarke et al. c_s is given the experimentally-derived value for CH_3Cl at 30°C given in [31]. α is chosen by trial and error so that the HPR results corresponded with those in [20]. The results presented here are thus close, but not identical to those of Clarke et al.

Note that heating the inert gas produces an acoustic wave of constant pressure, propagating ahead of the temperature curve. This pressure wave is also present in the heating of the combustible gas, where it proceeds in front of the combustion wave. The temperature increase accompanying this acoustic wave is not enough to ignite the reactive gas, and the thin reaction zone lags behind the acoustic wavefront. Although the combustion wave is referred to as a detonation wave in [20], it would now commonly be called a deflagration wave, as it travels subsonically and is not coincident with the shock wave. This phenomenon of a second, faster shock overtaking the combustion wave demonstrated experimentally by Kapila et al. [63], with a full mathematical analysis provided by Short [105], where it is shown to result from the steep temperature gradient at the time of ignition.
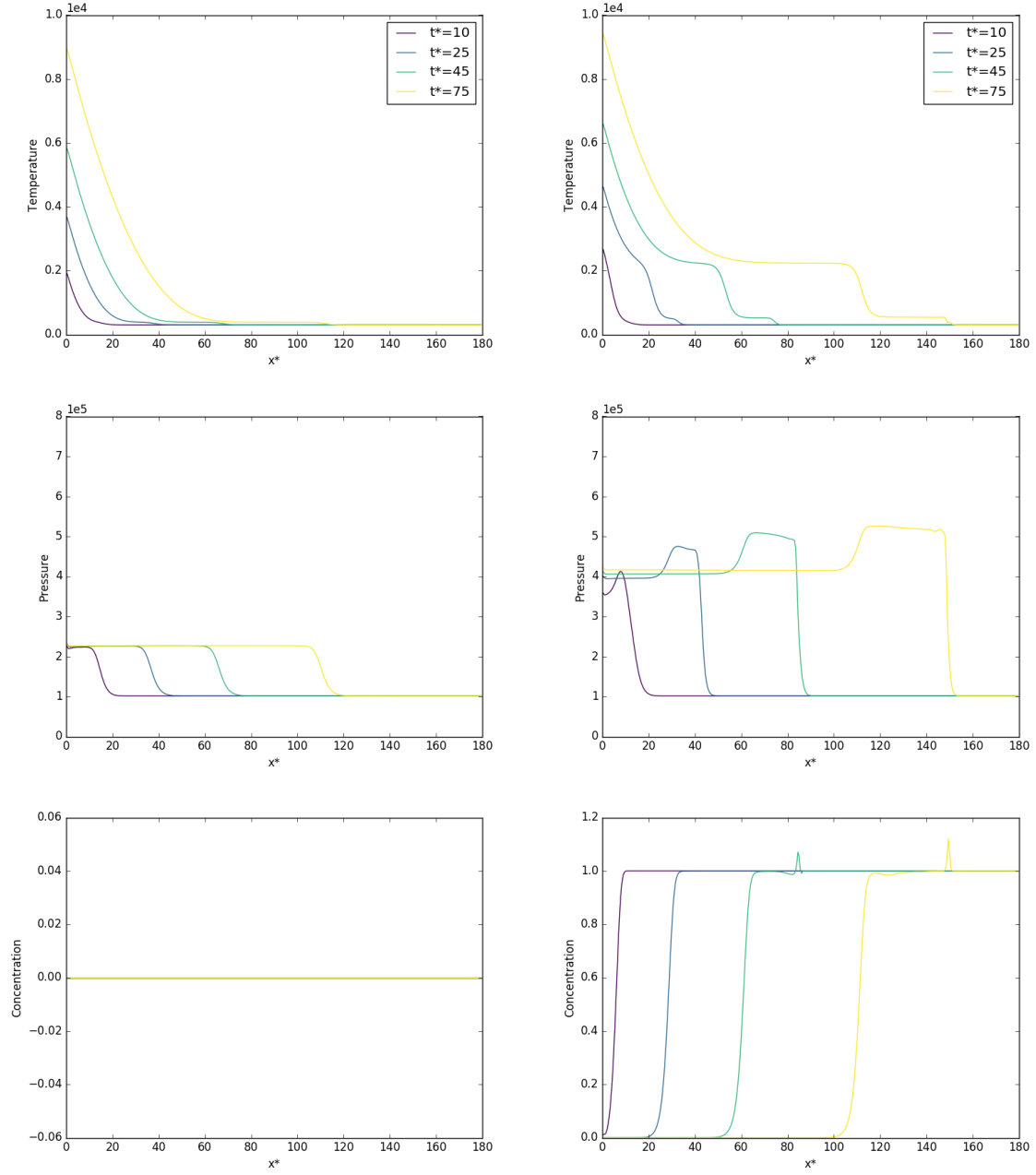
Figure 5.2: Temperature, pressure, and concentration of reactant in the heating-induced deflagration test with inert gas (left) / reactive gas (right)

5.3   Heating-Induced Detonation

It is now demonstrated that the heating-induced deflagration test can result in detonation if the temperature gradient upon ignition is less steep. This test is identical to the previous test, with one exception: ϵ is given the higher value of $\frac{1}{15}$. Thus, the activation energy is effectively lower, or equivalently, the whole gas volume is relatively closer to the ignition temperature when the gas at the left boundary ignites. The results of this test are shown in Figure 5.3 on page 56.

The von Neumann spike is present and well resolved, with a thin reaction zone appearing behind it in the concentration plot. Unlike in Section 5.1, the system does not relax to the CJ state behind the detonation wave, as thermal energy is continually added to the reflective left boundary. The region behind the reaction zone is thus complex.

5.4   Slow Cookoff

The performance of the isobaric cookoff technique presented in Section 4.2 will now be investigated. The initial conditions for a combustible gas are taken from Section 5.2. There is a time-dependent fixed-temperature boundary condition on the left, as described in Section 2.4, and the right boundary is reflective. The temperature at the left boundary is given by $T = T_0 \left(1 + t \cdot 10^6\right)$. Thus, this test can still be considered a quick cookoff in most contexts, but the heating process is four orders of magnitude slower than in the previous two tests; slow enough to demonstrate the isobaric cookoff technique.

Unlike in Section 5.2, as the heating rate is relatively low, the temperature gradient is fairly shallow at ignition, resulting in detonation rather than deflagration. The detonation wave reaches the end of the domain at about $t = 8.6 \times 10^{-7}$, with the long heating phase taking up most of this time. The detonation wave forms at around 8.5×10^{-7}. When using the isobaric cookoff technique, the full system is only calculated from around $t = 7 \times 10^{-7}$ onward.

The heating phase is shown in Figure 5.4 on page 58 at 9 equispaced points in time. The temperature profiles between the reduced and full system are very close. The
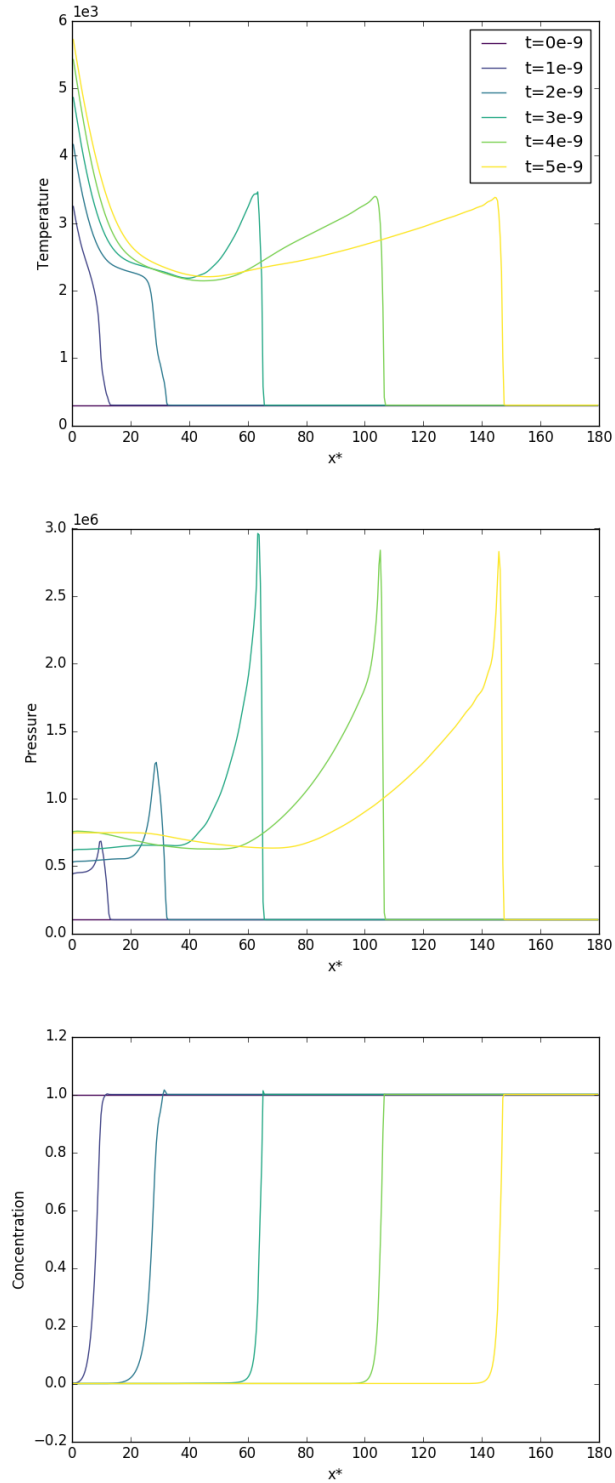
Figure 5.3: Temperature, pressure, and concentration of reactant in the heating-induced detonation test

constant pressure assumption works very well, as the heating rate is slow enough for the pressure differences it generates to equilibrate, and the domain is short enough that any acoustic waves emitted from the left boundary rebound into the domain. The pressure at each time step is slightly higher in the full system than the reduced system. This is due to the non-zero fluid velocities present in the full system (but not the reduced system) carrying heated material away from the left boundary, meaning that slightly more energy enters this system, as the boundary is held at a fixed, time-dependent value.

The zero velocities of the reduced system do not affect the shape of the final detonation wave, as the velocities in the full system are relatively small, but the indirect effect of this discrepancy on the total energy of the system means that the reduced system detonates about $6.55 \times 10^{-9}s$ later than the full system[2]. The subsequent evolution of the systems are almost indistinguishable (see Figure 5.5 on page 59). Proposals to rectify the discrepancy in the total energies of the systems are discussed in Section 7.1.

During the heating phase, the average time step for the reduced system was $\Delta t = 5.758 \times 10^{-11}$, as opposed to $\Delta t = 4.447 \times 10^{-11}$ for the full system. This relatively small difference is attributed to the fact that the heat characteristics are relatively fast with the values of the material parameters used (chosen to match those used in the heating-induced deflagration test). However, the WENO, DG, and FV steps took on average 0.0703s, 0.8355s, and 0.9326s respectively per iteration of the full system. The operator splitting solver took on average 0.0001522s per iteration of the reduced system (a speed-up of over 4 orders of magnitude). In both cases, the auxiliary functions (such as those applying the boundary conditions) took on average 0.01547s per iteration[3]. Thus, the heating phase took a total of 25740s with the full system, and 168s with the reduced system (a roughly 150-fold speed-up). Of course, these results are very implementation- and hardware-specific, and alternative implementations, running on different platforms may yield very different results. This is discussed further in Section 7.1.

---

[2]Detonation is defined here as the point at which 2.5% of reactant in any cell has burned; a fairly arbitrary measure, to be discussed in Section 7.1.

[3]All times quoted here resulted from running a single-threaded implementation of the solver on an Intel Core i7 4910-MQ.
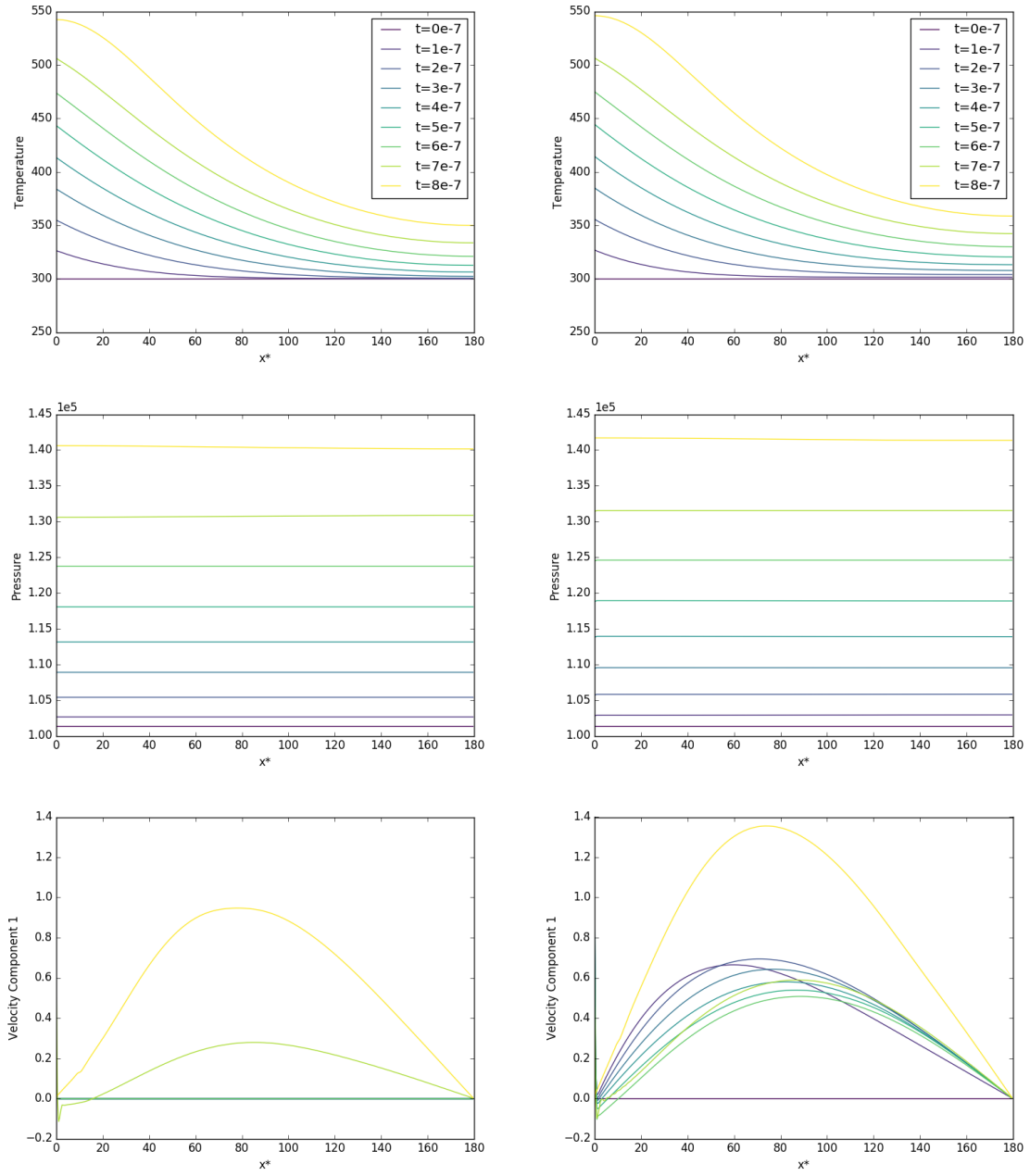
Figure 5.4: Temperature, pressure, and velocity in the heating phase of the slow cookoff test for the reduced system (left) / full system (right)
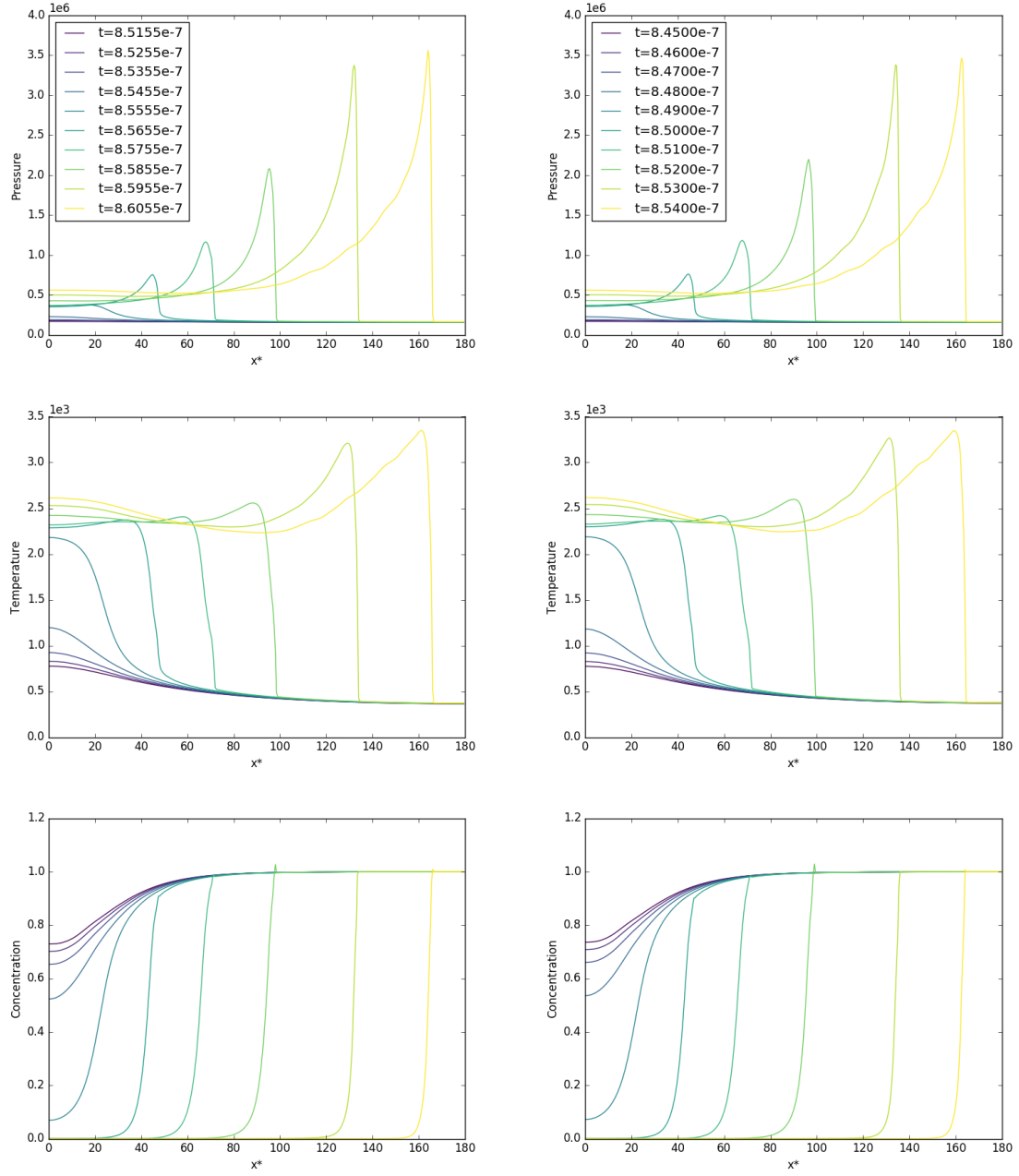
Figure 5.5: Pressure, temperature, and concentration of reactant in the detonation phase of the slow cookoff test for the reduced system (left) / full system (right)

Chapter 6

Numerical Results: Multimaterial Systems

The HPR-RGFM is now assessed. The first three tests in this chapter are standard Riemann problems, exact solutions to which exist for the Euler equations. The viscosity of the HPR model smears the solutions in areas in which the solutions to the Euler equations are discontinuous or not smooth. This smearing is not the result of using a low-order solver (all results in these sections being calculated to third order). The last two tests assess the ability of the HPR-RGFM to correctly model heat conduction across interfaces, using the temperature fix described in Section 4.4.

6.1 Viscous Sod Shock Tube

The purpose of this test is to ensure that the HPR-RGFM can maintain a sharp contact discontinuity in the famous shock tube test of Sod [106]. A viscous ideal gas is used with $\gamma = 1.4$, $\mu = 5 \times 10^{-4}$, $P_r = 2/3$, as in Ren et al. [89]. $c_v = 2.5$, $\rho_0 = 1$, $p_0 = 1$, $c_s = 1$, and $\alpha = 1$. The initial conditions are given in Table 6.1 on page 61. The final time is $t = 0.2$ and all simulations used 200 cells.

The results in Figure 6.1 on page 61 without the HPR-RGFM match those in [89] well. The viscous smearing in the density and the "bump" in the velocity at the contact discontinuity are present, as investigated by Jameson [58]. When applying the HPR-RGFM, the contact discontinuity is now maintained, as it should be, as the gases are assumed to be immiscible. Additionally, the bump in the velocity is no longer present. This is correct, as the bump corresponds to a smearing of the density across the contact discontinuity, which should not occur for immiscible gases.

6.2 Water-Water Interface

This problem tests the HPR-RGFM for the stiffened EOS. The test comprises two volumes of water with different pressures, meeting at $x = 0.5$ (as found in Ghaisas

	ρ	p	$\boldsymbol{v}$	A	$\boldsymbol{J}$
$x < 0.5$	1	1	$\boldsymbol{0}$	I_3	$\boldsymbol{0}$
$x \geq 0.5$	0.125	0.1	$\boldsymbol{0}$	$0.5 \cdot I_3$	$\boldsymbol{0}$

Table 6.1: Initial conditions for the viscous Sod shock tube test
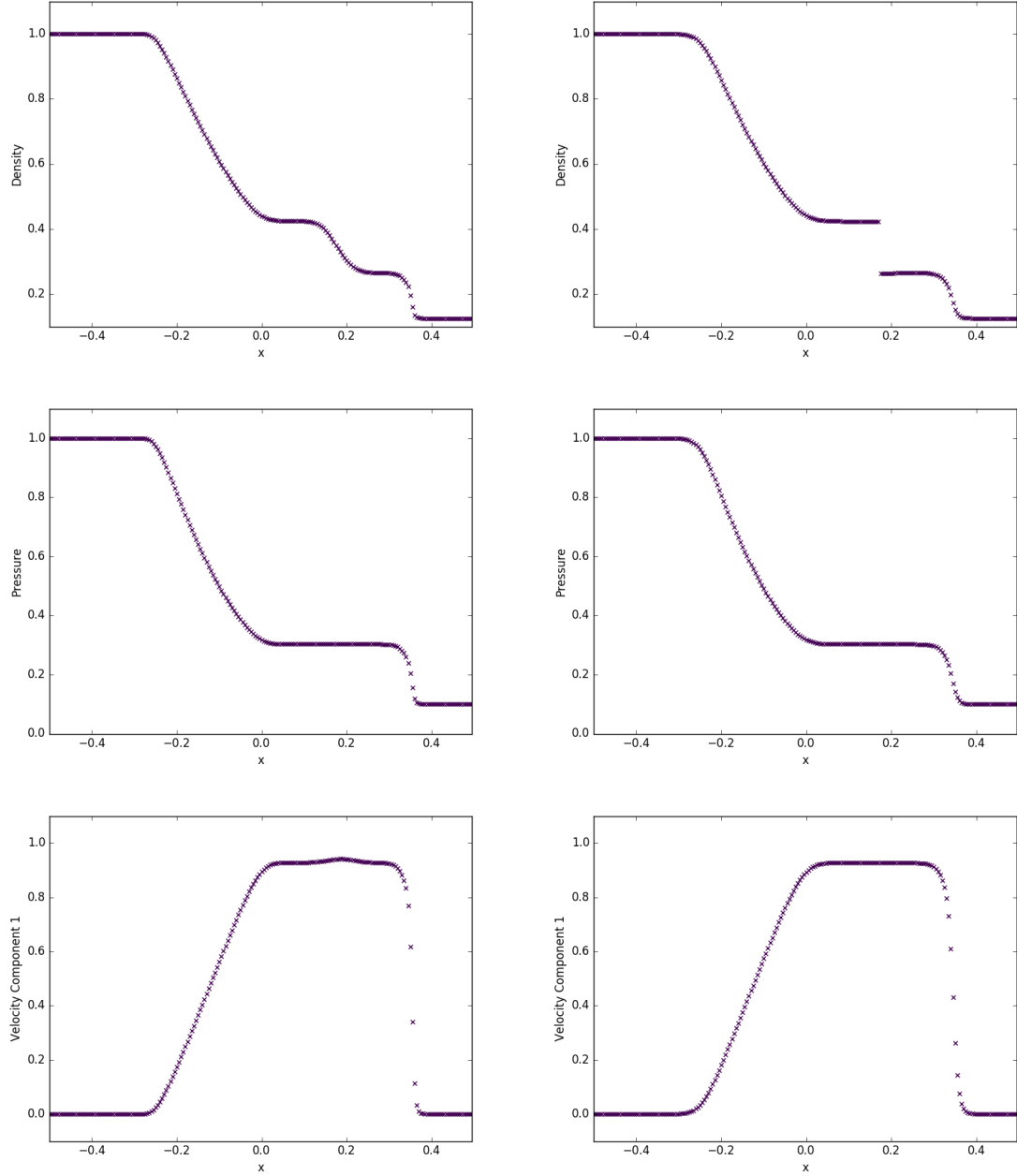
Figure 6.1: Density, pressure, and velocity for the viscous Sod shock tube test with viscosity $\mu = 5 \times 10^{-4}$ without HPR-RGFM (left) / with HPR-RGFM (right)

61

	ρ	p	$\boldsymbol{v}$	A	$\boldsymbol{J}$
$x < 0.5$	1000	7×10^8	$\mathbf{0}$	I_3	$\mathbf{0}$
$x \geq 0.5$	1000	10^8	$\mathbf{0}$	I_3	$\mathbf{0}$

Table 6.2: Initial conditions for the water-water interface test

et al. [42], Test III.B.2). The initial conditions are found in Table 6.2 on page 62. Realistic values are chosen for the material parameters: $\gamma = 4.4$, $p_\infty = 6 \times 10^8$, $c_v = 950$, $\mu = 10^{-3}$, $P_r = 7$, $\rho_0 = 1000$, $T_0 = 300$. c_s and α are taken to be 55 and 500, respectively. The final time is $t = 1.5 \times 10^{-4}$ and all simulations used 200 cells.

The results in Figure 6.2 on page 63 without the HPR-RGFM match those in [42] well. The sharp contact discontinuity is preserved by the HPR-RGFM.

6.3   Helium Bubble

The interface between two different gases is now modeled. As in Test B of Wang et al. [114], a bubble of helium - surrounded by air - initially occupies the region $x \in [0.4, 0.6]$. A shock front in the air, initially at $x = 0.05$, travels towards the helium bubble. The initial conditions are given in Table 6.3 on page 65. Realistic material parameters are taken for the helium: $\gamma = 1.66$, $c_v = 3127$, $\rho_0 = 0.163$, $\mu = 1.99 \times 10^{-5}$, $P_r = 0.688$, and for the air: $\gamma = 1.4$, $c_v = 721$, $\rho_0 = 1.18$, $\mu = 1.85 \times 10^{-5}$, $P_r = 0.714$. In both cases, $p_0 = 101325$, $c_s = 55$, and $\alpha = 500$.

200 cells are used. The results for times $t = 7 \times 10^{-4}$ and $t = 14 \times 10^{-4}$ are displayed in Figure 6.3 on page 64. In the former, the shock is about to hit the helium bubble (corresponding to the region of low density). In the latter, the shock has traveled through the helium bubble, compressing it slightly, and the bubble itself has moved almost 0.1 spatial units to the right. There is good correspondence with the results in [114] and the sharp discontinuity in density is maintained.

6.4   Intermaterial Heating-Induced Acoustic Wave

This test assesses the ability of the HPR-RGFM to conduct heat between two different materials. Take the material parameters for air from Section 5.2, and the material
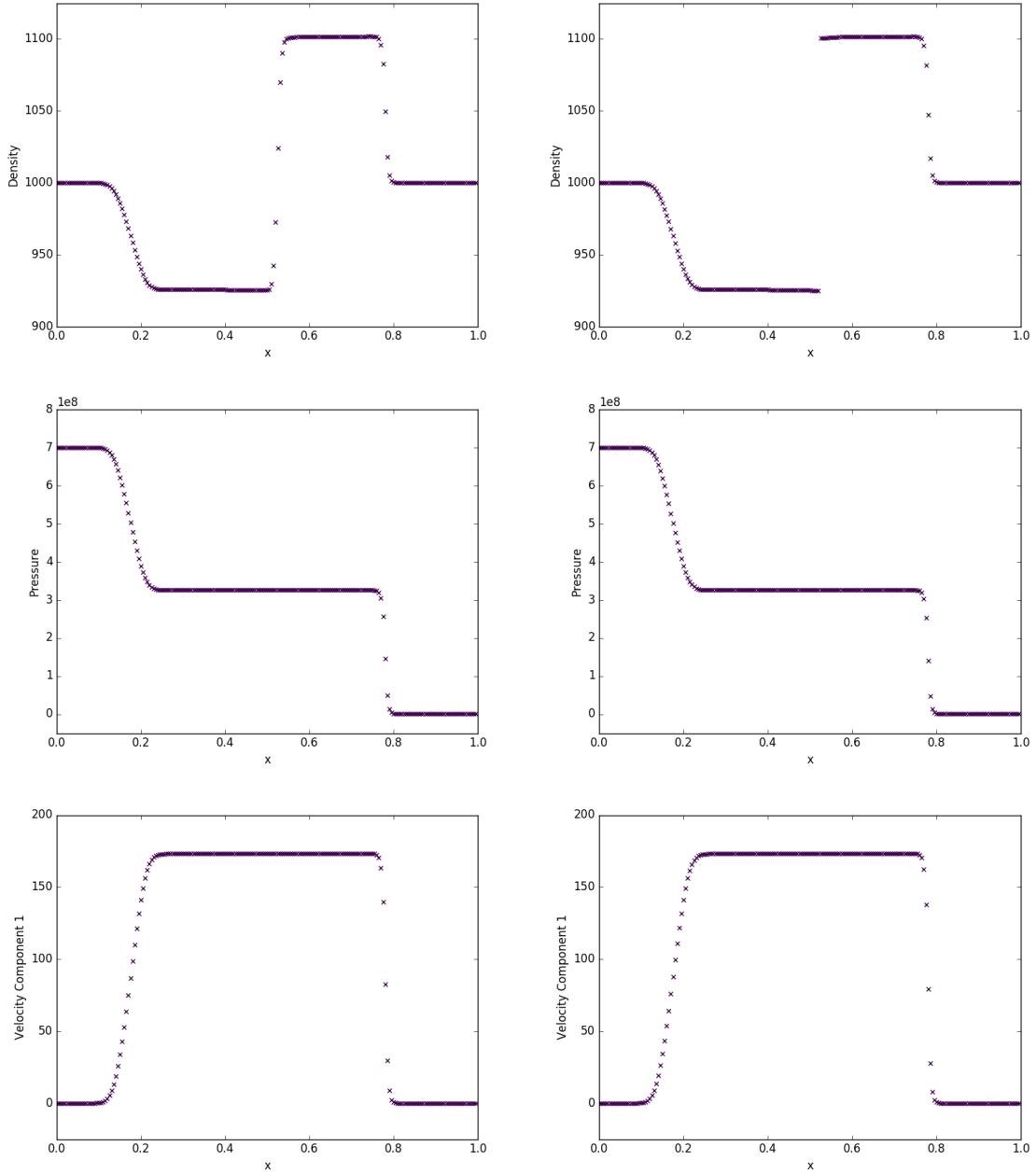
Figure 6.2: Density, pressure, and velocity for the water-water interface test without HPR-RGFM (left) / with HPR-RGFM (right)
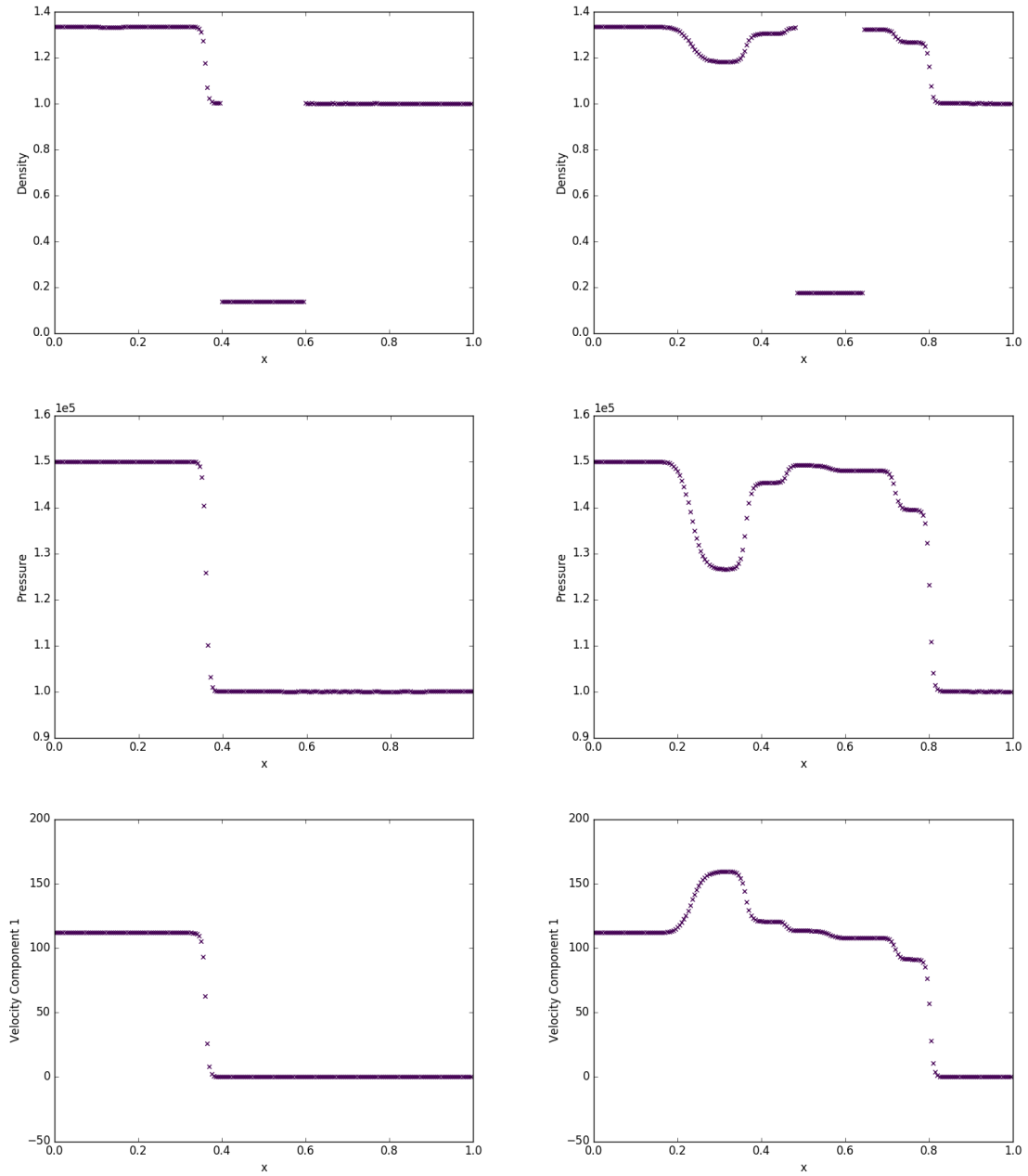
Figure 6.3: Density, pressure, and velocity for the helium bubble test with HPR-RGFM at times $t = 7 \times 10^{-4}$ (left) and $t = 14 \times 10^{-4}$ (right)

	ρ	p	$\boldsymbol{v}$	A	$\boldsymbol{J}$
$x < 0.05$	1.3333	1.5×10^5	$\left(35.35\sqrt{10}\ 0\ 0 \right)$	$\left(\frac{1.3333}{1.18} \right)^{\frac{1}{3}} I_3$	$\boldsymbol{0}$
$0.05 \leq x < 0.4$	1	10^5	$\boldsymbol{0}$	$\left(\frac{1}{1.18} \right)^{\frac{1}{3}} I_3$	$\boldsymbol{0}$
$0.4 \leq x < 0.6$	0.1379	10^5	$\boldsymbol{0}$	$\left(\frac{0.1379}{0.163} \right)^{\frac{1}{3}} I_3$	$\boldsymbol{0}$
$0.6 \leq x \leq 1$	1	10^5	$\boldsymbol{0}$	$\left(\frac{1}{1.18} \right)^{\frac{1}{3}} I_3$	$\boldsymbol{0}$

Table 6.3: Initial conditions for the helium bubble test

	ρ	p	$\boldsymbol{v}$	A	$\boldsymbol{J}$
air	1.18	101325	$\boldsymbol{0}$	I_3	$\boldsymbol{0}$
helium	0.164	101325	$\boldsymbol{0}$	I_3	$\boldsymbol{0}$

Table 6.4: Initial conditions for the intermaterial heating-induced acoustic wave test

parameters for helium from Section 6.3. Taking the scaled spatial variable x^* from Section 5.2, the domain $x^* \in [0, 90]$ is used, with the same boundary conditions (high-power heating on the left boundary). Three scenarios are tested:

1. The domain is filled with air.

2. The domain comprises two volumes of air, initially separated at $x^* = 22.5$.

3. The domain comprises a volume of air (left) and a volume of helium (right), initially separated at $x^* = 22.5$.

The initial conditions for the two gases in all scenarios are given in Table 6.4 on page 65. The results of the test are shown in Figure 6.4 on page 67 and Figure 6.5 on page 68 for various times. The material interface is represented by a dashed vertical line in scenarios 2 and 3. All simulations used 400 cells.

As the left wall heats up, a temperature gradient develops and the acoustic wave described in Section 5.2 appears. The results for scenarios 1 and 2 are indistinguishable, as they should be, and there are no aberrations around the material interface in scenario 2. In scenario 3, the acoustic wave hits the interface at around $t = 2 \times 10^{-9}$ and then speeds up (as it should, the speed of sound in helium being around three times that of air). The heat flux wave increases in intensity after passing into the helium,

Time ($\times 10^{-9}$)	0	1	2	3	4	5
Mass in Scenario 2 ($\times 10^{-6}$)	1.254	1.255	1.253	1.252	1.252	1.253
Mass in Scenario 3 ($\times 10^{-6}$)	1.254	1.253	1.248	1.254	1.255	1.255

Table 6.5: Mass of the air volume in scenarios 2 and 3 at various times

owing to the fact that the wave is traveling faster. As expected, all variables displayed are continuous across the interface.

In scenarios 2 and 3 the interface moves to the right as the air heats up and expands. The masses of the air volumes in these two scenarios at various times are given in Table 6.5 on page 66, demonstrating that mass is conserved well as the interface moves.

6.5   Intermaterial Heat Conduction

Returning to the heat conduction test of Section 3.3, an interface is now initially placed between the two volumes of air at $x = 0.5$. The final time is again taken to be $t = 1$, and 200 cells are used. Results are displayed in Figure 6.6 on page 69, using the results from Section 3.3 as a reference. The material interface is denoted by a dashed vertical line.

The temperature curve generated using the HPR-RGFM matches very well the reference solution. The interface has moved to $x = 0.53756$, as is to be expected, as the cooler gas on the left expands as it heats up, and the hotter gas on the right contracts as it cools. Initially, the mass of the left volume is 1 and the right volume is 0.25. At $t = 1$, these masses are 0.9997 and 0.2503, respectively. Thus, mass on either side is conserved to a good approximation. Although the HPR-RGFM results for the heat flux match the reference solution well over most of the domain, there are aberrations in a small region around the interface. Although this doesn't affect the temperature curve, these discrepancies are undesirable, and possible methods to rectify them are discussed in Section 7.2.

The temperature fix is crucial in obtaining these results. Using the traditional entropy fix instead results in a stationary system, with the initial conditions persisting indefinitely. This is because the entropy fix does not allow the system to "see" the temperature difference, meaning that no heat flux is generated across the interface.

66
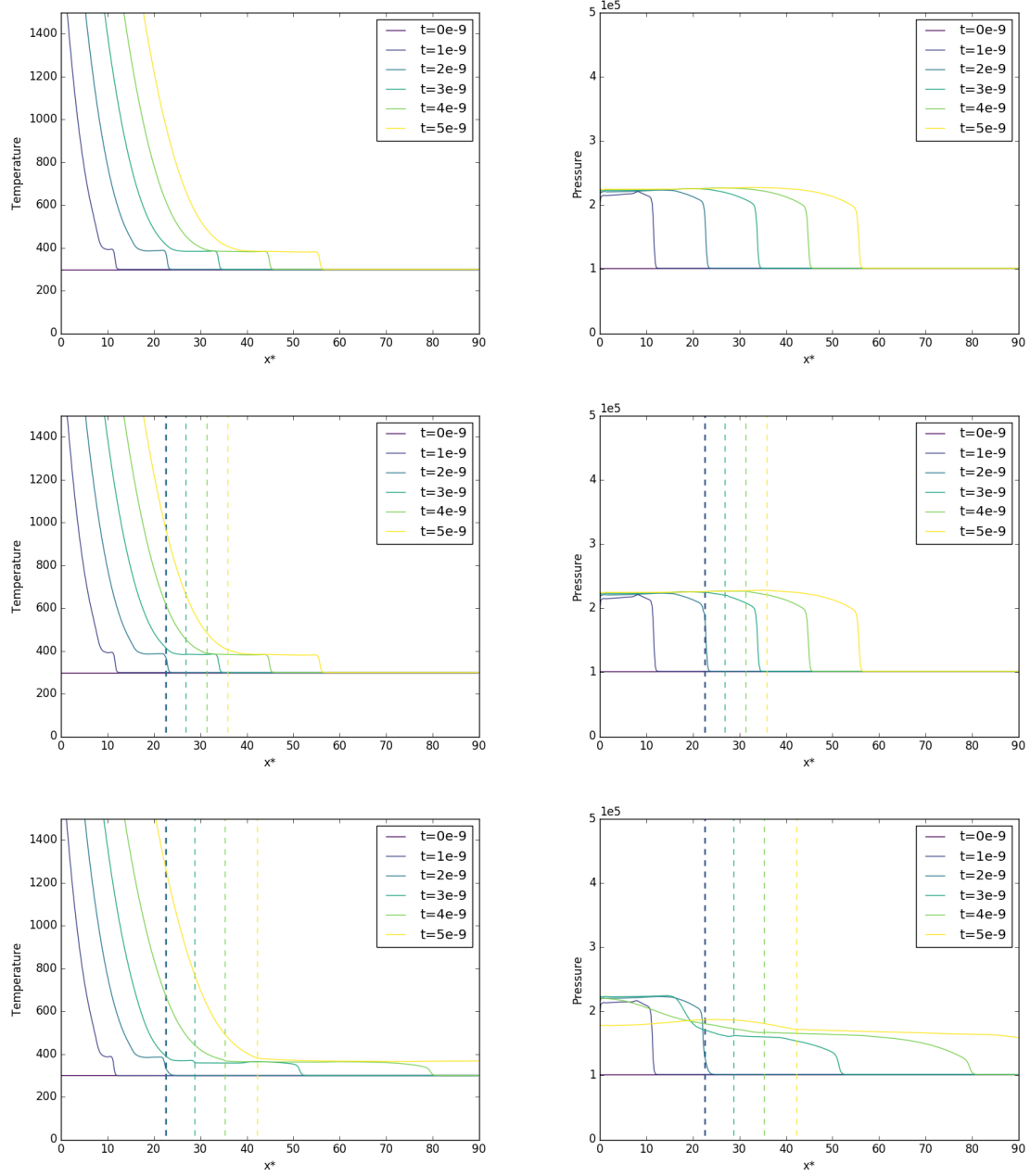
Figure 6.4: Temperature and pressure for the intermaterial heating-induced acoustic wave test with: a single volume of air (top); two volumes of air initially separated at $x^* = 22.5$ (middle); air and helium initially separated at $x^* = 22.5$ (bottom).
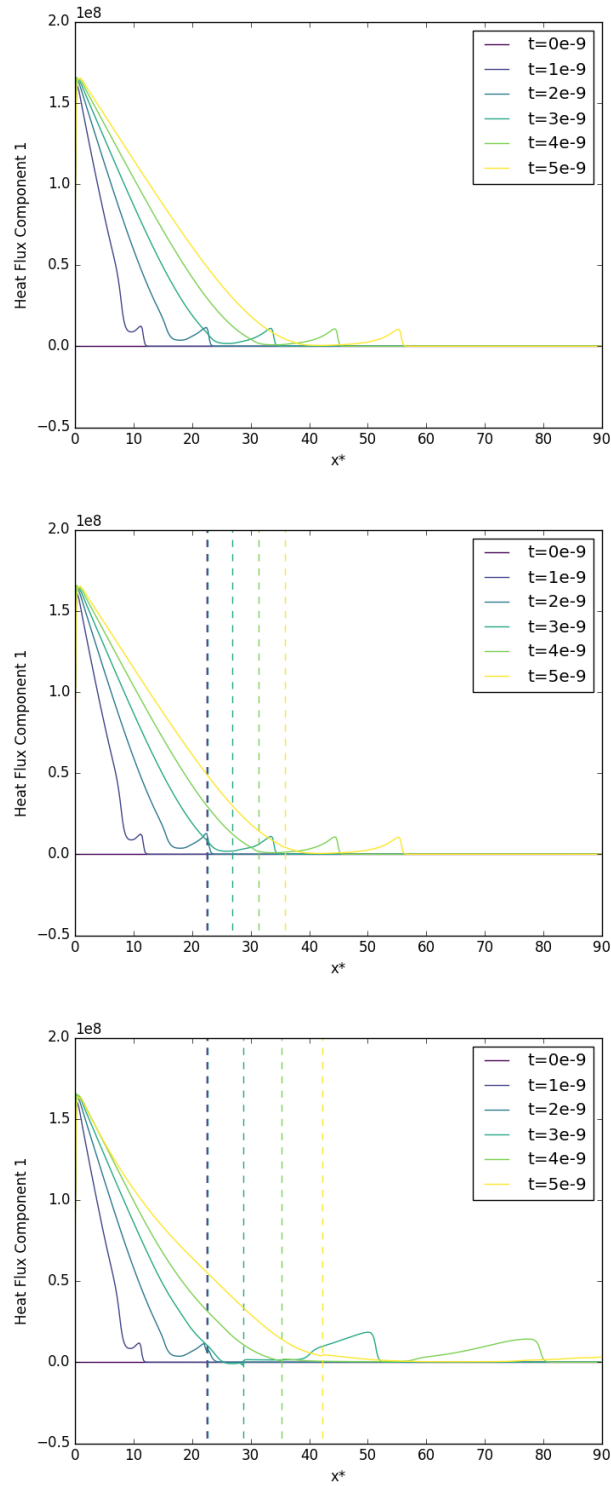
Figure 6.5: Heat flux for the intermaterial heating-induced acoustic wave test with: a single volume of air (top); two volumes of air initially separated at $x^* = 22.5$ (middle); air and helium initially separated at $x^* = 22.5$ (bottom).
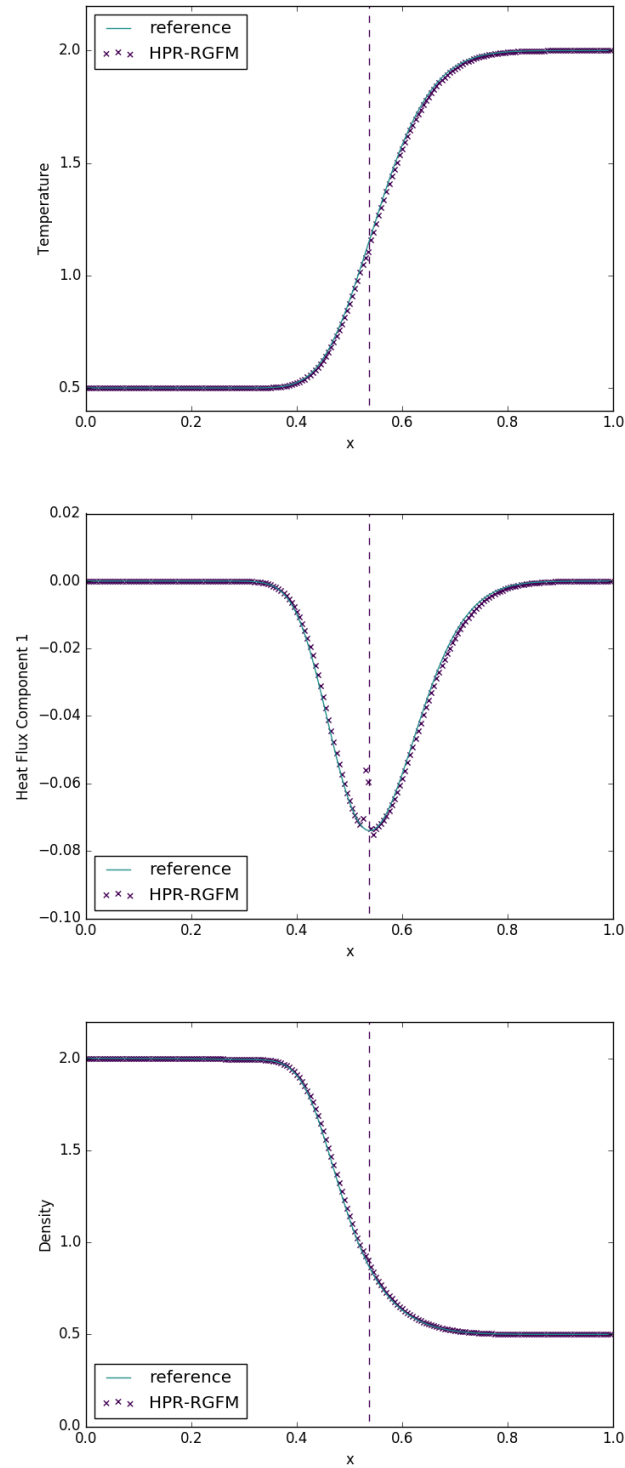
Figure 6.6: Temperature, heat flux, and density for the intermaterial heat conduction test with HPR-RGFM

Chapter 7

Conclusions

It has been demonstrated in Section 5.1, Section 5.2, and Section 5.3 that the HPR model coupled with Arrhenius reaction kinetics is capable of accurately modeling the deflagration and detonation phenomena required to simulate combustion. This system carries the benefits of being hyperbolic, as described in Section 1.1.

The two main novel developments of this study (the isobaric cookoff technique, and the HPR-RGFM) are discussed in Section 7.1 and Section 7.2 respectively, along with their limitations and potential improvements. Before discussing these specifics, it should be noted that there are several limitations applicable to this study as a whole. Firstly, all tests were carried out in 1D. Several multidimensional test cases are presented for the HPR model in [16, 31], including the circular explosion problem, the 3D Taylor-Green vortex, and the viscous double Mach reflection problem of Woodward and Colella [115], among others. However, several aspects of combustion are inherently multidimensional phenomena (such as hotspot formation, which can induce inhomogeneities in the profiles of combustion waves [102], or gas intrusions and channeling, which are important in deflagration-to-detonation processes [8]). The HPR model thus far has not been tested with any consideration of these phenomena, and this remains to be done.

The EOS used in this study was in every case either that of an ideal gas or a stiffened gas. Thus, solids could not be properly modeled. Although in the early days of cookoff simulation, generally only gases were considered, the focus now is very much on solids and the fluids that they interact with and produce over the course of the process. The isotropic hyperelastic EOS from [110] and the Mie-Grüneisen EOS are used with the HPR model in [16], providing some reference results against which to validate a future solid cookoff implementation. One outstanding problem regarding the HPR model is that of deriving a physically-relevant form of the function $\theta_1(\tau_1)$ that controls the evolution of the distortion tensor for each type of fluid or solid that one wishes to simulate. The form of θ_1 used in this study works well for Newtonian fluids[1], but is not appropriate for non-Newtonian fluids (where rate of strain is not

---

[1]A Newtonian fluid is one in which the shear rate is directly proportional to the shear stress.

directly proportional to shear stress) [31]. As of the time of writing, no other forms of θ_1 have been proposed, and this could form the basis of a future study.

Only a very simple one-step, single-phase reaction model was used in this study. In reality, reaction pathways are extremely complicated, and depending on the chemical species being modeled, this level of simplification may be highly inadequate. For example, Meredith et al. [74] recently simulated the ignition of HMX using a condensed-phase model consisting of two irreversible decomposition pathways and several subphases with different physical properties, and a gas-phase model with 45 species and 231 elementary reaction steps. In principle, the author sees no reason that the HPR model would not cope just as well with these processes as the models used in the cited paper. Transitioning between different phases would mean only varying the strain dissipation time, and perhaps the EOS; a great simplification to the multi-model frameworks typically used. Additionally, the interface dynamics could be treated with the HPR-RGFM, rather than the simplified, static interfaces used by Meredith et al.

Throughout this study, the various fluids have been assumed to be immiscible. Whilst this is a common assumption in situations where mixing is low or practically non-existent, there are many problems which may require it. It should be fairly straightforward to implement a mixture model such as that proposed by Romenski et al. [93, 94], which uses the same thermal conduction system as the HPR model. The results of Gross et al. [49] suggest that the isobaric cookoff technique would still be applicable to mixtures of fluids, as pressures still tend to equilibrate, but this is a complication that needs to be borne in mind.

7.1 The Isobaric Cookoff Technique

In Section 5.4 it was demonstrated that the method proposed in Section 4.2 can be used to significantly reduce the computational time in the heating phase of cookoff simulations on short bounded domains. An example of a real-world setup benefiting from this technique would be the constant-pressure HMX heating experiments of Renlund et al. [90]. Some examples of numerical experiments benefiting from this technique would be the heating phase of the simulations of Kapila, Schwendeman, et al. [63, 102], where the detonation response to different temperature gradients at constant pressure is investigated.

The isobaric cookoff technique is, in a sense, similar to existing techniques used in modeling solid cookoff, where the material is assumed not to flow in the heating phase [82]. The governing system of equations and its method of solution are, however, very different, and these previous models do not transform into a flow model upon detonation. The crucial realisation here is that fluid cookoff can be modeled in the same way if the acoustic wave generated by the heating hits bounding wall relatively early and pressure equilibrates over a relatively short period of time.

The isobaric cookoff technique is similar to the mass scaling technique described in Section 1.1, in that both produce an approximate, explicitly-solved system with a larger time step. Both techniques achieve a similar time step increment. Whilst the mass scaling technique applies not just to constant-pressure flows, the technique here is much more computationally efficient, retains the hyperbolic character of the thermal conduction, and does not produce spurious oscillations in the motions of the heated materials (as the materials are assumed to be motionless while only the reduced system is calculated).

Limitations

The isobaric cookoff technique only works on bounded domains which are relatively short in comparison to the speed of sound in the medium. This is because if the initial acoustic wave generated in the heating process does not reach the end of the domain early on in the simulation, the constant-pressure assumption will not be a realistic approximation to the system, leading to an incorrect calculation of the density (derived from the very accurate calculation of the temperature by the thermal subsystem).

Another problem with the method in its current form is that it assumes that the reactive material is structurally homogeneous. Whilst this may be a fair assumption in some situations for relatively inviscid gases, it is very unlikely to be realistic in many situations involving modeling detonations in solids, where gaps and thermal damage (porosity and cracks) develop over the long heating phase [118]. Inhomogeneities in the reactive materials can lead to very different outcomes, as demonstrated by Schwendeman and Kapila [102].

Potential Improvements

There are several improvements that can be made to the isobaric cookoff technique. Firstly, the current method of switching to the full system when 2.5% of the reactant has burnt is primitive. Choosing this level did not seem to incur any discrepancies in the results of Section 5.4, but at the very least it should be determined whether this level is optimal by a parameter study. A higher threshold would be desirable, as more of the process could be simulated with the quicker reduced system.

Leveque's *Large Time Step Method* [67] may present a further technique to speed up the calculation of the heating phase. This would require solution of the Riemann Problem of the thermal conduction subsystem of the HPR model. This is a relatively simple, conservative hyperbolic system with sources. Whilst there does not appear to be any published exact solutions available, there are a variety of techniques that could be applied to solve a Riemann Problem such as this (see Montecinos et al. for a recent overview [78]).

It may be that larger speed-ups than those demonstrated here could be achieved by the use of an implicit solver for the reduced system, owing to the larger time steps that this would permit. See Clutter [22] for some benchmark tests of explicit and implicit solvers for reactive systems. Implicit-Explicit (IMEX) methods are another technique [9, 10], involving solving the acoustic terms implicitly to avoid the acoustic CFL condition, while solving the advection and conduction terms explicitly, similarly to the method proposed in [72]. The explicit solves could be subcycled (repeated many times for each larger time step of the implicit solver), permitting the use of the larger implicit time steps. IMEX methods would allow the simulation of systems displaying non-constant pressure, acoustic waves, and flow.

Solving the equations at least partly implicitly requires the iterative solution of a non-linear system. This requires more algorithmic machinery and often tailored pre-conditioners to achieve good convergence speeds. The domain of dependence of the solution becomes the whole domain, in some sense destroying the localised nature of the hyperbolic system (and the associated benefits detailed in Section 1.3), and making impossible the trivial parallelisation inherent to the original system. This may prove more costly for very large grids, whereas the cost-per-iteration of an explicit solver to the hyperbolic system will not increase substantially, as long as additional computational cores are available. The performance of a method such as this, compared with

that proposed in this study, will depend to some extent on both algorithmic, software, and hardware implementations, and benchmarking for the desired usage cases should be performed to decide which is more desirable. It must also be borne in mind that the method proposed in this study is much simpler to implement, and the transition period from the reduced to the full system does not present any of the myriad issues commonly associated with implicit methods, discussed in Section 1.1.

Noting the large speed-up produced by the operator-splitting solver applied to the reduced system, it may be that the full system could be solved more quickly using a similar technique. Better-than-first-order accuracy has proved elusive so far with these methods applied to the HPR system, however [109]. This is critical for cookoff simulations, where the detonation waves and other phenomena will not be properly resolved with low-order methods. In any case, as noted in Chapter 2, the ADER-WENO schemes used in this study intuitively seem more expensive than necessary, and the development of less expensive methods is desirable.

It was noted in Section 5.4 that the reduced system detonates slightly later than the full system, owing to the fact that the convection of warm material away from the heated left boundary (a process ignored by the reduced system) results in slightly more energy being pumped into the full system, as the boundary is held at a fixed temperature. To ensure that exactly the same amount of energy has entered both systems at each point in time, a fixed flux boundary condition (as described in Section 2.4) could be used. It's important to note, however, that in the rudimentary implementation of this condition presented here, at each time step all the additional thermal energy resulting from the heat flux is added to just one boundary cell. If a very find grid is used, this will result in very large, nonphysical values for the temperature at the boundary. It may be possible to rectify this problem by smearing out the additional thermal energy at each time step over a layer a few cells thick at the boundary. Caution must be taken in deciding which proportions of the total additional energy to add to which cells, however, so that a physically-relevant solution is obtained. It may be instructive to obtain some analytical results regarding the depth of penetration of the heat flux over the time step, which would be available for the classical Fourier law of heat conduction in some situations. Alternatively, a subcycle of the thermal conduction system of the HPR model could be perform at the beginning of every time step to determine how far the heat flux penetrates the medium, given the temperature and density distribution around the boundary.

7.2 HPR-RGFM

The Riemann Ghost Fluid Method presented in Section 4.4 has been demonstrated to be a viable way of accurately simulating the interfaces between different materials described by the HPR model. Unlike in many existing implementations, heat conduction across the interface was simulated accurately. This greatly simplifies the conceptual framework required for multiphase interactions, as described in Section 1.1. Implementation should be easier and quicker, and future work can be more focused on a single model, rather than several fundamentally different frameworks.

Limitations

The truncation of the Taylor series expansions (4.40a) and (4.40b) used to find the star states of the heat flux and the viscous stress tensor implicitly assumes that there are only small differences between the side states and the star states of the variables upon which $q_1^*, \boldsymbol{\sigma_1^*}$ depend (ρ, p, J_1, and $\boldsymbol{A_1}$). If this is the case, higher order terms of the expansion can be neglected. If it is not, however, the method may fail.

The linearised nature of the HPR-RGFM solver also implicitly assumes that all waves of interest present in the Riemann Problem are shocks. Thus, strong rarefactions may cause the method to fail. An example of this is the failure of the HPR-RGFM on the water-gas shock tube test (taken from [18]). The domain $[0, 1]$ is initially occupied on $[0, 0.7]$ by water (with material parameters given in Section 6.2) and on $(0.7, 1]$ by air (with material parameters given in Section 6.3). The water initially has density 1000 and pressure 10^9. The air initially has density 50 and pressure 101325. The exact density and pressure resulting from simulating the problem with the Euler equations to time $t = 237.44 \times 10^{-6}$ are shown in Figure 7.1 on page 76. The material interface is located at $x = 0.8146$. Note the strong rarefaction on the left, and the large disparity between $p_L = 10^9$ and $p^* \approx 1.4 \times 10^7$, and similarly on the right side with $p_R \approx 10^5$.

Potential Improvements

An obvious improvement to the HPR-RGFM method presented would be to use a better Riemann solver than the iterative, linearised solver devised in Section 4.4. Let
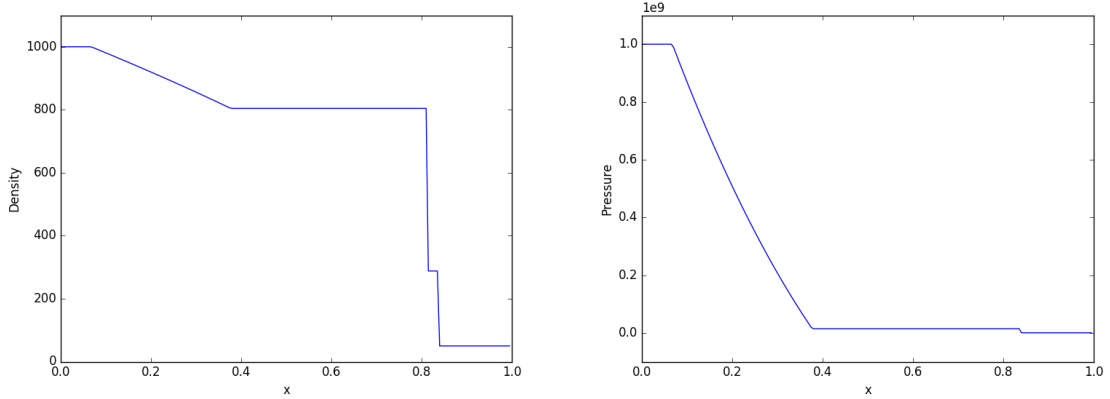
Figure 7.1: Density and pressure for the exact solution to the Euler equations for the water-gas shock tube test

L be the matrix of left eigenvectors of the primitive system. As noted previously, the solver relies upon the fact that each of the following relations holds along the characteristic to which it corresponds:

$$L \cdot \frac{d\boldsymbol{P}}{dt} = L \cdot \boldsymbol{S} \tag{7.1}$$

The right hand side was set to zero in the approximation process, but $\boldsymbol{S}$ can become arbitrarily stiff, as $\mu \to 0$. Thus, although no issues were raised in this study, there may well be times at which the source terms cannot be neglected. It may be that some numerical method is required to integrate (7.1) from the left and right interface boundary states to their respective star states.

Alternatively, a completely different approximate Riemann solver could be employed, such as the universal HLLEM solver of Dumbser et al. [25]. This path-conservative formulation of the HLLEM solver works for general non-conservative systems (such as the HPR model) and is simple to implement. It's based upon a new path-conservative HLL method (building on the original method of Harten, Lax, and van Leer [50]) but is claimed to be able to represent linearly degenerate intermediate waves "with a minimum of smearing" by evaluating the eigenvalues and eigenvectors of the intermediate characteristic fields (given in Section 4.3).

There are iterative exact Riemann solvers for the equations of non-linear elasticity (to which the HPR model reduces as $\tau_1 \to \infty$). Thus, they will work for applications

of the HPR model to solids problems (and perhaps to very viscous fluids problems too). Although these solvers are computationally expensive, they are only used once at each material interface point at each time step, and thus the added accuracy that they provide may be desirable. There are two ways to formulate the equations of non-linear elasticity: one in which the deformation tensor (the analogue of the inverse of the HPR model's distortion tensor) is evolved in time, and one in which its inverse (the analogue of A) is evolved instead. Miller's exact solver [77] uses the first formulation and the solver of Barton et al. [13] uses the second. The former can be used to evolve A^{-1}, from which A can be calculated. Unfortunately, both solvers critically assume that the source terms of the system vanish, and so are unlikely to produce the correct boundary conditions for the HPR-RGFM when modeling relatively inviscid fluids. It should also be noted that they cannot be used for problems involving heat conduction across material interfaces, and they do not take the thermal conduction subsystem of the HPR model into account.

If a different EOS is used in order to model solids, the derivations of the primitive systems matrices of the HPR model (given in Chapter B) will have to be performed again for each EOS, and the form of the eigenvectors will change (along with the systems solved to obtain the linearised approximations to the star states for use in the HPR-RGFM). Although this is tedious, it is a straightforward derivation to perform.

In Section 6.5 it was noted that the HPR-RGFM produces aberrations in the heat flux around the material interface, when using the temperature fix described in Section 4.4. Without using a better Riemann solver, a possible way to remedy this may be to specify the desired value of the heat flux in the star state, based on physical considerations, rather than obtaining it using the procedure detailed in Section 4.4. For example, take two different materials in thermal contact, with lengths $\Delta x_1, \Delta x_2$ and temperatures T_1, T_2 at their respective ends. If k_i is the thermal conductivity of material i, then by conservation of energy, the heat flux through the interface is given by the following equation, where h_c is the thermal conductance coefficient between the two materials:

$$q = \frac{T_1 - T_2}{\frac{\Delta x_1}{k_1} + \frac{\Delta x_2}{k_2} + \frac{1}{h_c}} \tag{7.2}$$

Usually, $\frac{1}{h_c} \approx 0$, and in fact it has been implicitly assumed to vanish in the models presented in this study. Introducing this fix for the heat flux could make the models more accurate in situations where $\frac{1}{h_c}$ diverges significantly from 0.

References

[1] *ALE3D.* https://wci.llnl.gov/simulation/computer-codes/ale3d.

[2] *Intel Math Kernel Library.* https://software.intel.com/en-us/articles/intel-mkl/.

[3] *The TOP500 Project.* https://www.top500.org.

[4] M. AIVAZIS, W. GODDARD, D. MEIRON, M. ORTIZ, J. POOL, AND J. SHEP-HERD, *A virtual test facility for simulating the dynamic response of materials*, Computing in Science & Engineering, 2 (2000), pp. 39–50.

[5] F. ALCRUDO AND F. BENKHALDOUN, *Exact solutions to the Riemann problem of the shallow water equations with a bottom step*, Computers & Fluids, 30 (2001), pp. 643–671.

[6] S. ARRHENIUS, *On the Reaction Velocity of the Inversion of Cane Sugar by Acids*, Zeitschrift für Physikalische Chemie, 4 (1889), pp. 226–248.

[7] ——, *The heat of dissociation of electrolytes and the influence of temperature on the degree of dissociation*, Wilhelm Engelmann, 1889.

[8] B. W. ASAY, *Non-Shock Initiation of Explosives*, Springer, 2010.

[9] U. M. ASCHER, S. J. RUUTH, AND R. J. SPITERI, *Implicit-explicit Runge-Kutta methods for time-dependent partial differential equations*, Applied Numerical Mathematics, 25 (1997), pp. 151–167.

[10] U. M. ASCHER, S. J. RUUTH, AND B. T. R. WETTON, *Implicit-Explicit Methods for Time-Dependent Partial Differential Equations*, SIAM Journal on Numerical Analysis, 32 (1995), pp. 797–823.

[11] F. BAMPI AND A. MORRO, *Viscous Fluids with Hidden Variables and Hyperbolic Systems*, Wave Motion, 2 (1980), pp. 153–157.

[12] P. T. BARTON AND D. DRIKAKIS, *An Eulerian method for multi-component problems in non-linear elasticity with sliding interfaces*, Journal of Computational Physics, 229 (2010), pp. 5518–5540.

[13] P. T. BARTON, D. DRIKAKIS, E. ROMENSKI, AND V. A. TITAREV, *Exact and approximate solutions of Riemann problems in non-linear elasticity*, Journal of Computational Physics, 228 (2009), pp. 7046–7068.

[14] P. T. BARTON, B. OBADIA, AND D. DRIKAKIS, *A conservative level-set based method for compressible solid/fluid problems on fixed grids*, Journal of Computational Physics, 230 (2011), pp. 7867–7890.

[15] R. BECKER, *Impact Waves and Detonation*, Zeitschrift für Physik, 8 (1929), p. 381.

[16] W. BOSCHERI, M. DUMBSER, AND R. LOUBERE, *Cell centered direct Arbitrary-Lagrangian-Eulerian ADER-WENO finite volume schemes for non-linear hyperelasticity*, International Journal for Numerical Methods in Fluids, 135 (2016), pp. 111–129.

[17] D. L. CHAPMAN, *On the Rate of Explosion in Gases*, Philosophical Magazine Series 5, 47 (1899), pp. 90–104.

[18] A. CHINNAYYA, E. DANIEL, AND R. SAUREL, *Modelling detonation waves in heterogeneous energetic materials*, Journal of Computational Physics, 196 (2004), pp. 490–538.

[19] J. F. CLARKE, D. R. KASSOY, AND N. RILEY, *Shocks generated in a confined gas due to rapid heat addition at the boundary*, Proceedings of the Royal Society of London A, 393 (1984), pp. 309–329.

[20] ——, *On the direct initiation of a plane detonation wave*, Proceedings of the Royal Society of London A, 408 (1986), pp. 129–148.

[21] ——, *On the evolution of plane detonations*, Proceedings of the Royal Society of London A, 429 (1990), pp. 259–283.

[22] J. K. CLUTTER, *Application of Computational Modeling for Explosive Hazard Assessments*, International Journal of Protective Structures, 4 (2013), pp. 293–314.

[23] A. COMPTE AND R. METZLER, *The generalized Cattaneo equation for the description of anomalous transport processes*, Journal of Physics A: Mathematical and General, 30 (1997), pp. 7277–7289.

[24] W. DORING, *On detonation processes in gases*, Annalen der Physik, 43 (1943), pp. 421–436.

[25] M. DUMBSER AND D. S. BALSARA, *A new efficient formulation of the HLLEM Riemann solver for general conservative and non-conservative hyperbolic systems*, Journal of Computational Physics, 304 (2016), pp. 275–319.

[26] M. DUMBSER, D. S. BALSARA, E. F. TORO, AND C. D. MUNZ, *A unified framework for the construction of one-step finite volume and discontinuous Galerkin schemes on unstructured meshes*, Journal of Computational Physics, 227 (2008), pp. 8209–8253.

[27] M. DUMBSER, M. CASTRO, C. PARES, AND E. F. TORO, *ADER schemes on unstructured meshes for nonconservative hyperbolic systems: Applications to geophysical flows*, Computers & Fluids, 38 (2009), pp. 1731–1748.

[28] M. DUMBSER, C. ENAUX, AND E. F. TORO, *Finite volume schemes of very high order of accuracy for stiff hyperbolic balance laws*, Journal of Computational Physics, 227 (2008), pp. 3971–4001.

[29] M. DUMBSER, A. HIDALGO, M. CASTRO, C. PARES, AND E. F. TORO, *FORCE schemes on unstructured meshes II: Non-conservative hyperbolic systems*, Computer Methods in Applied Mechanics & Engineering, 199 (2010), pp. 625–647.

[30] M. DUMBSER, A. HIDALGO, AND O. ZANOTTI, *High order space-time adaptive ADER-WENO finite volume schemes for non-conservative hyperbolic systems*, Computer Methods in Applied Mechanics & Engineering, 268 (2014), pp. 359–387.

[31] M. DUMBSER, I. PESHKOV, E. ROMENSKI, AND O. ZANOTTI, *High order ADER schemes for a unified first order hyperbolic formulation of continuum mechanics: viscous heat-conducting fluids and elastic solids*, Journal of Computational Physics, 314 (2015), pp. 824–862.

[32] M. DUMBSER AND E. F. TORO, *A simple extension of the Osher Riemann solver to non-conservative hyperbolic systems*, Journal of Scientific Computing, 48 (2011), pp. 70–88.

[33] ——, *On universal Osher-type schemes for general nonlinear hyperbolic conservation laws*, Communications in Computational Physics, 10 (2011), pp. 635–671.

[34] M. Dumbser and O. Zanotti, *Very high order PNPM schemes on unstructured meshes for the resistive relativistic MHD equations*, Journal of Computational Physics, 228 (2009), pp. 6991–7006.

[35] M. Dumbser, O. Zanotti, A. Hidalgo, and D. S. Balsara, *ADER-WENO finite volume schemes with space-time adaptive mesh refinement*, Journal of Computational Physics, 248 (2013), pp. 257–286.

[36] R. Fedkiw, T. Aslam, B. Merriman, and S. Osher, *A Non-oscillatory Eulerian Approach to Interfaces in Multimaterial Flows (the Ghost Fluid Method)*, Journal of Computational Physics, 152 (1999), pp. 457–492.

[37] R. P. Fedkiw, *Coupling an Eulerian Fluid Calculation to a Lagrangian Solid Calculation with the Ghost Fluid Method*, Journal of Computational Physics, 175 (2002), pp. 200–224.

[38] D. A. Frank-Kamenetskii, *Diffusion and Heat Exchange in Chemical Kinetics*, Princeton University Press, 1955.

[39] J. Frenkel, *Kinetic Theory of Liquids*, Oxford University Press, 1947.

[40] M. Fukuma and Y. Sakatani, *Relativistic Viscoelastic Fluid Mechanics*, International Journal of Modern Physics: Conference Series, 21 (2013), pp. 189–190.

[41] R. Geroch, *Relativistic theories of dissipative fluids*, Journal of Mathematical Physics, 36 (1995), pp. 4226–4241.

[42] N. S. Ghaisas, A. Subramaniam, and S. K. Lele, *High-Order Eulerian Methods for Elastic-Plastic Flow in Solids and Coupling with Fluid Flows*, 46th AIAA Fluid Dynamics Conference, (2016), pp. 1–17.

[43] J. Glimm and D. Marchesin, *A Numerical Method for Two Phase Flow with an Unstable Interface*, Journal of Computational Physics, 39 (1981), pp. 179–200.

[44] S. K. GODUNOV AND E. I. ROMENSKII, *Nonstationary equations of nonlinear elasticity theory in eulerian coordinates*, Journal of Applied Mechanics & Technical Physics, 13 (1974), pp. 868–884.

[45] H. GOMEZ, I. COLOMINAS, F. NAVARRINA, AND M. CASTELEIRO, *A finite element formulation for a convection-diffusion equation based on Cattaneo's law*, Computer Methods in Applied Mechanics & Engineering, 196 (2007), pp. 1757–1766.

[46] H. GOMEZ, I. COLOMINAS, F. NAVARRINA, J. PARES, AND M. CASTELEIRO, *A hyperbolic theory for advection-diffusion problems: Mathematical foundations and numerical modeling*, Archives of Computational Methods in Engineering, 17 (2010), pp. 191–211.

[47] P. GRESHO, *On the theory of semi-implicit projection methods for viscous incompressible flow and its implementation via a finite element method that also introduces a nearly consistent mass matrix. Part 1: Theory*, International Journal for Numerical Methods in Fluids, 11 (1990), pp. 587–620.

[48] ——, *On the theory of semi-implicit projection methods for viscous incompressible flow and its implementation via a finite element method that also introduces a nearly consistent mass matrix. Part 2: Implementation*, International Journal for Numerical Methods in Fluids, 11 (1990), pp. 587–620.

[49] M. L. GROSS, K. V. MEREDITH, AND M. W. BECKSTEAD, *Fast cook-off modeling of HMX*, Combustion & Flame, 162 (2015), pp. 3307–3315.

[50] A. HARTEN, P. D. LAX, AND B. VAN LEER, *On Upstream Differencing and Godunov-Type Schemes for Hyperbolic Conservation Laws*, SIAM Review, 25 (1983), pp. 35–61.

[51] C. HELZEL, R. J. LEVEQUE, AND G. WARNECKE, *A Modified Fractional Step Method for the Accurate Approximation of Detonation Waves*, SIAM Journal on Scientific Computing, 22 (2000), pp. 1489–1510.

[52] A. HIDALGO AND M. DUMBSER, *ADER schemes for nonlinear systems of stiff advection-diffusion-reaction equations*, Journal of Scientific Computing, 48 (2011), pp. 173–189.

[53] C. W. Hirt and B. D. Nichols, *Volume of fluid (VOF) method for the dynamics of free boundaries*, Journal of Computational Physics, 39 (1981), pp. 201–225.

[54] G. Hou, J. Wang, and A. Layton, *Numerical methods for fluid-structure interaction - A review*, Communications in Computational Physics, 12 (2012), pp. 337–377.

[55] W. M. Howard, M. A. Mcclelland, J. Knap, A. L. Nichols, and L. Livermore, *ALE3D Simulations of Gap Closure and Surface Ignition for Cookoff Modeling*, 13th International Detonation Symposium, (2006).

[56] B. Hübner, E. Walhorn, and D. Dinkler, *A monolithic approach to fluid-structure interaction using space-time finite elements*, Computer Methods in Applied Mechanics & Engineering, 193 (2004), pp. 2087–2104.

[57] W. Israel and J. M. Stewart, *Transient relativistic thermodynamics and kinetic theory*, Annals of Physics, 118 (1979), pp. 341–372.

[58] A. Jameson, *Formulation of Kinetic Energy Preserving Conservative Schemes for Gas Dynamics and Direct Numerical Simulation of One-Dimensional Viscous Compressible Flow in a Shock Tube Using Entropy and Kinetic Energy Preserving Schemes*, Journal of Scientific Computing, 34 (2008), pp. 188–208.

[59] G. S. Jiang and C. W. Shu, *Efficient implementation of weighted WENO schemes*, Journal of Computational Physics, 126 (1996), pp. 202–228.

[60] B. M. Johnson, *Analytical shock solutions at large and small Prandtl number*, Journal of Fluid Mechanics, 726 (2013), pp. 1–12.

[61] E. Jones, T. Oliphant, P. Peterson, and Others, *{SciPy}: Open source scientific tools for {Python}*.

[62] E. Jouget, *On the Propagation of Chemical Reactions in Gases*, Journal de Mathématiques Pures et Appliquées, 1 (1905), pp. 347–425.

[63] A. Kapila, D. W. Schwendeman, J. J. Quirk, and T. Hawa, *Mechanisms of detonation formation due to a temperature gradient*, Combustion Theory & Modelling, 6 (2002), pp. 553–594.

[64] S. A. Khairallah and A. Anderson, *Mesoscopic simulation model of selective laser melting of stainless steel powder*, Journal of Materials Processing Technology, 214 (2014), pp. 2627–2636.

[65] S. K. Lam, A. Pitrou, and S. Seibert, *Numba*, Proceedings of the Second Workshop on the LLVM Compiler Infrastructure in HPC - LLVM '15, (2015).

[66] A. Legay, J. Chessa, and T. Belytschko, *An Eulerian-Lagrangian method for fluid-structure interaction based on level sets*, Computer Methods in Applied Mechanics & Engineering, 195 (2006), pp. 2070–2087.

[67] R. J. Leveque, *A Large Time Step Generalization of Godunov 's Method for Systems of Conservation Laws*, SIAM Journal on Numerical Analysis, 22 (1985), pp. 1051–1073.

[68] T. G. Liu, B. C. Khoo, and K. S. Yeo, *Ghost fluid method for strong shock impacting on material interface*, Journal of Computational Physics, 190 (2003), pp. 651–681.

[69] T.-P. Liu, *The Riemann problem for general systems of conservation laws*, Journal of Differential Equations, 18 (1975), pp. 218–234.

[70] X.-D. Liu, S. Osher, and T. Chan, *Weighted essentially non-oscillatory schemes*, Journal of Computational Physics, 115 (1994), pp. 200–212.

[71] A. N. Malyshev and E. I. Romenski, *Hyperbolic Equations for Heat Transfer. Global Solvability of the Cauchy Problem*, Sibirskii Matematicheskii Zhurnal, 27 (1984), pp. 128–134.

[72] R. Mccallen, T. Dunn, A. Nichols, and J. Reaugh, *Modeling of Thermal Convection of Liquid TNT for Cookoff*, Proceedings of the NECDC 2002, (2003).

[73] M. A. McClelland, E. A. Glascoe, A. L. Nichols, S. P. Schofield, and H. K. Springer, *ALE3D Simulation of Incompressible Flow, Heat Transfer, and Chemical Decomposition of Comp B in Slow Cookoff Experiments*, 15th International Detonation Symposium, (2014).

[74] K. V. Meredith, M. L. Gross, and M. W. Beckstead, *Laser-induced ignition modeling of HMX*, Combustion & Flame, 162 (2015), pp. 506–515.

[75] L. Michael and N. Nikiforakis, *Coupling of elastoplastic solid models with condensed-phase explosives formulations*, (submitted), (2016).

[76] C. Michler, S. J. Hulshoff, E. H. van Brummelen, and R. de Borst, *A monolithic approach to fluid-structure interaction*, Computers & Fluids, 33 (2004), pp. 839–848.

[77] G. H. Miller, *An iterative Riemann solver for systems of hyperbolic conservation laws, with application to hyperelastic solid mechanics*, Journal of Computational Physics, 193 (2004), pp. 198–225.

[78] G. Montecinos, C. E. Castro, M. Dumbser, and E. F. Toro, *Comparison of solvers for the generalized Riemann problem for hyperbolic systems with source terms*, Journal of Computational Physics, 231 (2012), pp. 6472–6494.

[79] G. I. Montecinos, L. O. Müller, and E. F. Toro, *Hyperbolic reformulation of a 1D viscoelastic blood flow model and ADER finite volume schemes*, Journal of Computational Physics, 266 (2014), pp. 101–123.

[80] M. Morduchow and P. A. Libby, *On a Complete Solution of the One-Dimensional Flow Equations of a Viscous, Heat-Conducting, Compressible Gas*, tech. report, Polytechnic Institute of Brooklyn, 1949.

[81] E. D. Nering, *Linear Algebra and Matrix Theory*, 1970.

[82] A. L. Nichols and S. Schofield, *Modeling the Response of Fluid / Melt Explosives to Slow Cook-Off*, 15th International Detonation Symposium, (2014).

[83] H. Nishikawa, *A first-order system approach for diffusion equation. II: Unification of advection and diffusion*, Journal of Computational Physics, 229 (2010), pp. 3989–4016.

[84] S. Osher and R. Fedkiw, *Level Set Methods and Dynamic Implicit Surfaces*, Springer, 2002.

[85] I. Peshkov and E. Romenski, *A hyperbolic model for viscous Newtonian flows*, Continuum Mechanics & Thermodynamics, 28 (2016), pp. 85–104.

[86] F. D. Pin, S. Idelsohn, E. Onate, and R. Aubry, *The ALE/Lagrangian Particle Finite Element Method: A new approach to computation of free-surface flows and fluid-object interactions*, Computers & Fluids, 36 (2007), pp. 27–38.

[87] A. PRIOR, *Applications of implicit and explicit finite element techniques to metal forming*, Journal of Materials Processing Technology, 45 (1994), pp. 649–656.

[88] L. RAYLEIGH, *On the motion of solid bodies through viscous liquid*, Philosophical Magazine Series 6, 21 (1911), pp. 697–711.

[89] T. REN, J. HU, T. XIONG, AND J. M. QIU, *Runge-Kutta central discontinuous Galerkin BGK method for the Navier-Stokes equations*, Journal of Computational Physics, 274 (2014), pp. 592–610.

[90] A. M. RENLUND, J. C. MILLER, W. M. TROTT, K. L. ERICKSON, M. L. HOBBS, R. G. SCHMITT, G. W. WELLMAN, AND M. R. BAER, *Characterization of Thermally Degraded Energetic Materials*, tech. report, Sandia National Laboratories, 1997.

[91] R. D. RITCHTMYER, *Difference methods for initial-value problems*, Interscience, 1957.

[92] P. ROMATSCHKE, *New Developments in Relativistic Viscous Hydrodynamics*, International Journal of Modern Physics E, 19 (2010), pp. 1–53.

[93] E. ROMENSKI, D. DRIKAKIS, AND E. TORO, *Conservative models and numerical methods for compressible two-phase flow*, Journal of Scientific Computing, 42 (2010), pp. 68–95.

[94] E. ROMENSKI, A. D. RESNYANSKY, AND E. F. TORO, *Conservative Hyperbolic Formulation for Compressible Two-Phase Flow with Different Phase Pressures and Temperatures*, Quarterly of Applied Mathematics, 65 (2007), pp. 259–279.

[95] E. I. ROMENSKI, *Hyperbolic Equations of Maxwell's Nonlinear Model of Elastoplastic Heat-Conducting Media*, Sibirskii Matematicheskii Zhurnal, 30 (1988), pp. 135–159.

[96] R. ROSSI AND E. OÑATE, *Analysis of some partitioned algorithms for fluid-structure interaction*, Engineering Computations, 27 (2010), pp. 20–56.

[97] P. B. RYZHAKOV, R. ROSSI, S. R. IDELSOHN, AND E. ONATE, *A monolithic Lagrangian approach for fluid-structure interaction problems*, Computational Mechanics, 46 (2010), pp. 883–899.

[98] S. K. Sambasivan and H. S. UdayKumar, *Ghost Fluid Method for Strong Shock Interactions Part 1: Fluid-Fluid Interfaces*, AIAA Journal, 47 (2009), pp. 2907–2922.

[99] ——, *Ghost Fluid Method for Strong Shock Interactions Part 2: Immersed Solid Boundaries*, AIAA Journal, 47 (2009), pp. 2923–2937.

[100] H. Schlichting, *Boundary-Layer Theory*, McGraw-Hill, 1979.

[101] S. Schoch, K. Nordin-Bates, and N. Nikiforakis, *An Eulerian algorithm for coupled simulations of elastoplastic-solids and condensed-phase explosives*, Journal of Computational Physics, 252 (2013), pp. 163–194.

[102] D. W. Schwendeman and A. K. Kapila, *Effect of Thermal Nonhomogeneity on Explosion or Detonation in an Annular Cookoff*, 12th International Detonation Symposium, (2002), pp. 1–11.

[103] J. Selesovský, *Thermal loading of explosives–finite difference method with time step reduction.*, Journal of Hazardous Materials, 174 (2010), pp. 289–94.

[104] G. J. Sharpe and M. Short, *Shock-induced ignition of thermally sensitive explosives*, IMA Journal of Applied Mathematics, 69 (2004), pp. 493–520.

[105] M. Short, *On the Critical Conditions for the Initiation of a Detonation in a Nonuniformly Perturbed Reactive Fluid*, SIAM Journal on Applied Mathematics, 57 (1997), pp. 1242–1280.

[106] G. A. Sod, *A survey of several finite difference methods for systems of nonlinear hyperbolic conservation laws*, Journal of Computational Physics, 27 (1978), pp. 1–31.

[107] G. G. Stokes, *On the Effect of the Internal Friction of Fluids on the Motion of Pendulums*, Transactions of the Cambridge Philosophical Society, 9 (1850).

[108] M. Sućeska and S. Matečić-Muśanić, *Numerical Modeling of Self-Ignition of Energetic Materials*, Central European Journal of Energetic Materials, 1 (2004), pp. 23–41.

[109] K. Sverdrup, *Numerical Solutions of the Multidimensional HPR Equations using Finite Volume Methods with Splitting Schemes*, Master's Thesis, University of Cambridge, (2016).

[110] V. A. TITAREV, E. ROMENSKI, AND E. F. TORO, *MUSTA-type upwind fluxes for non-linear elasticity*, International Journal for Numerical Methods in Engineering, 73 (2008), pp. 897–926.

[111] E. F. TORO, *On Glimm-Related Schemes for Conservation Laws*, Preprint MMU-9602, Department of Mathematics & Physics, Manchester Metropolitan University, UK, (1996).

[112] E. F. TORO, *Riemann Solvers and Numerical Methods for Fluid Dynamics: A Practical Introduction*, Springer, 2009.

[113] J. VON NEUMANN, *Theory of Detonation Waves*, tech. report, Institute for Advanced Study, 1942.

[114] S. P. WANG, M. H. ANDERSON, J. G. OAKLEY, M. L. CORRADINI, AND R. BONAZZA, *A thermodynamically consistent and fully conservative treatment of contact discontinuities for compressible multicomponent flows*, Journal of Computational Physics, 195 (2004), pp. 528–559.

[115] P. WOODWARD, *The Numerical Simulation of Two-Dimensional Fluid Flow with Strong Shocks*, Journal of Computational Physics, 54 (1984), pp. 115–173.

[116] V. YAKHOT, *A New Approach to Modelling Strongly Non-Equilibrium, Time-Dependent Turbulent Flows*, tech. report, Institute for Advanced Study, 2003.

[117] J. J. YOH, *Simulating the Thermal Response of High Explosives on Time Scales of Days to Microseconds*, AIP Conference Proceedings, (2004), pp. 425–428.

[118] J. J. YOH, M. A. MCCLELLAND, J. L. MAIENSCHEIN, L. NICHOLS, AND J. F. WARDELL, *Towards An Ideal Slow Cookoff Model For PBXN-109*, JANNAF 2003 Conference Proceedings, (2003).

[119] J. J. YOH, M. A. MCCLELLAND, J. L. MAIENSCHEIN, AND J. F. WARDELL, *Towards a predictive thermal explosion model for energetic materials*, Journal of Computer-Aided Materials Design, 10 (2003), pp. 175–189.

[120] Y. B. ZELDOVICH, *On the Theory of the Propagation of Detonation in Gaseous Systems*, Journal of Experimental & Theoretical Physics, 10 (1940), pp. 542–568.

Appendix A

Derivatives of Dependent Variables

The following results are used in later sections of the appendix.

Spatial Derivatives

Note that:

$$
\begin{aligned}
\frac{\partial T}{\partial x_k} &= \frac{1}{c_v\,(\gamma - 1)\,\rho}\frac{\partial p}{\partial x_k} - \frac{p + p_\infty}{c_v\,(\gamma - 1)\,\rho^2}\frac{\partial \rho}{\partial x_k} \\
&= \frac{T}{p + p_\infty}\frac{\partial p}{\partial x_k} - \frac{T}{\rho}\frac{\partial \rho}{\partial x_k}
\end{aligned}
\tag{A.1}
$$

Thus:

$$
\begin{aligned}
\frac{\partial q_i}{\partial x_k} &= \alpha^2 \frac{\partial T}{\partial x_k} J_i + \alpha^2 T \frac{\partial J_i}{\partial x_k} \\
&= \frac{\alpha^2 T J_i}{p + p_\infty}\frac{\partial p}{\partial x_k} - \frac{\alpha^2 T J_i}{\rho}\frac{\partial \rho}{\partial x_k} + \alpha^2 T \frac{\partial J_i}{\partial x_k} \\
&= \frac{q_i}{p + p_\infty}\frac{\partial p}{\partial x_k} - \frac{q_i}{\rho}\frac{\partial \rho}{\partial x_k} + \alpha^2 T \frac{\partial J_i}{\partial x_k}
\end{aligned}
\tag{A.2}
$$

Additionally, with E defined as in (1.7):

$$
\frac{\partial E}{\partial x_k} = \frac{1}{(\gamma - 1)\,\rho}\frac{\partial p}{\partial x_i} - \frac{E_1}{\rho}\frac{\partial \rho}{\partial x_k} + \psi_{mn}\frac{\partial A_{mn}}{\partial x_k} + \alpha^2 J_m \frac{\partial J_m}{\partial x_k} + v_m \frac{\partial v_m}{\partial x_k}
\tag{A.3}
$$

As $\frac{\partial E}{\partial A}$ is a function of A only, $\frac{\partial \sigma}{\partial \rho} = \frac{\sigma}{\rho}$, giving:

$$
\begin{aligned}
\frac{\partial \sigma_{ik}}{\partial x_k} &= \frac{\partial \sigma_{ik}}{\partial \rho}\frac{\partial \rho}{\partial x_k} + \frac{\partial \sigma_{ik}}{\partial A_{mn}}\frac{\partial A_{mn}}{\partial x_k} \\
&= \frac{\sigma_{ik}}{\rho}\frac{\partial \rho}{\partial x_k} + \frac{\partial \sigma_{ik}}{\partial A_{mn}}\frac{\partial A_{mn}}{\partial x_k}
\end{aligned}
\tag{A.4}
$$

Derivatives with Respect to the Distortion Tensor

Note that:

$$\frac{\partial A_{ki}A_{kj}}{\partial A_{mn}} = \frac{\partial A_{ki}}{\partial A_{mn}}A_{kj} + A_{ki}\frac{\partial A_{kj}}{\partial A_{mn}} = \delta_{km}\delta_{in}A_{kj} + A_{ki}\delta_{km}\delta_{jn} \tag{A.5}$$

As $G_{ij} = \left(A^T A\right)_j = A_{ki}A_{kj}$:

$$\frac{\partial G_{ij}}{\partial A_{mn}} = \delta_{in}A_{mj} + \delta_{jn}A_{mi} \tag{A.6a}$$

$$\frac{\partial \operatorname{tr}(G)}{\partial A_{mn}} = \frac{\partial G_{kk}}{\partial A_{mn}} = 2A_{mn} \tag{A.6b}$$

Combining these results:

$$\frac{\partial \operatorname{dev}(G)_{ij}}{\partial A_{mn}} = \delta_{in}A_{mj} + \delta_{jn}A_{mi} - \frac{2}{3}\delta_{ij}A_{mn} \tag{A.7}$$

Thus:

$$
\begin{aligned}
\frac{\partial \left(G \operatorname{dev}(G)\right)_{ij}}{\partial A_{mn}} &= \frac{\partial G_{it}}{\partial A_{mn}}\operatorname{dev}(G)_{tj} + G_{it}\frac{\partial \operatorname{dev}(G)_{tj}}{\partial A_{mn}} \\
&= (\delta_{in}A_{mt} + \delta_{tn}A_{mi})\left(A_{kt}A_{kj} - \frac{1}{3}A_{kl}A_{kl}\delta_{tj}\right) \\
&\quad + (A_{ki}A_{kt})\left(\delta_{tn}A_{mj} + \delta_{jn}A_{mt} - \frac{2}{3}\delta_{tj}A_{mn}\right) \\
&= \delta_{in}\left(A_{mt}A_{kt}A_{kj} - \frac{1}{3}A_{mj}A_{kl}A_{kl}\right) + \delta_{jn}\left(A_{ki}A_{kt}A_{mt} - \frac{1}{3}A_{mi}A_{kl}A_{kl}\right) \\
&\quad + A_{mi}A_{kn}A_{kj} + A_{ki}A_{kn}A_{mj} - \frac{2}{3}A_{ki}A_{kj}A_{mn}
\end{aligned} \tag{A.8}
$$

Thus, as $\sigma = -\rho c_s^2 G \operatorname{dev}(G)$, the partial derivative of σ with respect to A, holding ρ constant, is given by:

$$\frac{\partial \sigma_{ij}}{\partial A_{mn}} = -c_s^2 \rho \left(\delta_{in}\left(A \operatorname{dev}(G)\right)_{mj} + \delta_{jn}\left(A \operatorname{dev}(G)\right)_{mi} + A_{mi}G_{jn} + A_{mj}G_{in} - \frac{2}{3}G_{ij}A_{mn}\right) \tag{A.9}$$

Appendix B

Matrix Forms of the HPR Model

The conserved and primitive variables of the HPR model are given, respectively, by:

$$\boldsymbol{Q} = \begin{pmatrix} \rho & \rho E & \rho v_1 & \rho v_2 & \rho v_3 & A_{11} & A_{21} & A_{31} & A_{12} & A_{22} & A_{32} & A_{13} & A_{23} & A_{33} & \rho J_1 & \rho J_2 & \rho J_3 \end{pmatrix}^T \quad \text{(B.1)}$$

$$\boldsymbol{P} = \begin{pmatrix} \rho & p & A_{11} & A_{21} & A_{31} & A_{12} & A_{22} & A_{32} & A_{13} & A_{23} & A_{33} & v_1 & v_2 & v_3 & J_1 & J_2 & J_3 \end{pmatrix}^T \quad \text{(B.2)}$$

$\boldsymbol{Q}$ is given here in the ordering found in the literature [16, 31, 85]. $\boldsymbol{P}$ is given in a different ordering, allowing the system matrix and eigenvectors of the primitive formulation of the HPR model to be expressed more succinctly in Section 4.3 and Chapter C.

Equations (1.2a), (1.4), (1.2b), (1.2c), (1.2d) can be put in the following form:

$$\frac{\partial \boldsymbol{Q}}{\partial t} + \frac{\partial \boldsymbol{F_1}}{\partial x_1} + \frac{\partial \boldsymbol{F_2}}{\partial x_2} + \frac{\partial \boldsymbol{F_3}}{\partial x_3} + B_1 \frac{\partial \boldsymbol{Q}}{\partial x_1} + B_2 \frac{\partial \boldsymbol{Q}}{\partial x_2} + B_3 \frac{\partial \boldsymbol{Q}}{\partial x_3} = \boldsymbol{S}\left(\boldsymbol{Q}\right) \quad \text{(B.3)}$$

where $\boldsymbol{F_i}, B_i, \boldsymbol{S}$ are given in the last section of the appendices. This is equivalent to the following system:

$$\frac{\partial \boldsymbol{Q}}{\partial t} + Z_1 \frac{\partial \boldsymbol{Q}}{\partial x_1} + Z_2 \frac{\partial \boldsymbol{Q}}{\partial x_2} + Z_3 \frac{\partial \boldsymbol{Q}}{\partial x_3} = \boldsymbol{S}\left(\boldsymbol{Q}\right) \quad \text{(B.4)}$$

$$Z_i = \frac{\partial \boldsymbol{F_i}}{\partial \boldsymbol{P}} \frac{\partial \boldsymbol{P}}{\partial \boldsymbol{Q}} + B_i \quad \text{(B.5)}$$

$\frac{\partial \boldsymbol{F_i}}{\partial \boldsymbol{P}}, \frac{\partial \boldsymbol{P}}{\partial \boldsymbol{Q}}$ are also given in the last section of the appendices.

Primitive Form of the HPR Model

Applying the product rule to (1.4), (1.2b), (1.2c), (1.2d):

$$\frac{\partial \rho}{\partial t} + \frac{\partial (\rho v_k)}{\partial x_k} = 0 \tag{B.6a}$$

$$\frac{\partial (\rho E)}{\partial t} + v_k \frac{\partial (\rho E)}{\partial x_k} + \rho E \frac{\partial v_k}{\partial x_k} + \frac{\partial (v_i (p\delta_{ik} - \sigma_{ik}) + q_k)}{\partial x_k} = 0 \tag{B.6b}$$

$$\frac{\partial A_{ij}}{\partial t} + v_k \frac{\partial A_{ik}}{\partial x_j} + A_{ik} \frac{\partial v_k}{\partial x_j} + v_k \left(\frac{\partial A_{ij}}{\partial x_k} - \frac{\partial A_{ik}}{\partial x_j} \right) = -\frac{\psi_{ij}}{\theta_1(\tau_1)} \tag{B.6c}$$

$$v_i \frac{\partial \rho}{\partial t} + \rho \frac{\partial v_i}{\partial t} + v_i \frac{\partial (\rho v_k)}{\partial x_k} + \rho v_k \frac{\partial v_i}{\partial x_k} + \frac{\partial (p\delta_{ik} - \sigma_{ik})}{\partial x_k} = 0 \tag{B.6d}$$

$$J_i \frac{\partial \rho}{\partial t} + \rho \frac{\partial J_i}{\partial t} + J_i \frac{\partial (\rho v_k)}{\partial x_k} + \rho v_k \frac{\partial J_i}{\partial x_k} + \frac{\partial T}{\partial x_i} = -\frac{\rho H_i}{\theta_2(\tau_2)} \tag{B.6e}$$

Inserting the first equation into the fourth and fifth, simplifying the third, and applying the chain rule to the temporal and spatial derivatives in the second:

$$\frac{\partial \rho}{\partial t} + \frac{\partial (\rho v_k)}{\partial x_k} = 0 \tag{B.7a}$$

$$\frac{\partial (\rho E)}{\partial \rho} \frac{D\rho}{Dt} + \frac{\partial (\rho E)}{\partial v_i} \frac{Dv_i}{Dt} + \frac{\partial (\rho E)}{\partial A_{ij}} \frac{DA_{ij}}{Dt} + \frac{\partial (\rho E)}{\partial J_i} \frac{DJ_i}{Dt} + \frac{\partial (\rho E)}{\partial p} \frac{Dp}{Dt} \tag{B.7b}$$

$$+ \rho E \frac{\partial v_k}{\partial x_k} + \frac{\partial (v_i (p\delta_{ik} - \sigma_{ik}) + q_k)}{\partial x_k} = 0$$

$$\frac{\partial A_{ij}}{\partial t} + v_k \frac{\partial A_{ij}}{\partial x_k} + A_{ik} \frac{\partial v_k}{\partial x_j} = -\frac{\psi_{ij}}{\theta_1(\tau_1)} \tag{B.7c}$$

$$\frac{\partial v_i}{\partial t} + v_k \frac{\partial v_i}{\partial x_k} + \frac{1}{\rho} \frac{\partial (p\delta_{ik} - \sigma_{ik})}{\partial x_k} = 0 \tag{B.7d}$$

$$\frac{\partial J_i}{\partial t} + v_k \frac{\partial J_i}{\partial x_k} + \frac{1}{\rho} \frac{\partial T}{\partial x_i} = -\frac{H_i}{\theta_2(\tau_2)} \tag{B.7e}$$

where $\frac{DX}{Dt} = \frac{\partial X}{\partial t} + v_k \frac{\partial X}{\partial x_k}$ is the material derivative of quantity X. Inserting the first, third, and fourth equations into the second:

$$0 = \frac{\partial\left(\rho E\right)}{\partial \rho}\left(-\rho\frac{\partial v_k}{\partial x_k}\right) + \frac{\partial\left(\rho E\right)}{\partial v_i}\left(-\frac{1}{\rho}\frac{\partial\left(p\delta_{ik} - \sigma_{ik}\right)}{\partial x_k}\right) \tag{B.8}$$
$$+ \frac{\partial\left(\rho E\right)}{\partial A_{ij}}\left(-\frac{\psi_{ij}}{\theta_1(\tau_1)} - A_{ik}\frac{\partial v_k}{\partial x_j}\right) + \frac{\partial\left(\rho E\right)}{\partial J_i}\left(-\frac{H_i}{\theta_2(\tau_2)} - \frac{1}{\rho}\frac{\partial T}{\partial x_i}\right)$$
$$+ \frac{\partial\left(\rho E\right)}{\partial p}\left(\frac{\partial p}{\partial t} + v_k\frac{\partial p}{\partial x_k}\right) + \rho E\frac{\partial v_k}{\partial x_k} + \frac{\partial\left(v_i\left(p\delta_{ik} - \sigma_{ik}\right) + q_k\right)}{\partial x_k}$$

When holding p constant rather than s, for the equations of state used in this study:

$$\rho^2\frac{\partial E}{\partial \rho} = -\frac{p}{\gamma - 1} \tag{B.9}$$

Thus, applying the product rule to $\frac{\partial(\rho E)}{\partial \rho}$:

$$0 = \frac{p}{\gamma - 1}\frac{\partial v_k}{\partial x_k} - \frac{\partial\left(\rho E\right)}{\partial v_i}\left(\frac{1}{\rho}\frac{\partial\left(p\delta_{ik} - \sigma_{ik}\right)}{\partial x_k}\right) \tag{B.10}$$
$$- \frac{\partial\left(\rho E\right)}{\partial A_{ij}}\left(\frac{\psi_{ij}}{\theta_1(\tau_1)} + A_{ik}\frac{\partial v_k}{\partial x_j}\right) - \frac{\partial\left(\rho E\right)}{\partial J_i}\left(\frac{H_i}{\theta_2(\tau_2)} + \frac{1}{\rho}\frac{\partial T}{\partial x_i}\right)$$
$$+ \frac{\partial\left(\rho E\right)}{\partial p}\left(\frac{\partial p}{\partial t} + v_k\frac{\partial p}{\partial x_k}\right) + \frac{\partial\left(v_i\left(p\delta_{ik} - \sigma_{ik}\right) + q_k\right)}{\partial x_k}$$

$\frac{\partial(\rho E)}{\partial v_i} = \rho v_i$, so applying the product rule to the last term:

$$0 = \frac{p}{\gamma - 1}\frac{\partial v_k}{\partial x_k} - \frac{\partial\left(\rho E\right)}{\partial A_{ij}}\left(\frac{\psi_{ij}}{\theta_1(\tau_1)} + A_{ik}\frac{\partial v_k}{\partial x_j}\right) - \frac{\partial\left(\rho E\right)}{\partial J_i}\left(\frac{H_i}{\theta_2(\tau_2)} + \frac{1}{\rho}\frac{\partial T}{\partial x_i}\right) \tag{B.11}$$
$$+ \frac{\partial\left(\rho E\right)}{\partial p}\left(\frac{\partial p}{\partial t} + v_k\frac{\partial p}{\partial x_k}\right) + \left(p\delta_{ik} - \sigma_{ik}\right)\frac{\partial v_i}{\partial x_k} + \frac{\partial q_k}{\partial x_k}$$

Thus:

$$\frac{\psi_{ij}}{\theta_1(\tau_1)}\frac{\partial\left(\rho E\right)}{\partial A_{ij}} + \frac{H_i}{\theta_2(\tau_2)}\frac{\partial\left(\rho E\right)}{\partial J_i} = -\frac{\partial\left(\rho E\right)}{\partial A_{ij}}A_{ik}\frac{\partial v_k}{\partial x_j} - \frac{\partial\left(\rho E\right)}{\partial J_i}\frac{1}{\rho}\frac{\partial T}{\partial x_i} \tag{B.12}$$
$$+ \frac{\partial\left(\rho E\right)}{\partial p}\left(\frac{\partial p}{\partial t} + v_k\frac{\partial p}{\partial x_k}\right) + \frac{\gamma p}{\gamma - 1}\frac{\partial v_k}{\partial x_k}$$
$$- \sigma_{ik}\frac{\partial v_i}{\partial x_k} + \frac{\partial q_k}{\partial x_k}$$

Using (A.1), (A.2) and the fact that $\frac{\partial(\rho E)}{\partial J_i} = \rho\alpha^2 J_i$:

$$\frac{\psi_{ij}}{\theta_1(\tau_1)}\frac{\partial\left(\rho E\right)}{\partial A_{ij}} + \frac{H_i}{\theta_2(\tau_2)}\frac{\partial\left(\rho E\right)}{\partial J_i} = -\frac{\partial\left(\rho E\right)}{\partial A_{ij}}A_{ik}\frac{\partial v_k}{\partial x_j} + \frac{\partial\left(\rho E\right)}{\partial p}\left(\frac{\partial p}{\partial t} + v_k\frac{\partial p}{\partial x_k}\right) \tag{B.13}$$
$$+ \frac{\gamma p}{\gamma - 1}\frac{\partial v_k}{\partial x_k} - \sigma_{ik}\frac{\partial v_i}{\partial x_k} + \alpha^2 T\frac{\partial J_k}{\partial x_k}$$

Reindexing the first term gives:

$$\frac{\psi_{ij}}{\theta_1(\tau_1)}\frac{\partial\left(\rho E\right)}{\partial A_{ij}} + \frac{H_i}{\theta_2(\tau_2)}\frac{\partial\left(\rho E\right)}{\partial J_i} = \frac{\partial\left(\rho E\right)}{\partial p}\left(\frac{\partial p}{\partial t} + v_k\frac{\partial p}{\partial x_k}\right) - \left(\frac{\partial\left(\rho E\right)}{\partial A_{jk}}A_{ji} + \sigma_{ik}\right)\frac{\partial v_i}{\partial x_k} \tag{B.14}$$
$$+ \frac{\gamma p}{\gamma - 1}\frac{\partial v_k}{\partial x_k} + \alpha^2 T\frac{\partial J_k}{\partial x_k}$$

As $\sigma = -\rho A^T\frac{\partial E}{\partial A}$, the second term disappears. Thus, noting that $\frac{\partial(\rho E)}{\partial p} = \frac{1}{\gamma - 1}$, $\psi = \frac{\partial E}{\partial A}$, and $H = \frac{\partial E}{\partial J}$, the full system is:

$$\frac{\partial\rho}{\partial t} + \frac{\partial\left(\rho v_k\right)}{\partial x_k} = 0 \tag{B.15a}$$

$$\frac{\partial p}{\partial t} + v_k\frac{\partial p}{\partial x_k} + \gamma p\frac{\partial v_k}{\partial x_k} + (\gamma - 1)\alpha^2 T\frac{\partial J_k}{\partial x_k} = (\gamma - 1)\rho\left(\frac{\psi_{ij}\psi_{ij}}{\theta_1(\tau_1)} + \frac{H_i H_i}{\theta_2(\tau_2)}\right) \tag{B.15b}$$

$$\frac{\partial A_{ij}}{\partial t} + v_k\frac{\partial A_{ij}}{\partial x_k} + A_{ik}\frac{\partial v_k}{\partial x_j} = -\frac{\psi_{ij}}{\theta_1(\tau_1)} \tag{B.15c}$$

$$\frac{\partial v_i}{\partial t} + v_k\frac{\partial v_i}{\partial x_k} + \frac{1}{\rho}\frac{\partial\left(p\delta_{ik} - \sigma_{ik}\right)}{\partial x_k} = 0 \tag{B.15d}$$

$$\frac{\partial J_i}{\partial t} + v_k\frac{\partial J_i}{\partial x_k} + \frac{1}{\rho}\frac{\partial T}{\partial x_i} = -\frac{H_i}{\theta_2(\tau_2)} \tag{B.15e}$$

Using the expressions (A.4) and (A.1), the full set of equations, in primitive form, is:

$$\frac{\partial \rho}{\partial t} + v_k \frac{\partial \rho}{\partial x_k} + \rho \frac{\partial v_k}{\partial x_k} = 0 \tag{B.16a}$$

$$\frac{\partial p}{\partial t} + v_k \frac{\partial p}{\partial x_k} + \gamma p \frac{\partial v_k}{\partial x_k} + (\gamma - 1)\,\alpha^2 T \frac{\partial J_k}{\partial x_k} = (\gamma - 1)\,\rho \left(\frac{\psi_{ij}\psi_{ij}}{\theta_1(\tau_1)} + \frac{H_i H_i}{\theta_2(\tau_2)} \right) \tag{B.16b}$$

$$\frac{\partial A_{ij}}{\partial t} + v_k \frac{\partial A_{ij}}{\partial x_k} + A_{ik} \frac{\partial v_k}{\partial x_j} = -\frac{\psi_{ij}}{\theta_1(\tau_1)} \tag{B.16c}$$

$$\frac{\partial v_i}{\partial t} + v_k \frac{\partial v_i}{\partial x_k} + \frac{1}{\rho} \frac{\partial p}{\partial x_i} - \frac{\sigma_{ik}}{\rho^2} \frac{\partial \rho}{\partial x_k} - \frac{1}{\rho} \frac{\partial \sigma_{ik}}{\partial A_{mn}} \frac{\partial A_{mn}}{\partial x_k} = 0 \tag{B.16d}$$

$$\frac{\partial J_i}{\partial t} + v_k \frac{\partial J_i}{\partial x_k} + \frac{T}{\rho\,(p + p_\infty)} \frac{\partial p}{\partial x_i} - \frac{T}{\rho^2} \frac{\partial \rho}{\partial x_i} = -\frac{H_i}{\theta_2(\tau_2)} \tag{B.16e}$$

Thus, taking $M_1, M_2, M_3, \boldsymbol{S_p}$ from Chapter C:

$$\frac{\partial \boldsymbol{P}}{\partial t} + M_1 \frac{\partial \boldsymbol{P}}{\partial x_1} + M_2 \frac{\partial \boldsymbol{P}}{\partial x_2} + M_3 \frac{\partial \boldsymbol{P}}{\partial x_3} = \boldsymbol{S_p}\,(\boldsymbol{P}) \tag{B.17}$$

Appendix C

Explicit Forms of System Matrices

The following quantities are defined for brevity's sake, using the definition of ψ from Section 1.3:

$$\Psi_{ij} = \rho v_i v_j - \sigma_{ij} \tag{C.1a}$$

$$\Phi_{ij}^k = \rho v_k \psi_{ij} - v_m \frac{\partial \sigma_{mk}}{\partial A_{ij}} \tag{C.1b}$$

$$\Omega_i = v_i \left(E - E_1 \right) - \frac{\sigma_{im} v_m + q_i}{\rho} \tag{C.1c}$$

$$\Gamma = \gamma - 1 \tag{C.1d}$$

$$\Upsilon = \Gamma \left(\|\boldsymbol{v}\|^2 + \alpha^2 \|\boldsymbol{J}\|^2 + E_1 - E \right) \tag{C.1e}$$

$\frac{\partial \boldsymbol{F_i}}{\partial \boldsymbol{P}}, \frac{\partial \boldsymbol{Q}}{\partial \boldsymbol{P}}$ are derived using (A.1), (A.2), (A.3), (A.4). $\frac{\partial \boldsymbol{P}}{\partial \boldsymbol{Q}}$ is derived as the inverse of $\frac{\partial \boldsymbol{Q}}{\partial \boldsymbol{P}}$.

$$\boldsymbol{F_1} = \begin{pmatrix} \rho v_1 \\ \rho v_1 E + v_1 p - v_m \sigma_{m1} + q_1 \\ \rho v_1^2 + p - \sigma_{11} \\ \rho v_1 v_2 - \sigma_{21} \\ \rho v_1 v_3 - \sigma_{31} \\ A_{1m} v_m \\ A_{2m} v_m \\ A_{3m} v_m \\ 0 \\ 0 \\ 0 \\ 0 \\ 0 \\ 0 \\ \rho J_1 v_1 + T \\ \rho J_2 v_1 \\ \rho J_3 v_1 \end{pmatrix}$$

$$\boldsymbol{F_2} = \begin{pmatrix} \rho v_2 \\ \rho v_2 E + v_2 p - v_m \sigma_{m2} + q_2 \\ \rho v_1 v_2 - \sigma_{12} \\ \rho v_2^2 + p - \sigma_{22} \\ \rho v_2 v_3 - \sigma_{32} \\ 0 \\ 0 \\ 0 \\ A_{1m} v_m \\ A_{2m} v_m \\ A_{3m} v_m \\ 0 \\ 0 \\ 0 \\ \rho J_1 v_2 \\ \rho J_2 v_2 + T \\ \rho J_3 v_2 \end{pmatrix}$$

$$\boldsymbol{F_3} = \begin{pmatrix} \rho v_3 \\ \rho v_3 E + v_3 p - v_m \sigma_{m3} + q_3 \\ \rho v_1 v_3 - \sigma_{13} \\ \rho v_2 v_3 - \sigma_{23} \\ \rho v_3^2 + p - \sigma_{33} \\ 0 \\ 0 \\ 0 \\ 0 \\ 0 \\ 0 \\ A_{1m} v_m \\ A_{2m} v_m \\ A_{3m} v_m \\ \rho J_1 v_3 \\ \rho J_2 v_3 \\ \rho J_3 v_3 + T \end{pmatrix}$$

$$\frac{\partial \boldsymbol{F_1}}{\partial \boldsymbol{P}} =$$

$$
\begin{pmatrix}
v_1 & 0 & \rho & 0 & 0 & 0 & 0 & 0 & 0 & 0 & 0 & 0 & 0 & 0 & 0 & 0 & 0 \\[4pt]
\Omega_1 & \left(\frac{\gamma v_1}{\Gamma}+\frac{q_1}{p+p\infty}\right) & (\Psi_{11}+\rho E+p) & \Psi_{12} & \Psi_{13} & \Phi^1_{11} & \Phi^1_{21} & \Phi^1_{31} & \Phi^1_{12} & \Phi^1_{22} & \Phi^1_{32} & \Phi^1_{13} & \Phi^1_{23} & \Phi^1_{33} & \alpha^2(\rho v_1 J_1+T) & \alpha^2\rho v_1 J_2 & \alpha^2\rho v_1 J_3 \\[4pt]
\frac{\Psi_{11}}{\rho} & 1 & 2\rho v_1 & 0 & 0 & -\frac{\sigma_{11}}{A_{11}} & -\frac{\sigma_{11}}{A_{21}} & -\frac{\sigma_{11}}{A_{31}} & -\frac{\sigma_{11}}{A_{12}} & -\frac{\sigma_{11}}{A_{22}} & -\frac{\sigma_{11}}{A_{32}} & -\frac{\sigma_{11}}{A_{13}} & -\frac{\sigma_{11}}{A_{23}} & -\frac{\sigma_{11}}{A_{33}} & 0 & 0 & 0 \\[4pt]
\frac{\Psi_{12}}{\rho} & 0 & \rho v_2 & \rho v_1 & 0 & -\frac{\sigma_{21}}{A_{11}} & -\frac{\sigma_{21}}{A_{21}} & -\frac{\sigma_{21}}{A_{31}} & -\frac{\sigma_{21}}{A_{12}} & -\frac{\sigma_{21}}{A_{22}} & -\frac{\sigma_{21}}{A_{32}} & -\frac{\sigma_{21}}{A_{13}} & -\frac{\sigma_{21}}{A_{23}} & -\frac{\sigma_{21}}{A_{33}} & 0 & 0 & 0 \\[4pt]
\frac{\Psi_{13}}{\rho} & 0 & \rho v_3 & 0 & \rho v_1 & -\frac{\sigma_{31}}{A_{11}} & -\frac{\sigma_{31}}{A_{21}} & -\frac{\sigma_{31}}{A_{31}} & -\frac{\sigma_{31}}{A_{12}} & -\frac{\sigma_{31}}{A_{22}} & -\frac{\sigma_{31}}{A_{32}} & -\frac{\sigma_{31}}{A_{13}} & -\frac{\sigma_{31}}{A_{23}} & -\frac{\sigma_{31}}{A_{33}} & 0 & 0 & 0 \\[4pt]
0 & 0 & A_{11} & A_{12} & A_{13} & v_1 & 0 & 0 & v_2 & 0 & 0 & v_3 & 0 & 0 & 0 & 0 & 0 \\[2pt]
0 & 0 & A_{21} & A_{22} & A_{23} & 0 & v_1 & 0 & 0 & v_2 & 0 & 0 & v_3 & 0 & 0 & 0 & 0 \\[2pt]
0 & 0 & A_{31} & A_{32} & A_{33} & 0 & 0 & v_1 & 0 & 0 & v_2 & 0 & 0 & v_3 & 0 & 0 & 0 \\[2pt]
0 & 0 & 0 & 0 & 0 & 0 & 0 & 0 & 0 & 0 & 0 & 0 & 0 & 0 & 0 & 0 & 0 \\[2pt]
0 & 0 & 0 & 0 & 0 & 0 & 0 & 0 & 0 & 0 & 0 & 0 & 0 & 0 & 0 & 0 & 0 \\[2pt]
0 & 0 & 0 & 0 & 0 & 0 & 0 & 0 & 0 & 0 & 0 & 0 & 0 & 0 & 0 & 0 & 0 \\[2pt]
0 & 0 & 0 & 0 & 0 & 0 & 0 & 0 & 0 & 0 & 0 & 0 & 0 & 0 & 0 & 0 & 0 \\[2pt]
0 & 0 & 0 & 0 & 0 & 0 & 0 & 0 & 0 & 0 & 0 & 0 & 0 & 0 & 0 & 0 & 0 \\[4pt]
v_1 J_1 - \frac{T}{\rho} & \frac{T}{p+p\infty} & \rho J_1 & 0 & 0 & 0 & 0 & 0 & 0 & 0 & 0 & 0 & 0 & 0 & \rho v_1 & 0 & 0 \\[4pt]
v_1 J_2 & 0 & \rho J_2 & 0 & 0 & 0 & 0 & 0 & 0 & 0 & 0 & 0 & 0 & 0 & 0 & \rho v_1 & 0 \\[4pt]
v_1 J_3 & 0 & \rho J_3 & 0 & 0 & 0 & 0 & 0 & 0 & 0 & 0 & 0 & 0 & 0 & 0 & 0 & \rho v_1
\end{pmatrix}
$$

$$\frac{\partial \boldsymbol{F_2}}{\partial \boldsymbol{P}} =$$

$$
\begin{pmatrix}
v_2 & 0 & 0 & \rho & 0 & 0 & 0 & 0 & 0 & 0 & 0 & 0 & 0 & 0 & 0 & 0 & 0 \\[4pt]
\Omega_2 & \left(\frac{\gamma v_2}{\Gamma}+\frac{q_2}{p+p_\infty}\right) & \Psi_{21} & \left(\Psi_{22}+\rho E+p\right) & \Psi_{23} & \Phi^2_{11} & \Phi^2_{21} & \Phi^2_{31} & \Phi^2_{12} & \Phi^2_{22} & \Phi^2_{32} & \Phi^2_{13} & \Phi^2_{23} & \Phi^2_{33} & \alpha^2\rho v_2 J_1 & \alpha^2\left(\rho v_2 J_2+T\right) & \alpha^2\rho v_2 J_3 \\[4pt]
\frac{\Psi_{21}}{\rho} & 0 & \rho v_2 & \rho v_1 & 0 & -\frac{\sigma_{12}}{A_{11}} & -\frac{\sigma_{12}}{A_{21}} & -\frac{\sigma_{12}}{A_{31}} & -\frac{\sigma_{12}}{A_{12}} & -\frac{\sigma_{12}}{A_{22}} & -\frac{\sigma_{12}}{A_{32}} & -\frac{\sigma_{12}}{A_{13}} & -\frac{\sigma_{12}}{A_{23}} & -\frac{\sigma_{12}}{A_{33}} & 0 & 0 & 0 \\[4pt]
\frac{\Psi_{22}}{\rho} & 1 & 0 & 2\rho v_2 & 0 & -\frac{\sigma_{22}}{A_{11}} & -\frac{\sigma_{22}}{A_{21}} & -\frac{\sigma_{22}}{A_{31}} & -\frac{\sigma_{22}}{A_{12}} & -\frac{\sigma_{22}}{A_{22}} & -\frac{\sigma_{22}}{A_{32}} & -\frac{\sigma_{22}}{A_{13}} & -\frac{\sigma_{22}}{A_{23}} & -\frac{\sigma_{22}}{A_{33}} & 0 & 0 & 0 \\[4pt]
\frac{\Psi_{23}}{\rho} & 0 & 0 & \rho v_3 & \rho v_2 & -\frac{\sigma_{32}}{A_{11}} & -\frac{\sigma_{32}}{A_{21}} & -\frac{\sigma_{32}}{A_{31}} & -\frac{\sigma_{32}}{A_{12}} & -\frac{\sigma_{32}}{A_{22}} & -\frac{\sigma_{32}}{A_{32}} & -\frac{\sigma_{32}}{A_{13}} & -\frac{\sigma_{32}}{A_{23}} & -\frac{\sigma_{32}}{A_{33}} & 0 & 0 & 0 \\[4pt]
0 & 0 & 0 & 0 & 0 & v_1 & 0 & 0 & 0 & 0 & 0 & 0 & 0 & 0 & 0 & 0 & 0 \\[4pt]
0 & 0 & 0 & 0 & 0 & 0 & v_1 & 0 & 0 & 0 & 0 & 0 & 0 & 0 & 0 & 0 & 0 \\[4pt]
0 & 0 & 0 & 0 & 0 & 0 & 0 & v_1 & 0 & 0 & 0 & 0 & 0 & 0 & 0 & 0 & 0 \\[4pt]
0 & 0 & A_{11} & A_{12} & A_{13} & 0 & 0 & 0 & v_2 & 0 & 0 & 0 & 0 & 0 & 0 & 0 & 0 \\[4pt]
0 & 0 & A_{21} & A_{22} & A_{23} & 0 & 0 & 0 & 0 & v_2 & 0 & 0 & 0 & 0 & 0 & 0 & 0 \\[4pt]
0 & 0 & A_{31} & A_{32} & A_{33} & 0 & 0 & 0 & 0 & 0 & v_2 & 0 & 0 & 0 & 0 & 0 & 0 \\[4pt]
0 & 0 & 0 & 0 & 0 & 0 & 0 & 0 & 0 & 0 & 0 & v_3 & 0 & 0 & 0 & 0 & 0 \\[4pt]
0 & 0 & 0 & 0 & 0 & 0 & 0 & 0 & 0 & 0 & 0 & 0 & v_3 & 0 & 0 & 0 & 0 \\[4pt]
0 & 0 & 0 & 0 & 0 & 0 & 0 & 0 & 0 & 0 & 0 & 0 & 0 & v_3 & 0 & 0 & 0 \\[4pt]
v_2 J_1 & 0 & 0 & \rho J_1 & 0 & 0 & 0 & 0 & 0 & 0 & 0 & 0 & 0 & 0 & \rho v_2 & 0 & 0 \\[4pt]
v_2 J_2-\frac{T}{\rho} & \frac{T}{p+p_\infty} & 0 & \rho J_2 & 0 & 0 & 0 & 0 & 0 & 0 & 0 & 0 & 0 & 0 & 0 & \rho v_2 & 0 \\[4pt]
v_2 J_3 & 0 & 0 & \rho J_3 & 0 & 0 & 0 & 0 & 0 & 0 & 0 & 0 & 0 & 0 & 0 & 0 & \rho v_2
\end{pmatrix}
$$

$$
\frac{\partial \boldsymbol{F}_3}{\partial \boldsymbol{P}} =
\begin{pmatrix}
v_3 & 0 & \rho & 0 & 0 & 0 & 0 & 0 & 0 & 0 & 0 & 0 & 0 & 0 & 0 & 0 & 0 \\[4pt]
\Omega_3 & \left(\dfrac{\gamma v_3}{\Gamma} + \dfrac{q_3}{p+p_\infty}\right) & \Psi_{31} & \Psi_{32} & \left(\Psi_{33}+\rho E+p\right) & \Phi^3_{11} & \Phi^3_{21} & \Phi^3_{31} & \Phi^3_{12} & \Phi^3_{22} & \Phi^3_{32} & \Phi^3_{13} & \Phi^3_{23} & \Phi^3_{33} & \alpha^2\rho v_3 J_1 & \alpha^2\rho v_3 J_2 & \alpha^2\left(\rho v_3 J_3 + T\right) \\[4pt]
\dfrac{\Psi_{31}}{\rho} & 0 & \rho v_3 & 0 & \rho v_1 & -\dfrac{\sigma_{13}}{A_{11}} & -\dfrac{\sigma_{13}}{A_{21}} & -\dfrac{\sigma_{13}}{A_{31}} & -\dfrac{\sigma_{13}}{A_{12}} & -\dfrac{\sigma_{13}}{A_{22}} & -\dfrac{\sigma_{13}}{A_{32}} & -\dfrac{\sigma_{13}}{A_{13}} & -\dfrac{\sigma_{13}}{A_{23}} & -\dfrac{\sigma_{13}}{A_{33}} & 0 & 0 & 0 \\[4pt]
\dfrac{\Psi_{32}}{\rho} & 0 & 0 & \rho v_3 & \rho v_2 & -\dfrac{\sigma_{23}}{A_{11}} & -\dfrac{\sigma_{23}}{A_{21}} & -\dfrac{\sigma_{23}}{A_{31}} & -\dfrac{\sigma_{23}}{A_{12}} & -\dfrac{\sigma_{23}}{A_{22}} & -\dfrac{\sigma_{23}}{A_{32}} & -\dfrac{\sigma_{23}}{A_{13}} & -\dfrac{\sigma_{23}}{A_{23}} & -\dfrac{\sigma_{23}}{A_{33}} & 0 & 0 & 0 \\[4pt]
\dfrac{\Psi_{33}}{\rho} & 1 & 0 & 0 & 2\rho v_3 & -\dfrac{\sigma_{33}}{A_{11}} & -\dfrac{\sigma_{33}}{A_{21}} & -\dfrac{\sigma_{33}}{A_{31}} & -\dfrac{\sigma_{33}}{A_{12}} & -\dfrac{\sigma_{33}}{A_{22}} & -\dfrac{\sigma_{33}}{A_{32}} & -\dfrac{\sigma_{33}}{A_{13}} & -\dfrac{\sigma_{33}}{A_{23}} & -\dfrac{\sigma_{33}}{A_{33}} & 0 & 0 & 0 \\[4pt]
0 & 0 & 0 & 0 & 0 & 0 & 0 & 0 & 0 & 0 & 0 & 0 & 0 & 0 & 0 & 0 & 0 \\
0 & 0 & 0 & 0 & 0 & 0 & 0 & 0 & 0 & 0 & 0 & 0 & 0 & 0 & 0 & 0 & 0 \\
0 & 0 & 0 & 0 & 0 & 0 & 0 & 0 & 0 & 0 & 0 & 0 & 0 & 0 & 0 & 0 & 0 \\
0 & 0 & 0 & 0 & 0 & 0 & 0 & 0 & 0 & 0 & 0 & 0 & 0 & 0 & 0 & 0 & 0 \\
0 & 0 & 0 & 0 & 0 & 0 & 0 & 0 & 0 & 0 & 0 & 0 & 0 & 0 & 0 & 0 & 0 \\
0 & 0 & 0 & 0 & 0 & v_1 & 0 & 0 & v_2 & 0 & 0 & v_3 & 0 & 0 & 0 & 0 & 0 \\
0 & 0 & A_{11} & A_{12} & A_{13} & 0 & v_1 & 0 & 0 & v_2 & 0 & 0 & v_3 & 0 & 0 & 0 & 0 \\
0 & 0 & A_{21} & A_{22} & A_{23} & 0 & 0 & v_1 & 0 & 0 & v_2 & 0 & 0 & v_3 & 0 & 0 & 0 \\
0 & 0 & A_{31} & A_{32} & A_{33} & 0 & 0 & 0 & 0 & 0 & 0 & 0 & 0 & 0 & 0 & 0 & 0 \\
v_3 J_1 & 0 & 0 & 0 & \rho J_1 & 0 & 0 & 0 & 0 & 0 & 0 & 0 & 0 & 0 & \rho v_3 & 0 & 0 \\
v_3 J_2 & 0 & 0 & 0 & \rho J_2 & 0 & 0 & 0 & 0 & 0 & 0 & 0 & 0 & 0 & 0 & \rho v_3 & 0 \\
v_3 J_3 - \dfrac{T}{\rho} & \dfrac{T}{p+p_\infty} & 0 & 0 & \rho J_3 & 0 & 0 & 0 & 0 & 0 & 0 & 0 & 0 & 0 & 0 & 0 & \rho v_3
\end{pmatrix}
$$

$$B_2 = \begin{pmatrix} 0 & 0 & 0 & 0 & 0 & 0 & 0 & 0 & 0 & 0 & 0 & 0 & 0 & 0 & 0 & 0 & 0 \\ 0 & 0 & 0 & 0 & 0 & 0 & 0 & 0 & 0 & 0 & 0 & 0 & 0 & 0 & 0 & 0 & 0 \\ 0 & 0 & 0 & 0 & 0 & 0 & 0 & 0 & 0 & 0 & 0 & 0 & 0 & 0 & 0 & 0 & 0 \\ 0 & 0 & 0 & 0 & 0 & 0 & 0 & 0 & 0 & 0 & 0 & 0 & 0 & 0 & 0 & 0 & 0 \\ 0 & 0 & 0 & 0 & 0 & 0 & 0 & 0 & 0 & 0 & 0 & 0 & 0 & 0 & 0 & 0 & 0 \\ 0 & 0 & 0 & 0 & 0 & v_2 & 0 & 0 & -v_1 & 0 & 0 & 0 & 0 & 0 & 0 & 0 & 0 \\ 0 & 0 & 0 & 0 & 0 & 0 & v_2 & 0 & 0 & -v_1 & 0 & 0 & 0 & 0 & 0 & 0 & 0 \\ 0 & 0 & 0 & 0 & 0 & 0 & 0 & v_2 & 0 & 0 & -v_1 & 0 & 0 & 0 & 0 & 0 & 0 \\ 0 & 0 & 0 & 0 & 0 & 0 & 0 & 0 & -v_3 & 0 & 0 & v_2 & 0 & 0 & 0 & 0 & 0 \\ 0 & 0 & 0 & 0 & 0 & 0 & 0 & 0 & 0 & -v_3 & 0 & 0 & v_2 & 0 & 0 & 0 & 0 \\ 0 & 0 & 0 & 0 & 0 & 0 & 0 & 0 & 0 & 0 & -v_3 & 0 & 0 & v_2 & 0 & 0 & 0 \\ 0 & 0 & 0 & 0 & 0 & 0 & 0 & 0 & 0 & 0 & 0 & 0 & 0 & 0 & 0 & 0 & 0 \\ 0 & 0 & 0 & 0 & 0 & 0 & 0 & 0 & 0 & 0 & 0 & 0 & 0 & 0 & 0 & 0 & 0 \\ 0 & 0 & 0 & 0 & 0 & 0 & 0 & 0 & 0 & 0 & 0 & 0 & 0 & 0 & 0 & 0 & 0 \\ 0 & 0 & 0 & 0 & 0 & 0 & 0 & 0 & 0 & 0 & 0 & 0 & 0 & 0 & 0 & 0 & 0 \\ 0 & 0 & 0 & 0 & 0 & 0 & 0 & 0 & 0 & 0 & 0 & 0 & 0 & 0 & 0 & 0 & 0 \\ 0 & 0 & 0 & 0 & 0 & 0 & 0 & 0 & 0 & 0 & 0 & 0 & 0 & 0 & 0 & 0 & 0 \end{pmatrix}$$

$$B_1 = \begin{pmatrix} 0 & 0 & 0 & 0 & 0 & 0 & 0 & 0 & 0 & 0 & 0 & 0 & 0 & 0 & 0 & 0 & 0 \\ 0 & 0 & 0 & 0 & 0 & 0 & 0 & 0 & 0 & 0 & 0 & 0 & 0 & 0 & 0 & 0 & 0 \\ 0 & 0 & 0 & 0 & 0 & 0 & 0 & 0 & 0 & 0 & 0 & 0 & 0 & 0 & 0 & 0 & 0 \\ 0 & 0 & 0 & 0 & 0 & 0 & 0 & 0 & 0 & 0 & 0 & 0 & 0 & 0 & 0 & 0 & 0 \\ 0 & 0 & 0 & 0 & 0 & 0 & 0 & 0 & 0 & 0 & 0 & 0 & 0 & 0 & 0 & 0 & 0 \\ 0 & 0 & 0 & 0 & 0 & -v_2 & 0 & 0 & v_1 & 0 & 0 & 0 & 0 & 0 & 0 & 0 & 0 \\ 0 & 0 & 0 & 0 & 0 & 0 & -v_2 & 0 & 0 & v_1 & 0 & 0 & 0 & 0 & 0 & 0 & 0 \\ 0 & 0 & 0 & 0 & 0 & 0 & 0 & -v_2 & 0 & 0 & v_1 & 0 & 0 & 0 & 0 & 0 & 0 \\ 0 & 0 & 0 & 0 & 0 & -v_3 & 0 & 0 & 0 & 0 & 0 & v_1 & 0 & 0 & 0 & 0 & 0 \\ 0 & 0 & 0 & 0 & 0 & 0 & -v_3 & 0 & 0 & 0 & 0 & 0 & v_1 & 0 & 0 & 0 & 0 \\ 0 & 0 & 0 & 0 & 0 & 0 & 0 & -v_3 & 0 & 0 & 0 & 0 & 0 & v_1 & 0 & 0 & 0 \\ 0 & 0 & 0 & 0 & 0 & 0 & 0 & 0 & 0 & 0 & 0 & 0 & 0 & 0 & 0 & 0 & 0 \\ 0 & 0 & 0 & 0 & 0 & 0 & 0 & 0 & 0 & 0 & 0 & 0 & 0 & 0 & 0 & 0 & 0 \\ 0 & 0 & 0 & 0 & 0 & 0 & 0 & 0 & 0 & 0 & 0 & 0 & 0 & 0 & 0 & 0 & 0 \\ 0 & 0 & 0 & 0 & 0 & 0 & 0 & 0 & 0 & 0 & 0 & 0 & 0 & 0 & 0 & 0 & 0 \\ 0 & 0 & 0 & 0 & 0 & 0 & 0 & 0 & 0 & 0 & 0 & 0 & 0 & 0 & 0 & 0 & 0 \\ 0 & 0 & 0 & 0 & 0 & 0 & 0 & 0 & 0 & 0 & 0 & 0 & 0 & 0 & 0 & 0 & 0 \end{pmatrix}$$

$$B_3 = \begin{pmatrix}
0 & 0 & 0 & 0 & 0 & 0 & 0 & 0 & 0 & 0 & 0 & 0 & 0 & 0 & 0 & 0 & 0 \\
0 & 0 & 0 & 0 & 0 & 0 & 0 & 0 & 0 & 0 & 0 & 0 & 0 & 0 & 0 & 0 & 0 \\
0 & 0 & 0 & 0 & 0 & 0 & 0 & 0 & 0 & 0 & 0 & 0 & 0 & 0 & 0 & 0 & 0 \\
0 & 0 & 0 & 0 & 0 & 0 & 0 & 0 & 0 & 0 & 0 & 0 & 0 & 0 & 0 & 0 & 0 \\
0 & 0 & 0 & 0 & 0 & 0 & 0 & 0 & 0 & 0 & 0 & 0 & 0 & 0 & 0 & 0 & 0 \\
0 & 0 & 0 & 0 & 0 & v_3 & 0 & 0 & 0 & 0 & 0 & -v_1 & 0 & 0 & 0 & 0 & 0 \\
0 & 0 & 0 & 0 & 0 & 0 & v_3 & 0 & 0 & 0 & 0 & 0 & -v_1 & 0 & 0 & 0 & 0 \\
0 & 0 & 0 & 0 & 0 & 0 & 0 & v_3 & 0 & 0 & 0 & 0 & 0 & -v_1 & 0 & 0 & 0 \\
0 & 0 & 0 & 0 & 0 & 0 & 0 & 0 & v_3 & 0 & 0 & -v_2 & 0 & 0 & 0 & 0 & 0 \\
0 & 0 & 0 & 0 & 0 & 0 & 0 & 0 & 0 & v_3 & 0 & 0 & -v_2 & 0 & 0 & 0 & 0 \\
0 & 0 & 0 & 0 & 0 & 0 & 0 & 0 & 0 & 0 & v_3 & 0 & 0 & -v_2 & 0 & 0 & 0 \\
0 & 0 & 0 & 0 & 0 & 0 & 0 & 0 & 0 & 0 & 0 & 0 & 0 & 0 & 0 & 0 & 0 \\
0 & 0 & 0 & 0 & 0 & 0 & 0 & 0 & 0 & 0 & 0 & 0 & 0 & 0 & 0 & 0 & 0 \\
0 & 0 & 0 & 0 & 0 & 0 & 0 & 0 & 0 & 0 & 0 & 0 & 0 & 0 & 0 & 0 & 0 \\
0 & 0 & 0 & 0 & 0 & 0 & 0 & 0 & 0 & 0 & 0 & 0 & 0 & 0 & 0 & 0 & 0 \\
0 & 0 & 0 & 0 & 0 & 0 & 0 & 0 & 0 & 0 & 0 & 0 & 0 & 0 & 0 & 0 & 0 \\
0 & 0 & 0 & 0 & 0 & 0 & 0 & 0 & 0 & 0 & 0 & 0 & 0 & 0 & 0 & 0 & 0
\end{pmatrix}$$

$$S = \frac{1}{\theta_1(\tau_1)}\begin{pmatrix} 0 \\ 0 \\ 0 \\ 0 \\ 0 \\ -\psi_{11} \\ -\psi_{21} \\ -\psi_{31} \\ -\psi_{12} \\ -\psi_{22} \\ -\psi_{32} \\ -\psi_{13} \\ -\psi_{23} \\ -\psi_{33} \\ 0 \\ 0 \\ 0 \end{pmatrix} + \frac{1}{\theta_2(\tau_2)}\begin{pmatrix} 0 \\ 0 \\ 0 \\ 0 \\ 0 \\ 0 \\ 0 \\ 0 \\ 0 \\ 0 \\ 0 \\ 0 \\ 0 \\ 0 \\ -\rho H_1 \\ -\rho H_2 \\ -\rho H_3 \end{pmatrix}$$

$$
\frac{\partial \boldsymbol{Q}}{\partial \boldsymbol{P}} =
\begin{pmatrix}
1 & 0 & 0 & 0 & 0 & 0 & 0 & 0 & 0 & 0 & 0 & 0 & 0 & 0 & 0 & 0 & 0 \\
E-E_1 & \frac{1}{\Gamma} & \rho v_1 & \rho v_2 & \rho v_3 & \rho\psi_{11} & \rho\psi_{21} & \rho\psi_{31} & \rho\psi_{12} & \rho\psi_{22} & \rho\psi_{32} & \rho\psi_{13} & \rho\psi_{23} & \rho\psi_{33} & \alpha^2\rho J_1 & \alpha^2\rho J_2 & \alpha^2\rho J_3 \\
v_1 & 0 & \rho & 0 & 0 & 0 & 0 & 0 & 0 & 0 & 0 & 0 & 0 & 0 & 0 & 0 & 0 \\
v_2 & 0 & 0 & \rho & 0 & 0 & 0 & 0 & 0 & 0 & 0 & 0 & 0 & 0 & 0 & 0 & 0 \\
v_3 & 0 & 0 & 0 & \rho & 0 & 0 & 0 & 0 & 0 & 0 & 0 & 0 & 0 & 0 & 0 & 0 \\
0 & 0 & 0 & 0 & 0 & 1 & 0 & 0 & 0 & 0 & 0 & 0 & 0 & 0 & 0 & 0 & 0 \\
0 & 0 & 0 & 0 & 0 & 0 & 1 & 0 & 0 & 0 & 0 & 0 & 0 & 0 & 0 & 0 & 0 \\
0 & 0 & 0 & 0 & 0 & 0 & 0 & 1 & 0 & 0 & 0 & 0 & 0 & 0 & 0 & 0 & 0 \\
0 & 0 & 0 & 0 & 0 & 0 & 0 & 0 & 1 & 0 & 0 & 0 & 0 & 0 & 0 & 0 & 0 \\
0 & 0 & 0 & 0 & 0 & 0 & 0 & 0 & 0 & 1 & 0 & 0 & 0 & 0 & 0 & 0 & 0 \\
0 & 0 & 0 & 0 & 0 & 0 & 0 & 0 & 0 & 0 & 1 & 0 & 0 & 0 & 0 & 0 & 0 \\
0 & 0 & 0 & 0 & 0 & 0 & 0 & 0 & 0 & 0 & 0 & 1 & 0 & 0 & 0 & 0 & 0 \\
0 & 0 & 0 & 0 & 0 & 0 & 0 & 0 & 0 & 0 & 0 & 0 & 1 & 0 & 0 & 0 & 0 \\
0 & 0 & 0 & 0 & 0 & 0 & 0 & 0 & 0 & 0 & 0 & 0 & 0 & 1 & 0 & 0 & 0 \\
J_1 & 0 & 0 & 0 & 0 & 0 & 0 & 0 & 0 & 0 & 0 & 0 & 0 & 0 & \rho & 0 & 0 \\
J_2 & 0 & 0 & 0 & 0 & 0 & 0 & 0 & 0 & 0 & 0 & 0 & 0 & 0 & 0 & \rho & 0 \\
J_3 & 0 & 0 & 0 & 0 & 0 & 0 & 0 & 0 & 0 & 0 & 0 & 0 & 0 & 0 & 0 & \rho
\end{pmatrix}
$$

$$\frac{\partial \mathbf{P}}{\partial \mathbf{Q}} =
\begin{pmatrix}
1 & 0 & 0 & 0 & 0 & 0 & 0 & 0 & 0 & 0 & 0 & 0 & 0 & 0 & 0 & 0 & 0 \\
\Upsilon & \Gamma & -\Gamma v_1 & -\Gamma v_2 & -\Gamma v_3 & -\Gamma\rho\psi_{11} & -\Gamma\rho\psi_{21} & -\Gamma\rho\psi_{31} & -\Gamma\rho\psi_{12} & -\Gamma\rho\psi_{22} & -\Gamma\rho\psi_{32} & -\Gamma\rho\psi_{13} & -\Gamma\rho\psi_{23} & -\Gamma\rho\psi_{33} & -\Gamma\alpha^2 J_1 & -\Gamma\alpha^2 J_2 & -\Gamma\alpha^2 J_3 \\
-\frac{v_1}{\rho} & 0 & \frac{1}{\rho} & 0 & 0 & 0 & 0 & 0 & 0 & 0 & 0 & 0 & 0 & 0 & 0 & 0 & 0 \\
-\frac{v_2}{\rho} & 0 & 0 & \frac{1}{\rho} & 0 & 0 & 0 & 0 & 0 & 0 & 0 & 0 & 0 & 0 & 0 & 0 & 0 \\
-\frac{v_3}{\rho} & 0 & 0 & 0 & \frac{1}{\rho} & 0 & 0 & 0 & 0 & 0 & 0 & 0 & 0 & 0 & 0 & 0 & 0 \\
0 & 0 & 0 & 0 & 0 & 1 & 0 & 0 & 0 & 0 & 0 & 0 & 0 & 0 & 0 & 0 & 0 \\
0 & 0 & 0 & 0 & 0 & 0 & 1 & 0 & 0 & 0 & 0 & 0 & 0 & 0 & 0 & 0 & 0 \\
0 & 0 & 0 & 0 & 0 & 0 & 0 & 1 & 0 & 0 & 0 & 0 & 0 & 0 & 0 & 0 & 0 \\
0 & 0 & 0 & 0 & 0 & 0 & 0 & 0 & 1 & 0 & 0 & 0 & 0 & 0 & 0 & 0 & 0 \\
0 & 0 & 0 & 0 & 0 & 0 & 0 & 0 & 0 & 1 & 0 & 0 & 0 & 0 & 0 & 0 & 0 \\
0 & 0 & 0 & 0 & 0 & 0 & 0 & 0 & 0 & 0 & 1 & 0 & 0 & 0 & 0 & 0 & 0 \\
0 & 0 & 0 & 0 & 0 & 0 & 0 & 0 & 0 & 0 & 0 & 1 & 0 & 0 & 0 & 0 & 0 \\
0 & 0 & 0 & 0 & 0 & 0 & 0 & 0 & 0 & 0 & 0 & 0 & 1 & 0 & 0 & 0 & 0 \\
0 & 0 & 0 & 0 & 0 & 0 & 0 & 0 & 0 & 0 & 0 & 0 & 0 & 1 & 0 & 0 & 0 \\
-\frac{J_1}{\rho} & 0 & 0 & 0 & 0 & 0 & 0 & 0 & 0 & 0 & 0 & 0 & 0 & 0 & \frac{1}{\rho} & 0 & 0 \\
-\frac{J_2}{\rho} & 0 & 0 & 0 & 0 & 0 & 0 & 0 & 0 & 0 & 0 & 0 & 0 & 0 & 0 & \frac{1}{\rho} & 0 \\
-\frac{J_3}{\rho} & 0 & 0 & 0 & 0 & 0 & 0 & 0 & 0 & 0 & 0 & 0 & 0 & 0 & 0 & 0 & \frac{1}{\rho}
\end{pmatrix}$$

$$
M_1 = \begin{pmatrix}
v_1 & 0 & 0 & 0 & 0 & 0 & 0 & 0 & 0 & 0 & 0 & \rho & 0 & 0 & 0 & 0 & 0 \\[2pt]
0 & v_1 & 0 & 0 & 0 & 0 & 0 & 0 & 0 & 0 & 0 & \gamma p & 0 & \Gamma\alpha^2 T & 0 & 0 & 0 \\[2pt]
0 & 0 & v_1 & 0 & 0 & 0 & 0 & 0 & 0 & 0 & 0 & A_{11} & A_{12} & A_{13} & 0 & 0 & 0 \\[2pt]
0 & 0 & 0 & v_1 & 0 & 0 & 0 & 0 & 0 & 0 & 0 & A_{21} & A_{22} & A_{23} & 0 & 0 & 0 \\[2pt]
0 & 0 & 0 & 0 & v_1 & 0 & 0 & 0 & 0 & 0 & 0 & A_{31} & A_{32} & A_{33} & 0 & 0 & 0 \\[2pt]
0 & 0 & 0 & 0 & 0 & v_1 & 0 & 0 & 0 & 0 & 0 & 0 & 0 & 0 & 0 & 0 & 0 \\[2pt]
0 & 0 & 0 & 0 & 0 & 0 & v_1 & 0 & 0 & 0 & 0 & 0 & 0 & 0 & 0 & 0 & 0 \\[2pt]
0 & 0 & 0 & 0 & 0 & 0 & 0 & v_1 & 0 & 0 & 0 & 0 & 0 & 0 & 0 & 0 & 0 \\[2pt]
0 & 0 & 0 & 0 & 0 & 0 & 0 & 0 & v_1 & 0 & 0 & 0 & 0 & 0 & 0 & 0 & 0 \\[2pt]
0 & 0 & 0 & 0 & 0 & 0 & 0 & 0 & 0 & v_1 & 0 & 0 & 0 & 0 & 0 & 0 & 0 \\[2pt]
0 & 0 & 0 & 0 & 0 & 0 & 0 & 0 & 0 & 0 & v_1 & 0 & 0 & 0 & 0 & 0 & 0 \\[4pt]
-\dfrac{\sigma_{11}}{\rho^2} & \dfrac{1}{\rho} & -\dfrac{1}{\rho}\dfrac{\partial\sigma_{11}}{\partial A_{11}} & -\dfrac{1}{\rho}\dfrac{\partial\sigma_{11}}{\partial A_{21}} & -\dfrac{1}{\rho}\dfrac{\partial\sigma_{11}}{\partial A_{31}} & -\dfrac{1}{\rho}\dfrac{\partial\sigma_{11}}{\partial A_{12}} & -\dfrac{1}{\rho}\dfrac{\partial\sigma_{11}}{\partial A_{22}} & -\dfrac{1}{\rho}\dfrac{\partial\sigma_{11}}{\partial A_{32}} & -\dfrac{1}{\rho}\dfrac{\partial\sigma_{11}}{\partial A_{13}} & -\dfrac{1}{\rho}\dfrac{\partial\sigma_{11}}{\partial A_{23}} & -\dfrac{1}{\rho}\dfrac{\partial\sigma_{11}}{\partial A_{33}} & v_1 & 0 & 0 & 0 & 0 & 0 \\[8pt]
-\dfrac{\sigma_{21}}{\rho^2} & 0 & -\dfrac{1}{\rho}\dfrac{\partial\sigma_{21}}{\partial A_{11}} & -\dfrac{1}{\rho}\dfrac{\partial\sigma_{21}}{\partial A_{21}} & -\dfrac{1}{\rho}\dfrac{\partial\sigma_{21}}{\partial A_{31}} & -\dfrac{1}{\rho}\dfrac{\partial\sigma_{21}}{\partial A_{12}} & -\dfrac{1}{\rho}\dfrac{\partial\sigma_{21}}{\partial A_{22}} & -\dfrac{1}{\rho}\dfrac{\partial\sigma_{21}}{\partial A_{32}} & -\dfrac{1}{\rho}\dfrac{\partial\sigma_{21}}{\partial A_{13}} & -\dfrac{1}{\rho}\dfrac{\partial\sigma_{21}}{\partial A_{23}} & -\dfrac{1}{\rho}\dfrac{\partial\sigma_{21}}{\partial A_{33}} & 0 & v_1 & 0 & 0 & 0 & 0 \\[8pt]
-\dfrac{\sigma_{31}}{\rho^2} & 0 & -\dfrac{1}{\rho}\dfrac{\partial\sigma_{31}}{\partial A_{11}} & -\dfrac{1}{\rho}\dfrac{\partial\sigma_{31}}{\partial A_{21}} & -\dfrac{1}{\rho}\dfrac{\partial\sigma_{31}}{\partial A_{31}} & -\dfrac{1}{\rho}\dfrac{\partial\sigma_{31}}{\partial A_{12}} & -\dfrac{1}{\rho}\dfrac{\partial\sigma_{31}}{\partial A_{22}} & -\dfrac{1}{\rho}\dfrac{\partial\sigma_{31}}{\partial A_{32}} & -\dfrac{1}{\rho}\dfrac{\partial\sigma_{31}}{\partial A_{13}} & -\dfrac{1}{\rho}\dfrac{\partial\sigma_{31}}{\partial A_{23}} & -\dfrac{1}{\rho}\dfrac{\partial\sigma_{31}}{\partial A_{33}} & 0 & 0 & v_1 & 0 & 0 & 0 \\[8pt]
-\dfrac{T}{\rho^2} & \dfrac{T}{\rho(p+p_\infty)} & 0 & 0 & 0 & 0 & 0 & 0 & 0 & 0 & 0 & 0 & 0 & 0 & v_1 & 0 & 0 \\[4pt]
0 & 0 & 0 & 0 & 0 & 0 & 0 & 0 & 0 & 0 & 0 & 0 & 0 & 0 & 0 & v_1 & 0 \\[2pt]
0 & 0 & 0 & 0 & 0 & 0 & 0 & 0 & 0 & 0 & 0 & 0 & 0 & 0 & 0 & 0 & v_1
\end{pmatrix}
$$

$$
M_2 =
\begin{pmatrix}
v_2 & 0 & 0 & \rho & 0 & 0 & 0 & 0 & 0 & 0 & 0 & 0 & 0 & 0 & 0 & 0 & 0 \\[4pt]
0 & v_2 & 0 & \gamma p & 0 & 0 & 0 & 0 & 0 & 0 & 0 & 0 & 0 & 0 & 0 & \Gamma\alpha^2 T & 0 \\[4pt]
-\dfrac{\sigma_{12}}{\rho^2} & 0 & v_2 & 0 & 0 & -\dfrac{1}{\rho}\dfrac{\partial\sigma_{12}}{\partial A_{11}} & -\dfrac{1}{\rho}\dfrac{\partial\sigma_{12}}{\partial A_{21}} & -\dfrac{1}{\rho}\dfrac{\partial\sigma_{12}}{\partial A_{31}} & -\dfrac{1}{\rho}\dfrac{\partial\sigma_{12}}{\partial A_{12}} & -\dfrac{1}{\rho}\dfrac{\partial\sigma_{12}}{\partial A_{22}} & -\dfrac{1}{\rho}\dfrac{\partial\sigma_{12}}{\partial A_{32}} & -\dfrac{1}{\rho}\dfrac{\partial\sigma_{12}}{\partial A_{13}} & -\dfrac{1}{\rho}\dfrac{\partial\sigma_{12}}{\partial A_{23}} & -\dfrac{1}{\rho}\dfrac{\partial\sigma_{12}}{\partial A_{33}} & 0 & 0 & 0 \\[4pt]
-\dfrac{\sigma_{22}}{\rho^2} & \dfrac{1}{\rho} & 0 & v_2 & 0 & -\dfrac{1}{\rho}\dfrac{\partial\sigma_{22}}{\partial A_{11}} & -\dfrac{1}{\rho}\dfrac{\partial\sigma_{22}}{\partial A_{21}} & -\dfrac{1}{\rho}\dfrac{\partial\sigma_{22}}{\partial A_{31}} & -\dfrac{1}{\rho}\dfrac{\partial\sigma_{22}}{\partial A_{12}} & -\dfrac{1}{\rho}\dfrac{\partial\sigma_{22}}{\partial A_{22}} & -\dfrac{1}{\rho}\dfrac{\partial\sigma_{22}}{\partial A_{32}} & -\dfrac{1}{\rho}\dfrac{\partial\sigma_{22}}{\partial A_{13}} & -\dfrac{1}{\rho}\dfrac{\partial\sigma_{22}}{\partial A_{23}} & -\dfrac{1}{\rho}\dfrac{\partial\sigma_{22}}{\partial A_{33}} & 0 & 0 & 0 \\[4pt]
-\dfrac{\sigma_{32}}{\rho^2} & 0 & 0 & 0 & v_2 & -\dfrac{1}{\rho}\dfrac{\partial\sigma_{32}}{\partial A_{11}} & -\dfrac{1}{\rho}\dfrac{\partial\sigma_{32}}{\partial A_{21}} & -\dfrac{1}{\rho}\dfrac{\partial\sigma_{32}}{\partial A_{31}} & -\dfrac{1}{\rho}\dfrac{\partial\sigma_{32}}{\partial A_{12}} & -\dfrac{1}{\rho}\dfrac{\partial\sigma_{32}}{\partial A_{22}} & -\dfrac{1}{\rho}\dfrac{\partial\sigma_{32}}{\partial A_{32}} & -\dfrac{1}{\rho}\dfrac{\partial\sigma_{32}}{\partial A_{13}} & -\dfrac{1}{\rho}\dfrac{\partial\sigma_{32}}{\partial A_{23}} & -\dfrac{1}{\rho}\dfrac{\partial\sigma_{32}}{\partial A_{33}} & 0 & 0 & 0 \\[4pt]
0 & 0 & 0 & 0 & 0 & v_2 & 0 & 0 & 0 & 0 & 0 & 0 & 0 & 0 & 0 & 0 & 0 \\[4pt]
0 & 0 & 0 & 0 & 0 & 0 & v_2 & 0 & 0 & 0 & 0 & 0 & 0 & 0 & 0 & 0 & 0 \\[4pt]
0 & 0 & 0 & 0 & 0 & 0 & 0 & v_2 & 0 & 0 & 0 & 0 & 0 & 0 & 0 & 0 & 0 \\[4pt]
0 & 0 & A_{11} & A_{12} & A_{13} & 0 & 0 & 0 & v_2 & 0 & 0 & 0 & 0 & 0 & 0 & 0 & 0 \\[4pt]
0 & 0 & A_{21} & A_{22} & A_{23} & 0 & 0 & 0 & 0 & v_2 & 0 & 0 & 0 & 0 & 0 & 0 & 0 \\[4pt]
0 & 0 & A_{31} & A_{32} & A_{33} & 0 & 0 & 0 & 0 & 0 & v_2 & 0 & 0 & 0 & 0 & 0 & 0 \\[4pt]
0 & 0 & 0 & 0 & 0 & 0 & 0 & 0 & 0 & 0 & 0 & v_2 & 0 & 0 & 0 & 0 & 0 \\[4pt]
0 & 0 & 0 & 0 & 0 & 0 & 0 & 0 & 0 & 0 & 0 & 0 & v_2 & 0 & 0 & 0 & 0 \\[4pt]
0 & 0 & 0 & 0 & 0 & 0 & 0 & 0 & 0 & 0 & 0 & 0 & 0 & v_2 & 0 & 0 & 0 \\[4pt]
0 & 0 & 0 & 0 & 0 & 0 & 0 & 0 & 0 & 0 & 0 & 0 & 0 & 0 & v_2 & 0 & 0 \\[4pt]
-\dfrac{T}{\rho^2} & \dfrac{T}{\rho(p+p_\infty)} & 0 & 0 & 0 & 0 & 0 & 0 & 0 & 0 & 0 & 0 & 0 & 0 & 0 & v_2 & 0 \\[4pt]
0 & 0 & 0 & 0 & 0 & 0 & 0 & 0 & 0 & 0 & 0 & 0 & 0 & 0 & 0 & 0 & v_2
\end{pmatrix}
$$

$$
M_3 =
\begin{pmatrix}
v_3 & 0 & 0 & 0 & 0 & 0 & 0 & 0 & 0 & 0 & 0 & 0 & 0 & \rho & 0 & 0 & 0\\[4pt]
0 & v_3 & 0 & 0 & 0 & 0 & 0 & 0 & 0 & 0 & 0 & 0 & 0 & \gamma p & 0 & 0 & \Gamma\alpha^2 T\\[4pt]
0 & 0 & v_3 & 0 & 0 & 0 & 0 & 0 & 0 & 0 & 0 & A_{11} & A_{12} & A_{13} & 0 & 0 & 0\\[4pt]
0 & 0 & 0 & v_3 & 0 & 0 & 0 & 0 & 0 & 0 & 0 & A_{21} & A_{22} & A_{23} & 0 & 0 & 0\\[4pt]
0 & 0 & 0 & 0 & v_3 & 0 & 0 & 0 & 0 & 0 & 0 & A_{31} & A_{32} & A_{33} & 0 & 0 & 0\\[4pt]
0 & 0 & 0 & 0 & 0 & v_3 & 0 & 0 & 0 & 0 & 0 & 0 & 0 & 0 & 0 & 0 & 0\\[4pt]
0 & 0 & 0 & 0 & 0 & 0 & v_3 & 0 & 0 & 0 & 0 & 0 & 0 & 0 & 0 & 0 & 0\\[4pt]
0 & 0 & 0 & 0 & 0 & 0 & 0 & v_3 & 0 & 0 & 0 & 0 & 0 & 0 & 0 & 0 & 0\\[4pt]
0 & 0 & 0 & 0 & 0 & 0 & 0 & 0 & v_3 & 0 & 0 & 0 & 0 & 0 & 0 & 0 & 0\\[4pt]
0 & 0 & 0 & 0 & 0 & 0 & 0 & 0 & 0 & v_3 & 0 & 0 & 0 & 0 & 0 & 0 & 0\\[4pt]
0 & 0 & 0 & 0 & 0 & 0 & 0 & 0 & 0 & 0 & v_3 & 0 & 0 & 0 & 0 & 0 & 0\\[4pt]
-\dfrac{\sigma_{13}}{\rho^2} & 0 & -\dfrac{1}{\rho}\dfrac{\partial\sigma_{13}}{\partial A_{11}} & -\dfrac{1}{\rho}\dfrac{\partial\sigma_{13}}{\partial A_{21}} & -\dfrac{1}{\rho}\dfrac{\partial\sigma_{13}}{\partial A_{31}} & -\dfrac{1}{\rho}\dfrac{\partial\sigma_{13}}{\partial A_{12}} & -\dfrac{1}{\rho}\dfrac{\partial\sigma_{13}}{\partial A_{22}} & -\dfrac{1}{\rho}\dfrac{\partial\sigma_{13}}{\partial A_{32}} & -\dfrac{1}{\rho}\dfrac{\partial\sigma_{13}}{\partial A_{13}} & -\dfrac{1}{\rho}\dfrac{\partial\sigma_{13}}{\partial A_{23}} & -\dfrac{1}{\rho}\dfrac{\partial\sigma_{13}}{\partial A_{33}} & v_3 & 0 & 0 & 0 & 0 & 0\\[10pt]
-\dfrac{\sigma_{23}}{\rho^2} & 0 & -\dfrac{1}{\rho}\dfrac{\partial\sigma_{23}}{\partial A_{11}} & -\dfrac{1}{\rho}\dfrac{\partial\sigma_{23}}{\partial A_{21}} & -\dfrac{1}{\rho}\dfrac{\partial\sigma_{23}}{\partial A_{31}} & -\dfrac{1}{\rho}\dfrac{\partial\sigma_{23}}{\partial A_{12}} & -\dfrac{1}{\rho}\dfrac{\partial\sigma_{23}}{\partial A_{22}} & -\dfrac{1}{\rho}\dfrac{\partial\sigma_{23}}{\partial A_{32}} & -\dfrac{1}{\rho}\dfrac{\partial\sigma_{23}}{\partial A_{13}} & -\dfrac{1}{\rho}\dfrac{\partial\sigma_{23}}{\partial A_{23}} & -\dfrac{1}{\rho}\dfrac{\partial\sigma_{23}}{\partial A_{33}} & 0 & v_3 & 0 & 0 & 0 & 0\\[10pt]
-\dfrac{\sigma_{33}}{\rho^2} & \dfrac{1}{\rho} & -\dfrac{1}{\rho}\dfrac{\partial\sigma_{33}}{\partial A_{11}} & -\dfrac{1}{\rho}\dfrac{\partial\sigma_{33}}{\partial A_{21}} & -\dfrac{1}{\rho}\dfrac{\partial\sigma_{33}}{\partial A_{31}} & -\dfrac{1}{\rho}\dfrac{\partial\sigma_{33}}{\partial A_{12}} & -\dfrac{1}{\rho}\dfrac{\partial\sigma_{33}}{\partial A_{22}} & -\dfrac{1}{\rho}\dfrac{\partial\sigma_{33}}{\partial A_{32}} & -\dfrac{1}{\rho}\dfrac{\partial\sigma_{33}}{\partial A_{13}} & -\dfrac{1}{\rho}\dfrac{\partial\sigma_{33}}{\partial A_{23}} & -\dfrac{1}{\rho}\dfrac{\partial\sigma_{33}}{\partial A_{33}} & 0 & 0 & v_3 & 0 & 0 & 0\\[10pt]
0 & 0 & 0 & 0 & 0 & 0 & 0 & 0 & 0 & 0 & 0 & 0 & 0 & 0 & v_3 & 0 & 0\\[4pt]
0 & 0 & 0 & 0 & 0 & 0 & 0 & 0 & 0 & 0 & 0 & 0 & 0 & 0 & 0 & v_3 & 0\\[4pt]
-\dfrac{T}{\rho^2} & -\dfrac{T}{\rho(p+p_\infty)} & 0 & 0 & 0 & 0 & 0 & 0 & 0 & 0 & 0 & 0 & 0 & 0 & 0 & 0 & v_3
\end{pmatrix}
$$

$$S_p = \frac{1}{\theta_1(\tau_1)}
\begin{pmatrix}
0 \\
(\gamma-1)\,\rho\,\|\psi\|_F^2 \\
0 \\
0 \\
0 \\
-\psi_{11} \\
-\psi_{21} \\
-\psi_{31} \\
-\psi_{12} \\
-\psi_{22} \\
-\psi_{32} \\
-\psi_{13} \\
-\psi_{23} \\
-\psi_{33} \\
0 \\
0 \\
0
\end{pmatrix}
+ \frac{1}{\theta_2(\tau_2)}
\begin{pmatrix}
0 \\
(\gamma-1)\,\rho\,\|\boldsymbol{H}\|^2 \\
0 \\
0 \\
0 \\
0 \\
0 \\
0 \\
0 \\
0 \\
0 \\
0 \\
0 \\
-H_1 \\
-H_2 \\
-H_3
\end{pmatrix}$$